Efficacy of Vickers indentation method to measure residual stress in additively manufactured IN718 specimens

BC Stander

orcid.org/0000-0002-4750-6186

Dissertation accepted in fulfilment of the requirements for the degree *Master of Engineering in Mechanical Engineering* at the North-West University

Supervisor: Mr CP Kloppers

Graduation: May 2022

Student number: 25995146

ACKNOWLEDGEMENTS

I would like to extend my gratitude to the Collaborative Program for Additive Manufacturing for providing funding and resources that enabled the completion of this study. A special thanks to Mr CP Kloppers and Dr Jaundrie Fourie for the guidance and support they provided throughout the duration of the study, as well as assistance in sample preparation and writing.

A special thanks to my parents, who have supported me in reaching my goal of acquiring this degree.

ABSTRACT

Selective laser melting of Inconel 718 powder (a nickel-based superalloy) is regularly used to manufacture gas turbine parts for the aerospace industry. Residual stresses that remain in components after manufacturing are known to be detrimental, often resulting in geometric distortion and inadequate mechanical properties. It is therefore essential to be able to measure these residual stresses. Many non-destructive residual stress measuring techniques are used in the industry, and the Vickers indentation method has been proposed as a less expensive, rapid evaluation technique of residual stresses. The efficacy of the Vickers indentation method as a residual stress measurement technique was evaluated in the study.

It was observed that, for the conditions present in the study, the Vickers micro-indentation method provided inaccurate data. Residual stresses measured using this technique varied considerably across the surfaces of the specimens, with only slight tendencies observable. Compared to X-ray diffraction measurement on cubes manufactured under the same conditions, the residual stress values calculated from the Vickers micro-indentations were very low in magnitude. Differences in hatch distance overlap percentage did not show substantial differences in calculated surface residual stress values; however, slight increases in compressive stresses were observed with increasing hatch distance overlap. Sand-blasting of specimen surfaces preceded dry electrochemical polishing and resulted in increased compressive stresses calculated by the Vickers micro-indentation method. The ability to ensure even and smooth surfaces for Vickers micro-indentations would provide more accurate data on surface residual stress values. Ultimately, it was concluded that the Vickers micro-indentation method is not suitable for surface residual stress measurements of selective laser melted components because of the inability to provide adequately smooth surfaces for indentations to provide accurate data without removing substantial amounts of component surfaces.

Finally, the inherent strain method was employed to simulate residual surface stresses on the selective laser melted components. It was found that these values did not correlate with the values obtained from Vickers micro-indentation tests and X-ray diffraction tests. These discrepancies were attributed to the inability of the simulation software to account for certain processes used during the manufacturing and preparation of the specimens.

Keywords: Selective Laser Melting, IN718, Residual Stress, Vickers Indentation Method, Simufact Additive, X-ray Diffraction

TABLE OF CONTENTS

LIST OF TABLES

LIST OF FIGURES

ABBREVIATIONS

AM	Additive Manufacturing
EDM	Electron Discharge Machining
IN718	Inconel® 718
ND	Neutron Diffraction
PBF	Powder Bed Fusion
SLM	Selective Laser Melting
VED	Volumetric Energy Density
XRD	X-ray Diffraction

CHAPTER 1 INTRODUCTION

Metal additive manufacturing (AM) of Inconel 718 (IN718) has shown promise in recent years for the production of specialised parts with comparable or higher mechanical properties than those of cast and wrought parts [1-4]. IN718 is a work-hardenable superalloy that finds application in aircraft, gas turbines and structural components used in highly corrosive environments with temperatures as high as 700°C [4-7]. IN718 is frequently manufactured using selective laser melting (SLM), an AM process involving melting metal powder particles with a laser [4, 7]. SLM is an attractive manufacturing technique for IN718 since it enables the production of complex or customised near-net shaped parts on-demand, with little need for expensive tooling typically required in conventional manufacturing methods [8, 9].

Several process parameters used during SLM may influence the mechanical properties of the final component [10-12]. These parameters influence the formation and presence of residual stresses within SLM parts [13]. Residual stresses remain in SLM parts after manufacturing and are usually detrimental, resulting in geometric distortion and reduced mechanical response under loading [7, 13]. To combat these shortcomings, heat treatment of AM parts is able to reduce residual stresses, with most SLM components requiring this post-processing procedure [4, 14]. Residual stress states usually need to be evaluated to improve the manufacturing process by altering process parameters [10, 15].

In order to determine the stress state of metallic components, multiple measurement techniques are available, being either destructive or non-destructive [13]. Destructive measurements include hole-drilling and the contour method, which are based on the premise that residual stresses exist in static equilibrium. Therefore, cutting a plane or drilling a hole through the component results in deformation of the part [13]. Non-destructive techniques are predominantly based on diffractive measurements and include X-ray diffraction (XRD) and neutron diffraction (ND). These techniques, which are based on Bragg's law of diffraction, measure the lattice spacing of the crystalline material to derive the stress state [13]. In 2001, Carlsson et al. [16, 17] developed a technique to estimate residual stress using indentation measurements, i.e., Vickers hardness tests. Experimental correlations between residual stress and the indentation characteristic were used as the foundation for the formulation of this technique. It was observed that using this technique may be suitable for rapid evaluation of the residual stresses in IN718 parts [16].

Residual stresses have been shown to have significant effects on the quality of SLM IN718 parts, and therefore a deeper understanding of the causes of these stresses and the distribution of these stresses across the surfaces of manufactured parts is essential. Furthermore, since residual

stress measurement techniques may have disadvantages such as availability and costs, it is vital to investigate the efficacy of simpler and more accessible measurement techniques.

1.1 Problem Statement

SLM manufacturing of IN718 components plays a critical role in the continuing development of modern components because of the advantageous characteristics of the manufacturing process and the scope of application. In this regard, residual stresses in SLM IN718 components may hinder the widespread use of the manufacturing method, requiring techniques to measure residual stresses. Currently, these measuring techniques are complicated, expensive, and frequently inaccessible to manufacturers. Accordingly, the validity and efficacy of a more accessible measuring technique requires investigation.

Research questions that will be answered during this study include the following:

- Can surface indentations be used to accurately predict surface residual stress in the as-built condition and stress-relieved condition of SLM specimens?
- Does surface hardness vary across the vertical and horizontal surfaces of cuboid specimens?
- To what extent does stress-relieving remove surface residual stresses of SLM IN718 specimens?

1.2 Aim and Objectives

1.2.1 Aim

This study aims to investigate the efficacy of using the Vickers indentation technique for evaluating residual stresses in IN718 specimens manufactured using a COHERENT Creator™ SLM machine across a range of different hatch distances.

1.2.2 Objectives

To achieve the study's aim, the following objectives were completed:

1. Manufacturing of IN718 SLM cuboid specimens (using different hatch distances), with both as-built and stress relieved conditions. For this, a post-processing dry electrochemical polishing surface finish was applied to all specimens.
2. Vickers indentation tests were done on various surfaces of the specimens in the as-built and stress-relieved condition for each hatch distance used.
3. Vickers indentation tests were done on the X-Z and Y-Z planes of specimens in the as-built and stress-relieved condition for each hatch distance used.

4. Measured indentation geometries were used to calculate residual stress values numerically.
5. A simulation program was used to simulate the surface residual stresses in cuboid specimens.
6. Residual stress data calculated from Vickers indentation tests were compared to residual stress values obtained from XRD analysis.

1.3 Method/Approach

The methods used consisted of two main parts: experimental methods and simulation methods. During the experimental methods, cuboid specimens were manufactured and post-processing techniques were applied to these specimens. Surface residual stress datasets were obtained across the surfaces of the specimens using Vickers indentation techniques and XRD measurements. Similarly, the simulation methods required the manufacturing of cantilever specimens used for calibration of the simulation software. After the software was calibrated, simulations were run to observe the resulting surface residual stresses at the points of interest. The high-level steps to these methods are outlined in Figure 1-1.

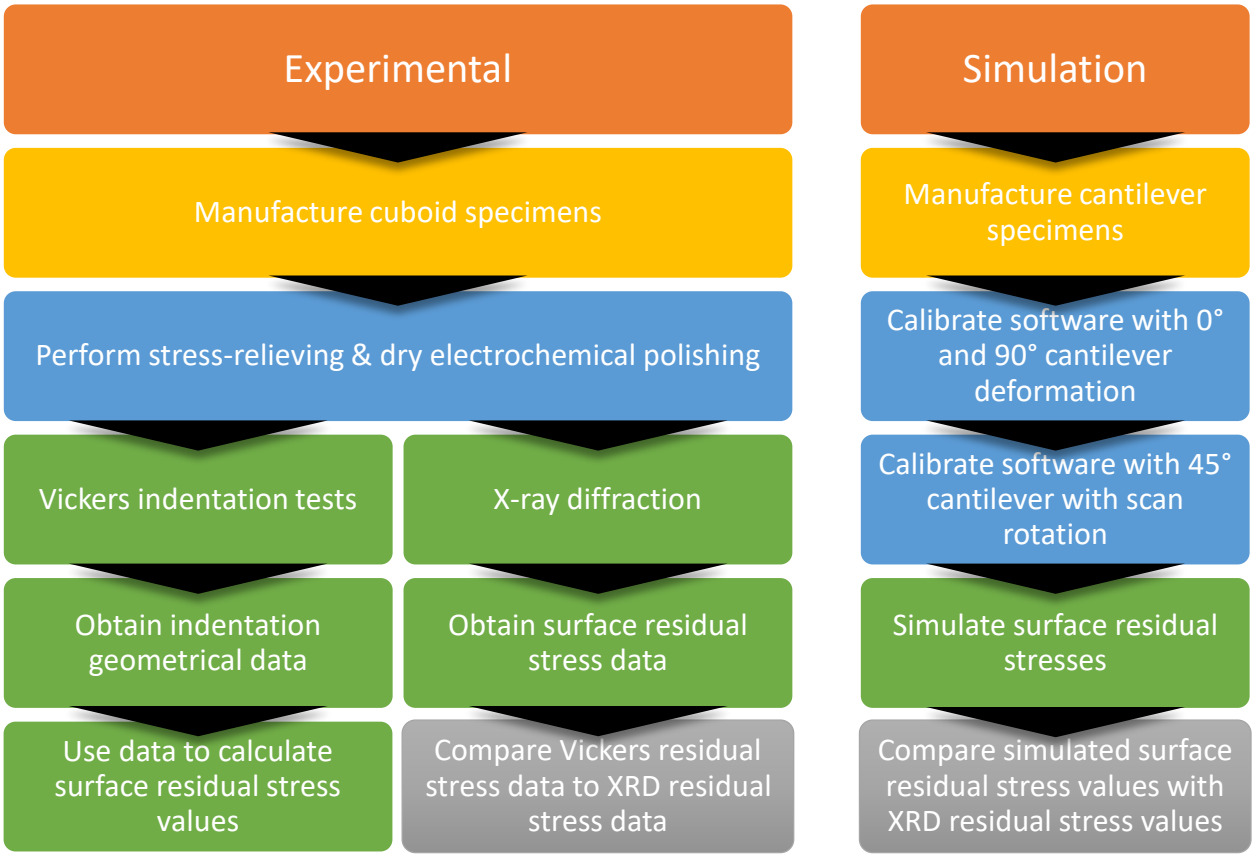

Figure 1-1: Method to be used in the study

CHAPTER 2 LITERATURE REVIEW

The contents of the following literature review provide the background and reasoning behind the study. In addition, significant findings are discussed, and ultimately the importance of this study is clarified.

2.1 Additive Manufacturing

Additive manufacturing (AM) is described as the “process of joining materials to make parts from 3D model data, usually layer upon layer, as opposed to subtractive manufacturing and formative manufacturing methodologies” [18]. The International Organization for Standardization (ISO), in conjunction with ASTM International (formerly known as the American Society for Testing and Materials), have constructed a standard document (ISO/ASTM 52900:2015) providing definitions for nomenclature used in AM technology and the definition above [18]. Vat photo-polymerisation, material jetting, powder bed fusion (PBF), material extrusion, binder jetting, sheet lamination and directed energy deposition are the seven AM process categories that all AM processes fall under [19-22].

Additive manufacturing was initially called “rapid prototyping” when the technology first appeared on the market [12, 19, 23-25]. As the name suggests, rapid prototyping refers mainly to processes that could produce an object from digital Computer-Aided Design (CAD) model data in a short amount of time, primarily for design purposes [8, 10, 19]. With the progression of AM technologies, it was realised that functional components could be manufactured directly using these processes, leading to the adoption of the term “additive manufacturing” by ASTM International [19, 26, 27]

The final part produced using AM techniques will approximate the original CAD file, with its dimensional accuracy dependent on the layer heights used [19]. AM machines predominantly use this method, with differences in the feedstock materials (metal or polymers etc.), the approach used in forming or positioning the layers (layer powder distribution, using a nozzle, curing entire layers of liquid photopolymer etc.), and the binding process used to join the layers together (sintering, liquid binder material, melted polymer filament etc.) [19]. This study will focus on the SLM process, a PBF technique used to form near net shape metallic components [19, 21, 24].

2.2 Selective Laser Melting

The SLM process incorporates a laser that is scanned across a powder bed, melting powder particles together per layer [21, 24, 28]. SLM is widely used to manufacture near-net-shape parts directly from metal powders [8, 29, 30]. SLM effectively supplements or replaces traditional manufacturing methods, especially for once-off components, small production lines and where a

reduction of part count is beneficial [8, 9, 31]. Cost- and time-saving manufacturing methods like SLM are valuable for industry leaders, especially in the aerospace industry [12, 31]. Parts fabricated by SLM potentially have static mechanical properties equal to those of conventionally fabricated parts, given that the process parameters are correctly programmed [1-4, 29, 32]. The process is depicted in Figure 2-1 [33].

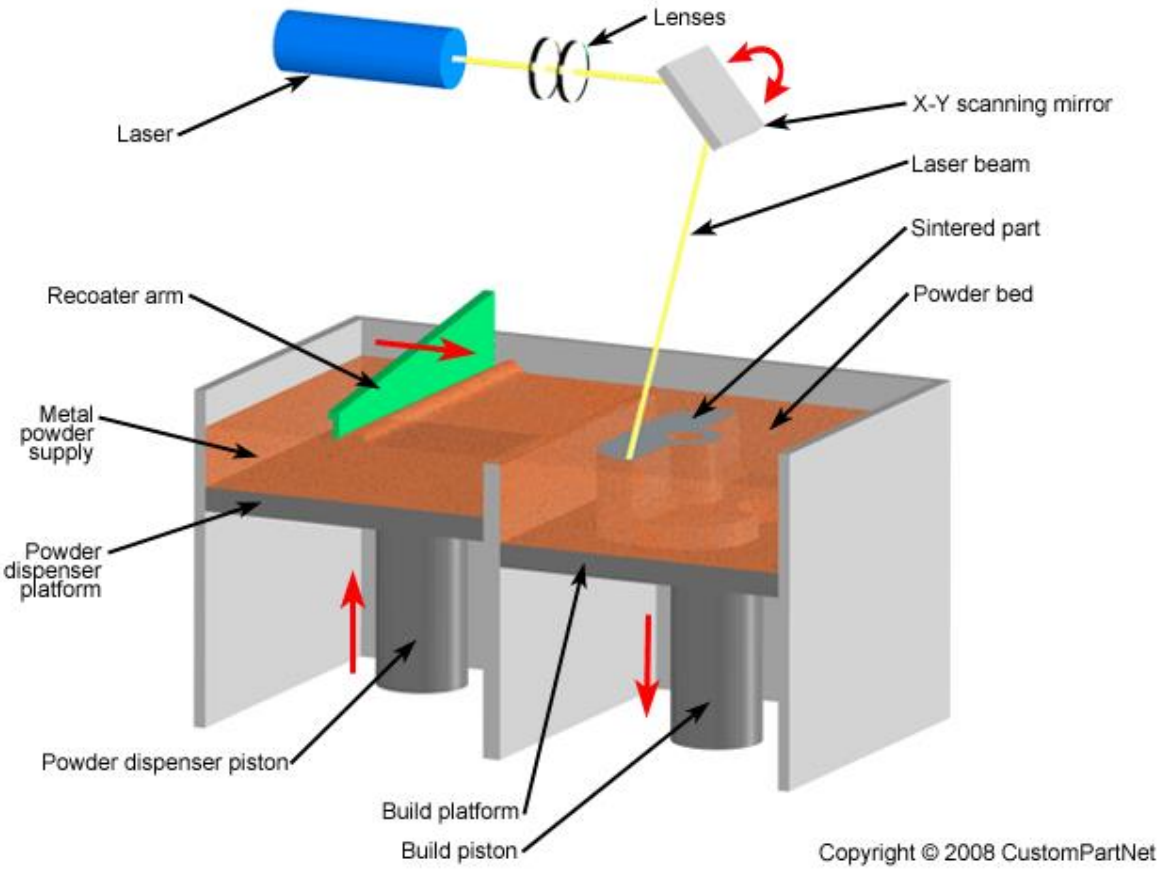

Figure 2-1: Selective laser melting process (from CustomPartNet Inc. [33])

It should be noted that the beam deflection process depicted in Figure 2-1 shows a post-objective scanning system where the laser beam is first focused through lenses before it is redirected to the processing region [34]. Other systems may implement pre-objective scanning processes, during which F-Theta lenses focus the laser beam after it has been redirected by deflection mirrors towards the build region [34].

2.2.1 SLM Process

Since SLM is a PBF process, the final component is manufactured from metallic powder feedstock material with particular powder morphology, sphericity and particle size distribution (usually

ranging from 5μm to 50μm) [12, 21, 24, 26, 28, 35]. Properties of SLM feedstock powders include good flowability and packing characteristics, which will ensure sufficiently high packing density for enhanced final densities of components [24, 26]. Conversely, using powder with a lower quality than the process requires may lead to lowered relative density, which causes weak mechanical properties, undesirable dimensional tolerances, and ultimately unusable components [3, 26].
During the SLM process, an oxygen content of less than 0.1 % is maintained in the enclosed chamber using inert gases (usually argon or nitrogen) to prevent powder degradation and powder combustion, since certain feedstock material may become more reactive when exposed to oxygen [19, 26, 36-38]. An inert atmosphere is also maintained to prevent oxygen from contaminating the melt pool preventing oxidation of the melting material [8, 37, 39]. While the inert atmosphere is maintained, the metallic powder is distributed in thin layers (typically between 20μm and 100μm) onto a build plate for the first layer and subsequently on previously deposited layers [31, 40]. Next, another powder layer is distributed across the previously melted layer, usually by a roller or coater arm [19, 40, 41]. The process continues until the final layer is completed and the object is fabricated [12]. A laser beam (which is guided by galvanometric mirrors) is used to fully melt specific areas of the powder, effectively creating a “slice” or layer of cross-section specified by the original CAD model that was uploaded to the machine [19, 24, 28, 42-44]. These laser beams are usually single-mode fibre lasers used in continuous wave mode with wavelengths of 1060nm to 1080nm; however, neodymium-doped yttrium aluminium garnet (Nd: YAG) lasers may also be used [19, 26, 32, 44, 45]. The nature of the laser beam causes an intensity distribution across the diameter of the beam, which is often assumed to follow a Gaussian profile, meaning that the intensity of the laser beam is at its maximum at the centre and drops radially outwards [28, 41, 46, 47]. The process of the laser melting the powder particles together basically amounts to rows of overlapping weld beads being formed [24, 48]. In addition, the heat generated by the laser allows the current layer to adhere to previously melted layers, effectively adding another layer to the part [3, 28].

The parts are connected to the build surface by support structures during the process, which are necessary for heat dissipation and for supporting horizontal overhang surfaces to prevent distortion [3, 19, 26]. These support structures are cut off after manufacturing the part, usually employing abrasive saws or wire electron discharge machining (EDM) [3, 24, 30]. Components taken directly out of the SLM machine are referred to as “as-built” [3, 8, 24, 28].

2.2.2 Process Parameters

The mechanical properties of parts manufactured with SLM depend on several process parameters, with even slightly incorrectly applied combinations causing parts to have undesired properties [10-12]. These parameters include laser power, scan speed, layer thickness, scan

pattern and hatching distance [7, 10-12, 49]. Laser power may be defined as the incident energy of the laser per unit time [50]. The rate at which the laser moves is referred to as the scan speed [12, 50]. The layer thickness or layer height refers to the physical height of the layers of powder after the layer is melted [12, 50, 51]. Scan pattern refers to the specific path followed by the heat source during SLM [3]. Finally, hatch distance describes the distance between parallel scan tracks created by two passes of the laser over the powder bed [11, 12].

Evaluation of the effects of different parameters revealed that most parameters are interdependent [11, 25, 50, 52, 53]. This interdependency means that when specific parameters are kept constant, variations in another parameter will yield different results, e.g., variations in scan speed (while keeping laser power at a specific value) will yield different results for the same variations in scan speed while keeping laser power at another constant. This interdependency requires process parameters to be adjusted simultaneously when significant variations are used [9]. The volumetric energy density (VED) (energy density delivered to the build surface during SLM fabrication) is often used as a means to quantify the combined effects of layer thickness, hatch distance, scan speed and laser power on the mechanical properties of SLM components, and is given by Equation (2.1) [11, 14, 50, 52, 54].

$$E = \frac{P}{v \times h \times t} \tag{2.1}$$

In Equation (2.1), P is the laser power, v is the scan speed, h is the hatch distance, and t is the layer thickness. Although the VED is often used in literature, it is not sufficient to explain differences in observed outcomes of porosity, residual stresses, and distortions of specimens [14, 55]. When comparing results between different SLM studies, the VED might be beneficial; however, it would need to be altered significantly to account for the effects of gas flow direction, laser spot size and the properties of the materials being used [54].

2.3 Residual Stress

Generally, large and anisotropic stresses arise inside the component during SLM manufacturing and remain after manufacturing is completed; this phenomenon has obstructed widespread use of the SLM process [7-10, 13, 14, 19, 24, 56-58]. These undesirable stresses are referred to as residual stresses, and they generally exist in static equilibrium [8, 13]. Residual stresses may be plastic when the thermal stress is higher than the material's yield strength, which would result in a deformed part [9, 57]. Support structures anchor the component to the build plate to counteract distortion during the manufacturing process [28].

2.3.1 Residual Stress Formation

It is helpful to consider a simplified case of the SLM process (where entire layers are melted instantaneously) to understand the formation of residual stresses [13]. Tensile stress is induced in the upper layers of the component and compressive stress in the lower part during SLM manufacturing [56]. After removing the component from the build plate, the residual stresses may be relaxed due to elastic deformation, resulting in lower residual stress [7, 56]. A simple explanation of the formation of residual stresses resulting from large temperature gradients during the SLM process is shown in Figure 2-2 [56].

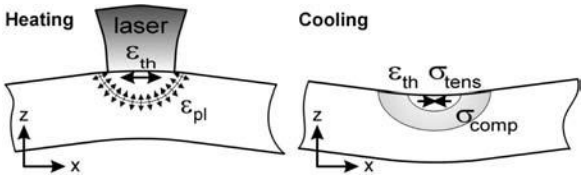

Figure 2-2: Formation of residual stress (with permission from [56])

During the heating stage, the topmost layer is heated rapidly. With slow conduction to the underlying layers, a steep temperature gradient develops. Elastic compressive stresses are induced due to the underlying layers restricting the expansion of the top layer [56]. Subsequently, the topmost layers cool down rapidly and shrink. Again, this deformation is restricted by the underlying layers, and tensile stresses are formed in the newly added top layer, with compressive stresses induced in the underlying layers [56, 59]. In short, residual stresses are predominantly caused by changes in volume during manufacturing when the powder melts and expands from the heat applied and, after that, solidifies and shrinks when the heat is removed [9, 28].

2.3.2 Types of Residual Stress

Residual stresses arise due to thermal strain and phase transformations that occur during the SLM process, caused by the non-uniform distribution of temperature at the powder bed surface [7, 9]. In addition, the fluctuating rates of expansion and subsequent shrinkage of already solidified material surrounding the melt pool due to the heating and cooling cycles result in thermal stresses that cause the formation of residual stresses [7, 9].

Three different types of residual stresses can form during the SLM process; Type I, Type II and Type III residual stress [13, 56, 60]. Type I residual stresses act on the macroscale (component scale) that may distort the component itself [13, 56, 60]. These are the stresses that are most frequently discussed in the literature concerning AM [13]. Type II and Type III residual stresses refer to intergranular and inter-atomic stresses, respectively [13, 60, 61]. Type II stresses are

caused by the misalignment of preferred slip-planes and Type III residual stresses by interstitial atoms in the matrix or the vacancies of atoms, and both of these types of stresses only affect the strength of the material to a small extent [13, 56]. Therefore, only Type I residual stress will be discussed further, as these stresses play the most important role in distortion of specifically SLM parts and will only be referred to as “residual stress”.

2.3.3 Process Parameter Effects on Residual Stresses

Process parameters have been shown to affect the magnitude and distribution of residual stresses in SLM components [9, 13, 43, 45, 49, 62-66]. For example, it was observed by Song et al. [67] from simulated results that the maximum residual stress values decreased linearly with increasing VED. However, parametric effects reported in the literature are often contradictory since a complex relationship exists between process parameters and residual stress, and residual stress behaviour varies between different ranges of process parameter values [68].

For thin-walled IN718 specimens, increased residual stresses have been observed with increases in **laser power** [63]. In other cases, residual stresses were observed to decrease with increases in laser power [9, 67]. It should be noted that, in the latter scenarios, the laser power was varied simultaneously with other parameters. Higher **scan velocities** led to average decreases in residual stresses in some cases [43, 63]. The opposite trend was observed in other studies using the same scan velocities, signifying scan speed's complex effect on residual stresses [9, 62]. Increasing **layer thicknesses** resulted in decreasing residual stresses within thin-walled IN718 components and Maraging Steel 300 manufactured with SLM [14, 63]. Similarly, fewer residual stress-related distortions were present when increasing the layer thickness of tool steel powder during SLM; however, this was because of higher porosity in the specimens [62]. Altering the **scan pattern** used during SLM also significantly affects residual stresses [3, 45, 67, 69, 70]. Scan strategies include the chess/island scan pattern, spot melt scanning, different types of raster scanning (bi-directional or “criss-cross” pattern) and space-filling curves (all strategies with and without rotation between subsequent layers) [3, 4, 10, 45, 66, 70-72]. In particular, the island scan pattern has been used widely in literature to minimise residual stresses by spreading heat distribution more evenly, at the cost of higher localised stresses [3, 45, 69, 70]. Residual stresses themselves should first be understood to understand how these process parameters affect the residual stresses in SLM components. In addition, understanding the mechanisms behind the formation of these stresses and methods to measure or estimate residual stresses in manufactured components is important to prevent or mitigate the effects of residual stresses on SLM components.

2.3.4 Effects of Hatch Distance on Residual Stresses

Another parameter that affects residual stress formation is the hatch distance [53, 64, 73]. This parameter describes the distance between parallel melt pools created by two laser passes over the powder bed, as shown in Figure 2-3 [11, 12, 46].

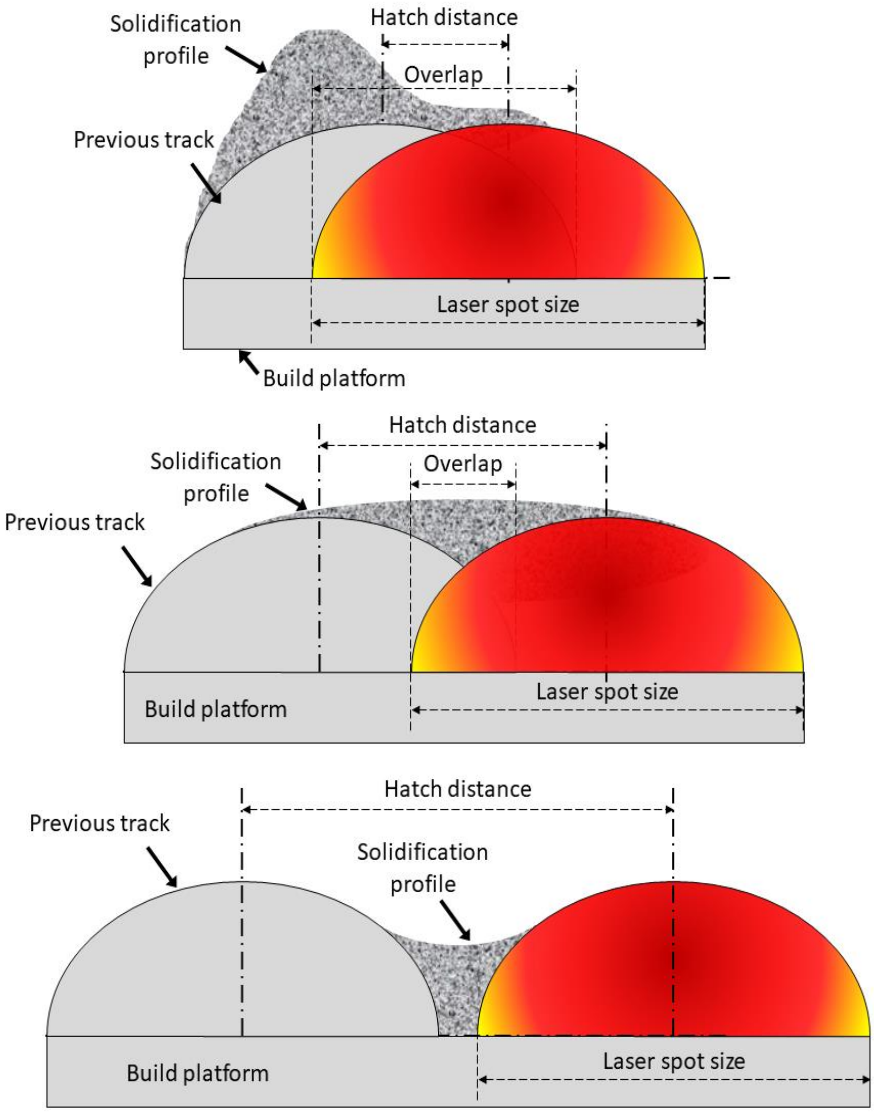

Figure 2-3: Effect of hatch distance on solidification profile (adapted from [46])

This parameter dramatically affects SLM components; e.g. small hatch distances may have detrimental effects on the printing process and ultimately on the mechanical properties of the finalised components, whereas larger distances may increase build rates but may also cause increased porosity [11, 46, 50]. When using smaller hatch distances, the heat flux formed by the vaporisation results in a recoil pressure, forcing the molten material away from the centre and onto the previously fabricated tracks [46]. The surface tension of molten material also influences this driving force [46]. This phenomenon was observed in a study by Wang et al. [29], where it

was confirmed that steep thermal gradients would result in molten fluid flow from a region of low surface tension to regions of higher surface tension, referred to as Marangoni flow [8, 29, 71, 74, 75]. The extra force will be employed on the molten material, causing the fluid to separate into smaller volumes to minimise surface free energy [29].

Physically, when regarding hatch distance and the SLM process as a whole, it is clear that small hatch distances will increase hatch overlap, with molten material build-up between laser paths [53]. On the other hand, hatch distances much larger than the laser spot size (the diameter of the laser focal point) will result in gaps between molten tracks, where powder particles may become trapped [46, 50]. Hatch distance will therefore need to be appropriately configured to create molten tracks that form a flat surface.

Liu et al. [15] observed that the measured thermal residual stresses were higher in the overlapping regions between two laser passes (hatch overlap) than in the centres of laser passes. Overlap regions have been shown to undergo complex heat treatments during surrounding laser passes when an overlap ratio of 20 % is used [15, 76]. Process parameter maps were created by Balbaa et al. [9], during which it was observed that a hatch distance overlap of -20 % (the negative value indicates distances between laser passes) gave the lowest surface residual stresses across a range of laser power and scan speed values, compared to larger hatch distance overlaps of 0 % and 20 % [9]. However, lower hatch distance overlaps led to higher residual stresses in SLM manufacturing of Ti-22Al-25Nb [64]. Deformation caused by residual stress increased with increasing hatch distance overlaps when manufacturing pure iron powder components with direct metal laser sintering (DMLS) [53]. At lower laser powers (240 W), the smallest residual stress value was found to be at 0 % hatch distance overlap, compared to 20 % and -20 % of SLM Ti6Al4V specimens by Xiao et al. [68]. Residual stress values showed decreasing tendencies with decreasing hatch distance overlaps for higher laser powers (300 W and 360 W) [68]. In contrast, in another study, increasing hatch distance overlaps decreased subsurface residual stresses (when using short layer scan times) [73]. This contradiction between the two abovementioned studies is most likely the result of different laser powers used; Mishurova et al. [73] used a laser power of 175 W, whereas Xiao et al. [68] used higher laser powers. These findings are summarised in Table 2-1.

Table 2-1: Hatch distance effects on residual stresses in literature

Hatch distance overlap	Residual stress	Material	Process	Source
↓	↓	IN718	SLM	[9]
↓	↑	Ti-22Al-25Nb	SLM	[64]
↓	↑	Ti6Al4V	SLM	[73]
↓	↑↓↑	Ti6Al4V	SLM	[68]

Results obtained by Xiao et al. [68] are shown for a laser power of 240 W. At higher laser powers (300 W and 360 W), the trend is similar to those found by Balbaa et al. [9], where residual stresses decrease with decreasing hatch distance overlap.

2.3.5 Residual Stress Measuring Techniques

Residual stress measurement techniques are generally categorised as being either destructive or non-destructive [13, 77]. Components that underwent destructive measuring cannot be used after testing is completed, whereas non-destructive techniques are non-intrusive, and the components are not damaged to such an extent that they become unusable for subsequent testing [78, 79].

2.3.5.1 Destructive Residual Stress Measurement

The basis for destructive measuring techniques is that residual stresses exist at static equilibrium within a component [13]. This phenomenon enables residual stresses to be indirectly measured by cutting across any given plane of the component resulting in a redefined state of static equilibrium through deformation of the plane [13]. This deformation can then be measured using coordinate measurement machines with the deformation values introduced into a finite element model (FEM), and the residual stresses normal to the cut plane can be determined by calculating the stresses required to deform the measured plane back to a flat surface in the FEM model [13, 77].

Two destructive techniques, namely the hole-drilling and contour methods, are based on this premise [13, 77]. Therefore, the accuracy of the data obtained using these methods is naturally dependent on the accuracy of the deformation measurements [13].

2.3.5.2 Non-Destructive Residual Stress Measurement

ND and XRD are two commonly used non-destructive residual stress measurement techniques [13]. These techniques are based on Bragg's law for diffraction, with which the crystal lattice spacing inside the metallic component can be measured and compared to the unstrained lattice spacing measurements [9, 13]. A stress-free sample is generally needed to determine the

residual stress in a stressed component [77]. Macroscopic stresses can be determined with these measurements using crystallographic information; however, XRD measurements can only detect elastic residual stresses [9, 13].

Another non-destructive technique is the three-dimensional digital image correlation (3D-DIC) system, which has also been used to evaluate in-situ residual stress formation by measuring surface distortions of SLM manufactured components [80]. Two high-resolution cameras are mounted so that the surface of the component can be captured [80]. This method proved to be accurate in a study by Bartlett et al. [80] since the difference between measured values did not exceed 6 % from obtained XRD residual stress values.

An alternative non-destructive residual stress measurement technique may be found in the form of Vickers micro-indentation tests. These tests are usually classified as non-destructive due to the relatively small indentations (~50μm) required for measurements, and the geometry generated may be used to evaluate residual stresses [15, 16, 45, 81-85]. Carlsson and Larsson [16] showed that an experimental correlation between residual stress and the indentation characteristic (i.e. surface area) could be used to calculate residual stress values. The study showed that the residual plastic strain fields influence the hardness value itself, and the ratio between the actual area of the indentation to the nominal area is affected by the residual stresses present in the material [16]. Figure 2-4 shows the difference between actual and nominal Vickers micro-indentation areas, with the red line indicating the actual area and the white rhombus denoting the nominal area (based on the corners of the indentation).

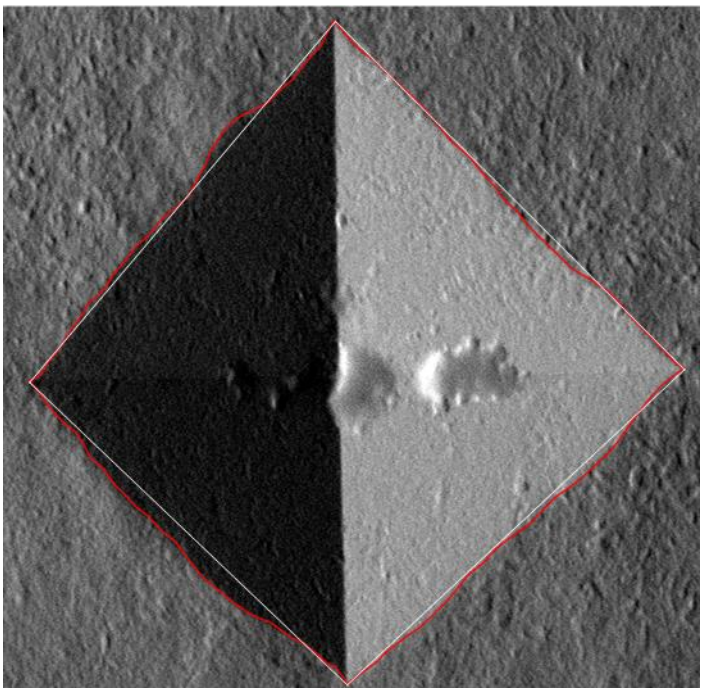

Figure 2-4: Actual and nominal Vickers micro-indentation area

The difference between these two areas is caused by residual stresses at the component's surface and can therefore be used to calculate the stress magnitudes present in the component (as discussed in 3.1.2) [16].

2.4 Post-Processing Heat Treatment

Heat treatments can be used to decrease the residual stresses in SLM components [3, 4, 12, 14, 35, 58]. Establishing which heat treatment(s) to use for specific parts depends on the microstructure of the as-built part, its application, and the properties needed [7]. Stress-relieving heat treatment is proposed in the standard specification F3055 specifically for AM IN718, as shown in Table 2-2 [7, 27].

Table 2-2: Stress-relieving heat treatment for IN718 [7, 27]

Stress relief
1065±15°C for 85-105min, performed while the components are attached to the build platform

No additional information is provided by the standard, and should therefore only be used as a guideline [7, 27]. Improved heat treatments have been recommended which include double aging techniques used with intermittent water-quenching steps, however, heat treatments for specific outcomes do not form part of this study, and will therefore not be investigated further [4, 8, 12].

2.5 Conclusion

Considering the research done on the effects of the various parameters on the mechanical properties of IN718 fabricated with SLM, some conclusions can be drawn concerning the parameters and their ideal settings. Suitable parameter sets can be tailored for specific desirable properties; however, it is challenging to find parameter sets where all properties are desirable. Balbaa et al. [9] evaluated scan speed, laser power, and hatch distance to a certain extent whilst evaluating the effects on surface residual stresses, surface roughness, and relative density. It was proposed that values of 320 W laser power, 600 mm/s scan speed and 0.12 mm hatch distance are used to minimise surface roughness. Samples fabricated with these values had 99.2 % relative density. If the density is the main priority, a laser power of 270 W coupled with a scan speed of 700 mm/s and hatch distance of 0.1 mm was proposed, which provided a relative density of 99.56 % [9]. Bartlett et al. [13] insisted that no clear correlation could be found between material density and residual stress magnitude; however, Lu et al. [45] found that low density (around 98.67 %) may have led to lower residual stresses as a result of cracking. In contrast, Kruth et al. [86], demonstrated that distortion (and therefore residual stresses) of SLM parts were practically unaffected by density itself, but more by processing parameters used.

Clearly, from the literature study, residual stresses are critical during SLM manufacturing; however, it is not always possible to predict these stresses before a component is manufactured, although literature provides insight into this issue. From the literature review in Chapter 2, it was realised that the presence and formation of residual stresses in the SLM process are causes of concern in the AM community. Several methods and techniques are available to measure residual stresses near the surfaces of SLM components, most of which are expensive or not accessible. Therefore, it is hypothesised that using the Vickers micro-indentation technique will be a quicker and less expensive way to measure surface residual stresses of SLM specimens, specifically for IN718. Furthermore, validation of the Vickers indentation tests for residual stress determination would require validation; accordingly, the XRD approach for surface residual stress would be beneficial in understanding the stress state of the components.

CHAPTER 3 THEORY

The necessary theory is discussed in this chapter. First, some background is given on the theory used, and the essential Equations are derived.

3.1 Vickers Indentation Test

Hardness is defined as the resistance of a body to be penetrated by another body [87, 88]. Different hardness tests are available, including Brinell, Vickers and Rockwell [19, 89]. Vickers was chosen for this formulation since the specific geometry is needed for the relation towards surface residual stresses [16].

3.1.1 Vickers Hardness

In the case of the Vickers hardness test, a square diamond pyramidal indenter is used, with opposite faces making an angle of 136° [88, 89]. The hardness value is obtained from the ratio of the applied load to the area formed by the indentation (after the load has been removed) and has pressure as dimension [88, 89]. The applied load (or "test force") is calculated from the mean value of the two diagonal lines across the test surface indentation, assuming that the indentation is geometrically true to the indenter [88]. Thus, the Vickers hardness is given by the following Equation (3.1) [88].

$$HV = \frac{0.102 \times F}{A} \tag{3.1}$$

In Equation (3.1), HV is the Vickers hardness number, F is the applied load in [N], and A is the area of the indentation [88]. The constant 0.102 originates from the kilopond (kp) unit used to measure test forces before 1969 [88]. To avoid high restructuring and conversion costs, the conversion relation $1\ N = 0.102\ kp$ is used to keep the original round kp values [88]. To calculate the area left by the indenter, the mean length (L) of the two diagonal lines of the indentation (L_1 and L_2) is used. From the geometry of the Vickers indentation, it follows that

$$A = \frac{L^2}{2 \times sin68°} = \frac{L^2}{1.854} \tag{3.2}$$

and therefore:

$$HV = 0.102 \times F \times \frac{1.854}{L^2} = \frac{0.1891 \times F}{L^2} \tag{3.3}$$

3.1.2 Residual Stress from Vickers Indentation Tests

Based on theoretical and numerical analyses and experimental investigations, Carlsson et al. [16, 17] found that residual strain fields can be accurately correlated with the hardness value of sharp (Vickers) indentation tests. At the same time, the size of the contact area can be related to the

residual stresses in the component [16, 17]. When an assumption is made that the residual stresses are in an equibiaxial state and that the uniaxial stress-strain curve can be approximated with a power-law function, accurate results can be obtained [15, 17]. Using the Vickers hardness test, the hardness of the measured surface is accurately given by Equation (3.4):

$$H = C \times \sigma_Y \tag{3.4}$$

In this Equation, H is the Vickers hardness value, C is a constant related to the geometry of the indenter itself, and σ_Y is the yield strength of the tested material. The σ_Y value is replaced with σ_{repr} for a strain-hardening material (such as IN718), which is the flow stress at a representative value of plastic strain, ε_{repr}, leading to Equation (3.5) [6, 7, 16, 82].

$$H = C \times \sigma(\varepsilon_{repr}) \tag{3.5}$$

Furthermore, an assumption is made that the change in hardness resulting from a residual plastic strain is present and must be considered if a more accurate representation is desired [16, 82]. The representative strain in Equation (3.5) is therefore used in summation with the residual plastic strain. Hence Equation (3.5) is rewritten as Equation (3.6) [15, 16]:

$$H = C \times \sigma(\varepsilon_{repr} + \varepsilon_{res}) \tag{3.6}$$

In conjunction with this, Equation (3.7) gives:

$$\mathrm{H} = \frac{P}{A} \tag{3.7}$$

where H is the micro-hardness of the point tested, P is the applied load during testing [N], and A is the actual projected area [mm^2]. This formula differs from the definition of the micro-Vickers test, where $HV = P/A_{surf}$ [kgf/mm^2] and A_{surf} is the surface of the sharp indenter [82]. A new indentation parameter was introduced into the model by Carlsson et al. [16] to establish a correlation between the actual projected area and the nominal projected area (referred to as the area ratio), as demonstrated in Equation (3.8):

$$c^2 = \frac{A_{real}}{A_{nom}} \tag{3.8}$$

This indentation parameter includes the effect of elastic deformation, which is represented by the change between the actual area (A_{real}) and the nominal area, as shown in Figure 3-1 [82].

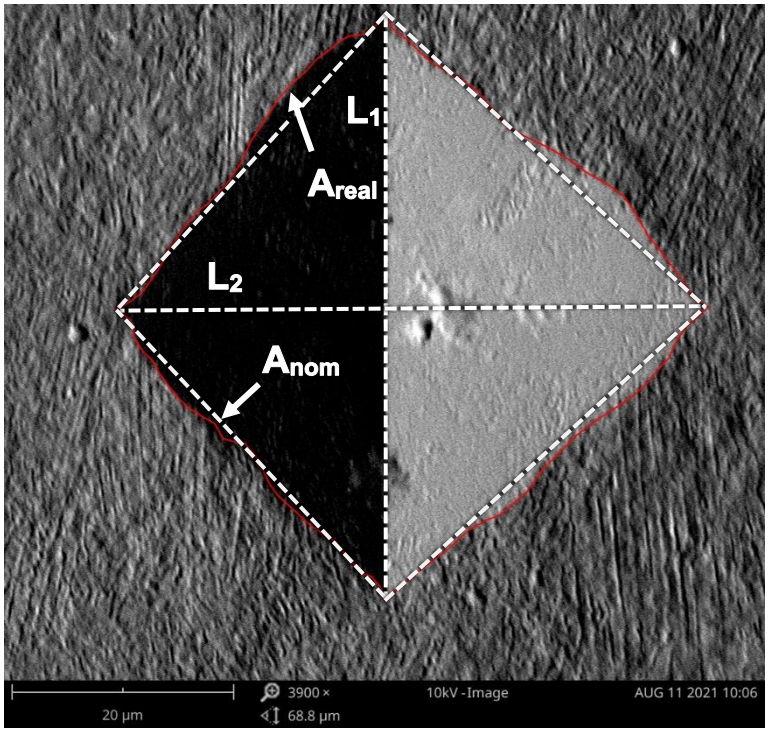

Figure 3-1: Nominal and actual area of a Vickers indentation

The red line around the perimeter of the indentation in Figure 3-1 is the actual area, and the white dashed rhombus is the nominal area of the indentation. Diagonal lines are marked L_1 and L_2, respectively. The value of A_{nom} can be calculated using the two measured diagonals of the indentation, as shown in Equation (3.9) [15, 83]:

$$A_{nom} = \frac{1}{2}\left(\frac{L_1 + L_2}{2}\right)^2 \quad \textbf{(3.9)}$$

Carlsson et al. [16] found that the residual stresses and strains also obey the following relation:

$$c^2 = c_0^2 - 0.32 \ln\left(1 + \frac{\sigma_{res}}{\sigma(\varepsilon_{res})}\right) \quad \textbf{(3.10)}$$

In Equation (3.10), ε_{res} is the residual Von Mises plastic strain and $\sigma(\varepsilon_{res})$ is the flow stress present at the point where ε_{res} is true [82, 84, 90]. The value of c^2 is the area ratio in the case of both residual stresses and strains present, and c_0^2 is the area ratio in the case of no residual stress [17].

Uniaxial stress-strain curves from Gao et al. [91] were used (shown in Figure 3-2) since the heat treatment used for these curves were the same as the heat treatments used in the current study, therefore providing comparable data.

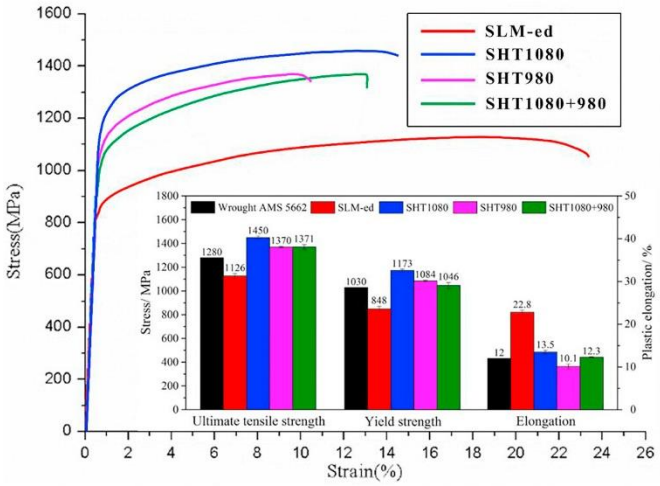

Figure 3-2: Room temperature tensile properties of SLM-fabricated Inconel 718 (with permission of [91])

Power-law functions were approximately fitted to the "SLM-ed" and "SHT1080" curves in Figure 3-2, providing (3.11) and (3.12), respectively:

$$\sigma_{ab}(\varepsilon_{ab}) = \sigma_0 \varepsilon_p^n = 349.44\ \varepsilon_p^{0.1391} \tag{3.11}$$

$$\sigma_{sr}(\varepsilon_{sr}) = \sigma_0 \varepsilon_p^n = 539.19\ \varepsilon_p^{0.1125} \tag{3.12}$$

In both these Equations [(3.11) and (3.12)], ε_p is the plastic strain [84]. Therefore, considering the following formulae [15, 83, 90],

$$\varepsilon_{res} = \left(\frac{P}{C\sigma_0 \times A_{nom}}\right)^{\frac{1}{n}} - \varepsilon_{repr} \tag{3.13}$$

$$\sigma_{res} = \sigma(\varepsilon_{res})^n \times \left[e^{\left(\frac{c_0^2 - c^2}{0.32}\right)} - 1\right] \tag{3.14}$$

the residual stresses can be calculated with

$$\sigma_{res} = \sigma_0 \left(\left[\frac{8 \times P}{C\sigma_0 \times (L_1 + L_2)^2}\right]^{\frac{1}{n}} - \varepsilon_{repr} \right)^n \times \left\{ e^{\left[\frac{c_0^2 - \frac{8 \times A_{real}}{(L_1+L_2)^2}}{0.32}\right]} - 1 \right\} \tag{3.15}$$

The use of a Vickers indentation suggests that C = 3 [89], ε_{repr} = 0.08 [89] and c_0^2 = 1, within a certain accuracy standard [15, 17]. Finally, the following Equation can then be used to determine the residual stress:

$$\sigma_{res} = \sigma_0 \times \left(\left[\frac{8 \times P}{3 \times \sigma_0 \times (L_1 + L_2)^2} \right]^{\frac{1}{n}} - 0.08 \right)^n \times \left\{ e^{\left[\frac{1 - \frac{8 \times A_{real}}{(L_1 + L_2)^2}}{0.32} \right]} - 1 \right\} \quad \textbf{(3.16)}$$

Some studies propose using Equation (3.16), with a minor difference, to calculate the Von Mises stresses [15, 83, 84]. However, this Equation differs only at the term where the two area coefficients are subtracted from each other, and the absolute value of the calculated stress is used.

$$\sigma_{res} = \left[\sigma_0 \times \left(\left[\frac{8 \times P}{3 \times \sigma_0 \times (L_1 + L_2)^2} \right]^{\frac{1}{n}} - 0.08 \right)^n \times \left\{ e^{\left[\frac{\frac{8 \times A_{real}}{(L_1 + L_2)^2} - 1}{0.32} \right]} - 1 \right\} \right] \quad \textbf{(3.17)}$$

Equation (3.17) is then used to calculate the Von Mises stresses at the Vickers micro-indentation locations.

3.2 Residual Stress from X-Ray Diffraction

It was mentioned earlier (Measurement techniques) that XRD is a commonly used non-destructive method for measuring residual stresses and that the technique is based on Bragg's law for diffraction [13, 92]. The technique relies on the internal lattice spacing of polycrystalline materials, which changes due to internal stresses inside the material. The change in lattice spacing corresponds to the magnitude of the internal stress; therefore, the lattice structure acts as a micro-scale strain gauge [92]. When a component surface is irradiated with X-rays, the lattice planes of the material diffract some of the rays, and a detector identifies the angles and intensity of the diffracted rays, creating a discernible pattern [92]. The detector is rotated through a range of angles, and peak locations in these patterns indicate the stresses within the component [92, 93]. The diffraction intensity is obtained as a function of the incident angle θ, and the measurements of these angles are recorded as 2θ, since the incident and diffracted angles are the same size [93]. To understand residual stresses and the way in which they act on the surfaces of specimens, an introduction to the principal stresses is necessary, as well as a statement of what convention will be used in the current study.

3.2.1 Principal Stresses

A coordinate system can be defined on which only normal stresses (perpendicular to plane surfaces) act, and no shear stresses are present. This is done by defining the coordinate system such that the axes are perpendicular to the planes of an elemental cube, which are then referred to as the principal planes [92]. Normal stresses are denoted as σ, with a subscript assigning it to the plane on which it acts, e.g., σ_x is the normal stress that acts in the x-direction of the coordinate

system [92]. The current study will adhere to the convention of positive tensile stress values and negative compressive stress values.

3.2.2 Bragg's Law

Crystalline materials, which consist of atoms periodically spaced in specific patterns, may result in interference (either constructive or destructive) when placed in the path of an X-ray beam [92]. The two main factors that influence the interference pattern are the wavelength of the incident radiation (λ) and the inter-planar spacing (d) [92].

When considering a row of atoms and two parallel rays striking two of these atoms respectively at a certain angle (as in Figure 3-3), it is expected that, since the rays are reflected over a range of angles, that at a specific angle, the reflected rays will be in phase with each other [92]. Furthermore, constructive interference between the reflected rays will be observed since their path lengths are equal between the incoming and reflected wavefronts [92].

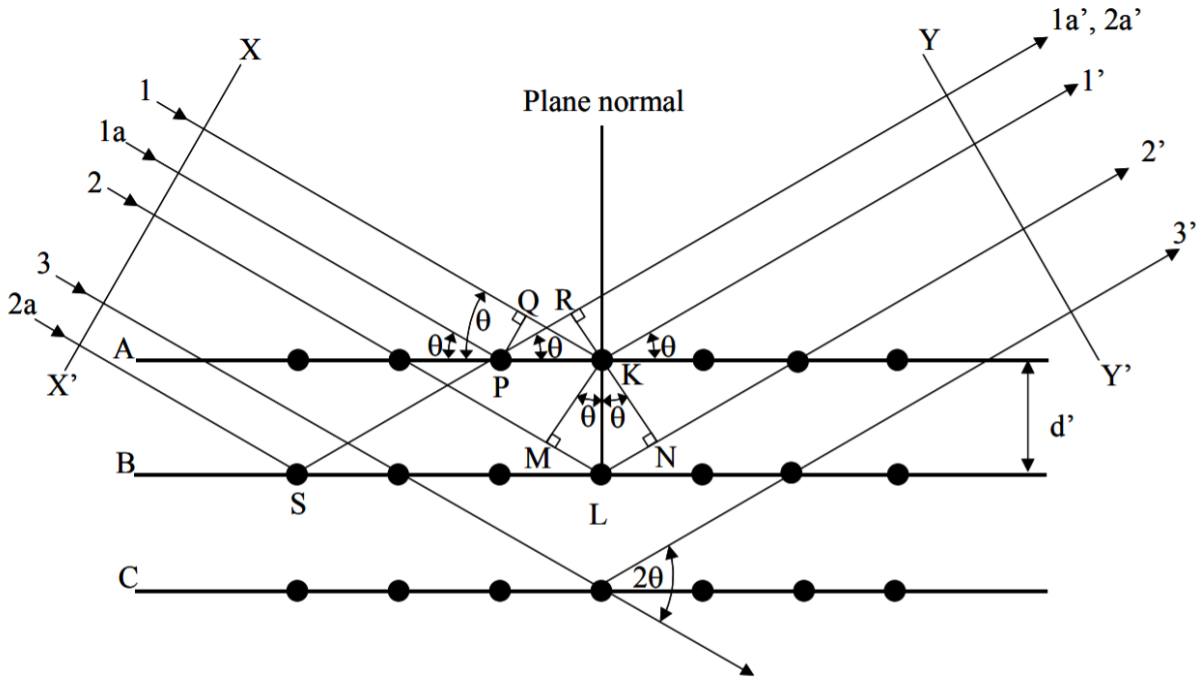

Figure 3-3: Diffraction of X-rays by a crystal lattice (with permission of [92])

Numerically, this will mean that:

$$QK - PR = PKcos\theta - PKcos\theta = 0 \quad \textbf{(3.18)}$$

If it is further observed that constructive interference is present as a result of reflections off one atom in the previously mentioned row and another atom in a lower plane, then, referring to these atoms as K and L, respectively, the path difference for the incoming-reflected rays reflected off K and L will be equal to:

$$ML + LN = d'sin\theta + d'sin\theta \quad \textbf{(3.19)}$$

Other rays reflected off different atoms than those mentioned above will only be in phase with the rays reflected off K and L when the path difference equals a whole number of wavelengths [92, 93]. Thus:

$$n\lambda = 2d'sin\theta \quad \textbf{(3.20)}$$

Equation (3.20) is known as Bragg's Law, on which XRD is based [92, 93].

3.2.3 Strain Measurement

It has been shown that the inter-planar spacing of atoms within the specimen has strong relationships with the diffraction pattern that is observed when X-rays are diffracted by the crystal lattices inside the specimen [92]. Variables affecting the resultant diffraction pattern include the inter-planar spacing and the wavelength of the X-ray beam [92]. Therefore, a specific diffraction pattern will be obtained whenever an unstrained specimen of a specific material is observed through XRD. Furthermore, since residual strains affect the crystal lattice by inducing expansions and contractions, the dimensional difference between the strained and unstrained specimens will result in a shifted diffraction pattern, which can then be measured [92]. From the measured shift in the pattern, the actual dimensional difference between the specimens can be calculated, and the inherent strain and the residual stresses can be calculated from this [92]. Therefore, an orthogonal coordinate system is necessary for establishing mathematical relationships between the strain and the inter-planar spacing, such as in Figure 3-4 [92].

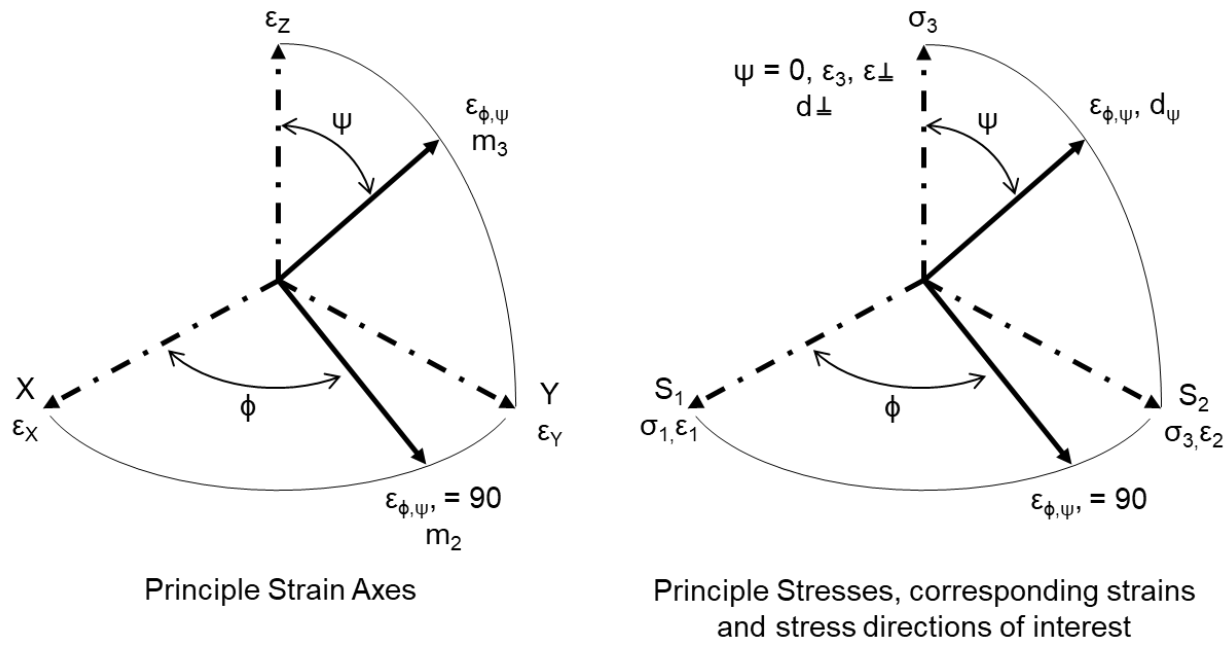

Figure 3-4: Coordinate system used for calculating surface strain and stresses. Note that ε_z and σ_3 are normal to the specimen surface (adapted from [92])

The main characteristics of this coordinate system are that the angle between the Z-axis and the XY plane is referred to as ψ, and the angle between the XZ plane and the Y-axis is referred to as ϕ. These angles are always perpendicular to each other [92]. Keeping this in mind and referring to the XRD method, it can be safely assumed that $\sigma_3 = 0$ since the measurements are made within the surface [92]. The strain ε_z will not be zero in this case but can be measured through experiments, where the peak position is used (2θ) and d_n in Bragg's Law. This becomes

$$\varepsilon_z = \frac{d_n - d_0}{d_0} \qquad \textbf{(3.21)}$$

if the unstrained inter-planar spacing (d_0) is known [92].

Therefore, the strain within the component surface can be calculated by comparing the strained to the unstrained lattice spacing [92]. Equation (3.21) is suitable for measurements normal to the surface; however, as seen in Figure 3-5, the formula needs to be altered for specimens that are tilted inside the diffractometer [92].

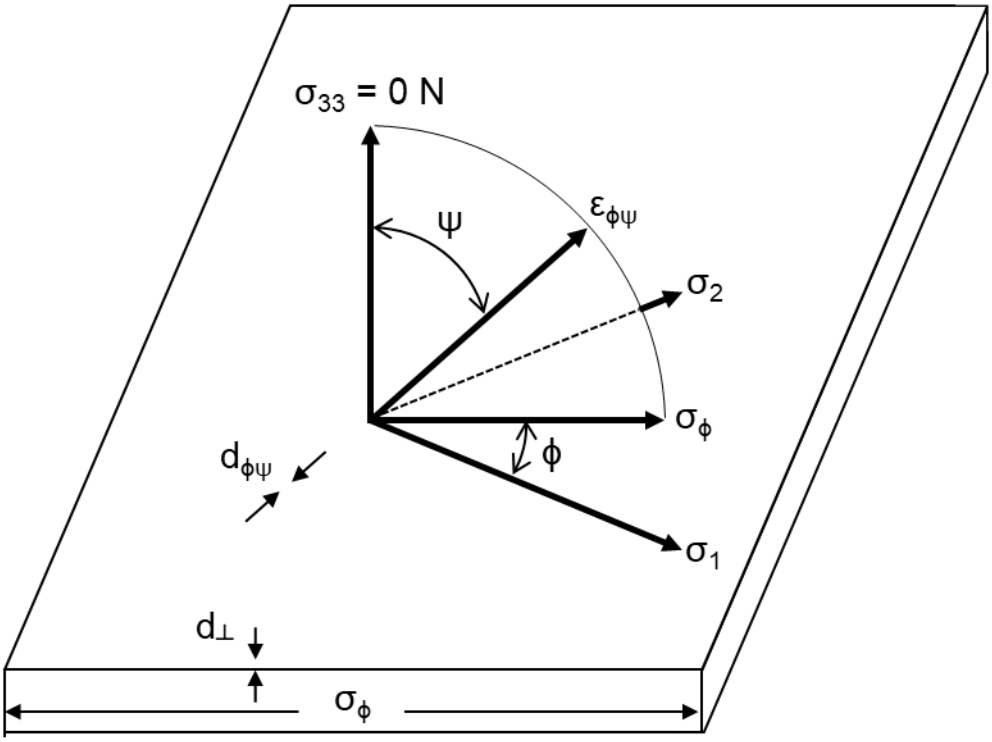

Figure 3-5: Schematic showing diffraction planes parallel to the surface and at an angle φψ. Note σ_1 and σ_2 both lie in the plane of the specimen surface (adapted from [92])

For planes measured at an angle ψ, Equation (3.22) is used [92].

$$\varepsilon_{\psi} = \frac{d_{\phi\psi} - d_0}{d_0} \tag{3.22}$$

3.2.4 Stress Determination

Determining the stresses present in the component is the primary goal of this study and will be discussed here. Hooke's law states that:

$$\sigma_y = E\varepsilon_y \tag{3.23}$$

An assumption is further made that $\sigma_z = 0$ (a state of plane stress exists) and the stresses are biaxial [92]. In this condition, Poisson's ratio (v) describes the ratio of the transverse to longitudinal strains, as in Equation (3.24).

$$\varepsilon_x = \varepsilon_y = -v\varepsilon_z = -\frac{v\sigma_y}{E} \tag{3.24}$$

Since the XRD is measured at the surface of the component, where $\sigma_z = 0$, it follows that:

$$\varepsilon_z = -v(\varepsilon_x + \varepsilon_y) = -\frac{v}{E}(\sigma_x + \sigma_y) \quad \textbf{(3.25)}$$

Combining Equations (3.21) and (3.25):

$$\varepsilon_z = \frac{d_n - d_0}{d_0} = -\frac{v}{E}(\sigma_x + \sigma_y) \quad \textbf{(3.26)}$$

Equation (3.26) is only applicable to a general case, specifically where the principal stresses can only be acquired as a sum and the d_0 value is yet to be determined [92]. To measure single stresses in a specific direction in the surface σ_ϕ, elasticity theory is used to show that the strain along a tilted path is given by Equation (3.27) [92].

$$\varepsilon_{\phi\psi} = \frac{1+v}{E}(\sigma_1 \cos^2\phi + \sigma_2 \sin^2\phi)\sin^2\psi - \frac{v}{E}(\sigma_1 + \sigma_2) \quad \textbf{(3.27)}$$

It can further be shown that, if the strains are used to calculate the stresses in any chosen direction from the inter-planar spacing, the stress is given by the following [92]:

$$\sigma_\phi = \frac{E}{(1+v)\sin^2\psi}\left(\frac{d_\psi - d_n}{d_n}\right) \quad \textbf{(3.28)}$$

Using the most common XRD method of $\sin^2\psi$, where a linear graph of lattice spacing (d) depending on $\sin^2\psi$ is obtained by multiple measurements through different angles, the gradient (m) of the d vs $\sin^2\psi$ curve is used in the stress calculation [92]. Assuming zero stress at $d = d_n$ where d is the y-axis intersection when $\sin^2\psi = 0$, the stress is given by Equation (3.29) [92]:

$$\sigma_\phi = \left(\frac{E}{1+v}\right) \times m \quad \textbf{(3.29)}$$

The above Equations form the basis of the XRD measurement technique [92].

3.3 Residual Stresses from the Inherent Strain Method

The inherent strain method was initially developed for simulating welding processes but has been adapted for PBF simulations [94]. This technique uses residual plastic strain tensors (or inherent strain tensors) to simulate the thermal stress build-up at a component scale by activating the tensors in each hatching region of a macro-scale mechanical model in a layer-by-layer fashion [94]. The material along the weld path will experience rapid heating, melting, solidification and cooling cycles during a welding process, resulting in large temperature gradients and complex deformation paths [95]. As a result, thermal strain and mechanical strain will form during the process [95]. It is helpful to consider two discrete points in the material, points A and B, to visualise the formation of the inherent strain under these circumstances, as in Figure 3-6.

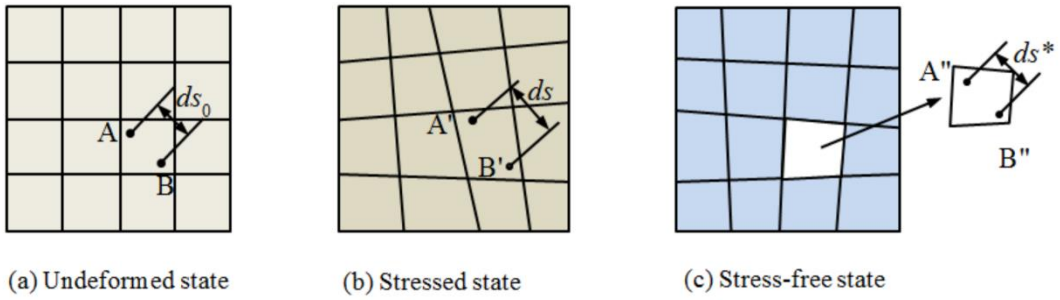

Figure 3-6: Original definition of inherent strain for welding mechanics (with permission of [95])

Defining the (infinitesimally small) distance between the points in the undeformed state, stressed state, and stress-relieved state as ds_0, ds, and ds^*, respectively, the inherent strain can be given by Equation (3.30) [95].

$$\varepsilon^* = \frac{ds^* - ds_0}{ds_0} \tag{3.30}$$

Equation (3.30) presents the residual strain in the stress-relieved state compared to the undeformed state, which is the definition of inherent strain. The component is cooled down to room temperature after the welding process, allowing the thermal strains to be disregarded [95]. Equation (3.30) is rearranged and produces Equation (3.31) [95].

$$\varepsilon^* = \frac{ds - ds_0}{ds_0} - \frac{ds - ds^*}{ds_0} \tag{3.31}$$

Since infinitesimal distances are considered, an assumption can be made that ds is essentially equal to ds_0 allowing the further rewriting of Equation (3.31) to form Equation (3.32) [95].

$$\varepsilon^* = \frac{ds - ds_0}{ds_0} - \frac{ds - ds^*}{ds} \tag{3.32}$$

In this Equation, the first term on the right-hand side is the total mechanical strain ε present after the welding process completes, and the second term is the mechanical elastic strain ε_{el} [95]. In this case, the mechanical elastic strain is directly proportional to the stress released from the material [95]. Equation (3.32) can therefore be rewritten as:

$$\varepsilon^* = \varepsilon_{total} - \varepsilon_{el} \tag{3.33}$$

Other strains may also be present in the welding process, such as strains induced by phase transformation and creep (denoted as ε_{pt} and ε_{cr}, respectively) [96, 97]. After welding, the total strain in a component will be the sum of all these strains, as shown in Equation (3.34) [96-98].

$$\varepsilon_{total} = \varepsilon_{el} + \varepsilon_{pl} + \varepsilon_{th} + \varepsilon_{pt} + \varepsilon_{cr} \quad \textbf{(3.34)}$$

The inherent strain ε^* refers to the strain remaining in the weld at equilibrium (after cooling to ambient temperature), which means that the elastic strain may be left out since only plastic strains contribute to the total inherent strain [96-98]. Therefore, the inherent strain is given by Equation (3.35), which is the same as Equation (3.33).

$$\varepsilon^* = \varepsilon_{total} - \varepsilon_{el} = \varepsilon_{pl} + \varepsilon_{th} + \varepsilon_{pt} + \varepsilon_{cr} \quad \textbf{(3.35)}$$

The strains caused by phase transformation and creep are neglected for simplification, and the thermal strains are assumed to equal zero after cooling, which leads to the inherent strain being equal to the plastic strain, as seen in Equation (3.33) [96-98].

$$\varepsilon^* = \varepsilon_{pl} \quad \textbf{(3.36)}$$

Equation (3.36) is valid for the welding process but not for an AM process [95]. Since the SLM process is more complicated than a simple welding process, this original inherent strain theory is not accurate when applied to SLM components, mainly because of the effects new layers have on those underneath [97-99]. Shrinkage of upper layers affects the elastic deformation in lower layers, invalidating the assumption that only the plastic strain will contribute to the inherent strain [97]. Considering the time-dependant shrinking and expanding of layers, the inherent strain will also be a time-dependent or rather a processing-history-dependent quantity, unlike the original theory's assumption that the inherent strain is only dependent on the final cooled state [97]. Regardless, it is assumed that each layer (or small group of consecutive layers) will experience the same thermal history and comparable mechanical restraints to those applied to the already solidified layers [97]. These similarities provide grounds for justifying the assumption that only a small volume (representative of the entire build) needs to be fully simulated, saving large amounts of time [97]. These assumptions lead to a modified inherent strain theory proposed by Liang et al. [97], which incorporates the contribution of plastic deformation and thermal shrinking coupled with the inter-layer effect. According to this theory, the plastic strain that SLM components experience after a laser pass (during rapid solidification) is considered to be directly influenced by the thermal strain [97]. For discussion purposes, the term "intermediate state" will be used to refer to the point in time of manufacturing when the compressive plastic strain (caused by the rapid solidification phenomenon) reaches its maximum value [97]. The contribution of the plastic deformation to the inherent strain may then be given as Equation (3.37) [97].

$$\varepsilon_{pl}^* = \varepsilon_{pl}^l \quad \textbf{(3.37)}$$

In Equation (3.37), ε_{pl}^{l} is the maximum value of the compressive plastic strain at the intermediate state as described above [97]. During the intermediate state, elastic deformation starts to accumulate [97]. Considering the SLM process where residual stresses and deformation manifest due to the lower layers restricting the shrinkage of the upper layers, the contribution of this phenomenon should also be accounted for in the inherent strain method [97]. After the process completes, the component cools down, during which the elastic strain changes [97]. This state is referred to as the "steady-state" for discussion purposes [97]. Elastic strains forming before this stage represents the conversion of thermal strain to mechanical strain [97]. These elastic strains are added to the plastic strains, which completes the rest of the modified inherent strain model for AM (and, in effect, SLM) [97]. The addition of the elastic strains is defined in Equation (3.38).

$$\varepsilon_{th}^{*} = \varepsilon_{el}^{I} - \varepsilon_{el}^{S} \quad \textbf{(3.38)}$$

In the above Equation, ε_{el}^{I} is the elastic strain formed during the intermediate state and ε_{el}^{S} is the elastic strain at the steady-state [97]. Finally, the inherent strain model amounts to Equation (3.39) [97].

$$\varepsilon^{*} = \varepsilon_{pl}^{*} + \varepsilon_{th}^{*} \quad \textbf{(3.39)}$$

CHAPTER 4 METHODOLOGY

4.1 Introduction

During this study, surface residual stresses in specimens of the same dimensions were evaluated using three different techniques: XRD, the inherent strain method and the Vickers-micro-indentation method. The XRD measurements were used as the trusted values of the surface residual stresses in the specimens. In addition, the values obtained from the Vickers micro-indentation method were compared to the XRD values for investigating the efficacy and accuracy of the Vickers micro-indentation method. Finally, to validate the XRD results, the inherent strain method was used by conducting simulations of the SLM process. The diagram in Figure 4-1 depicts the methods used.

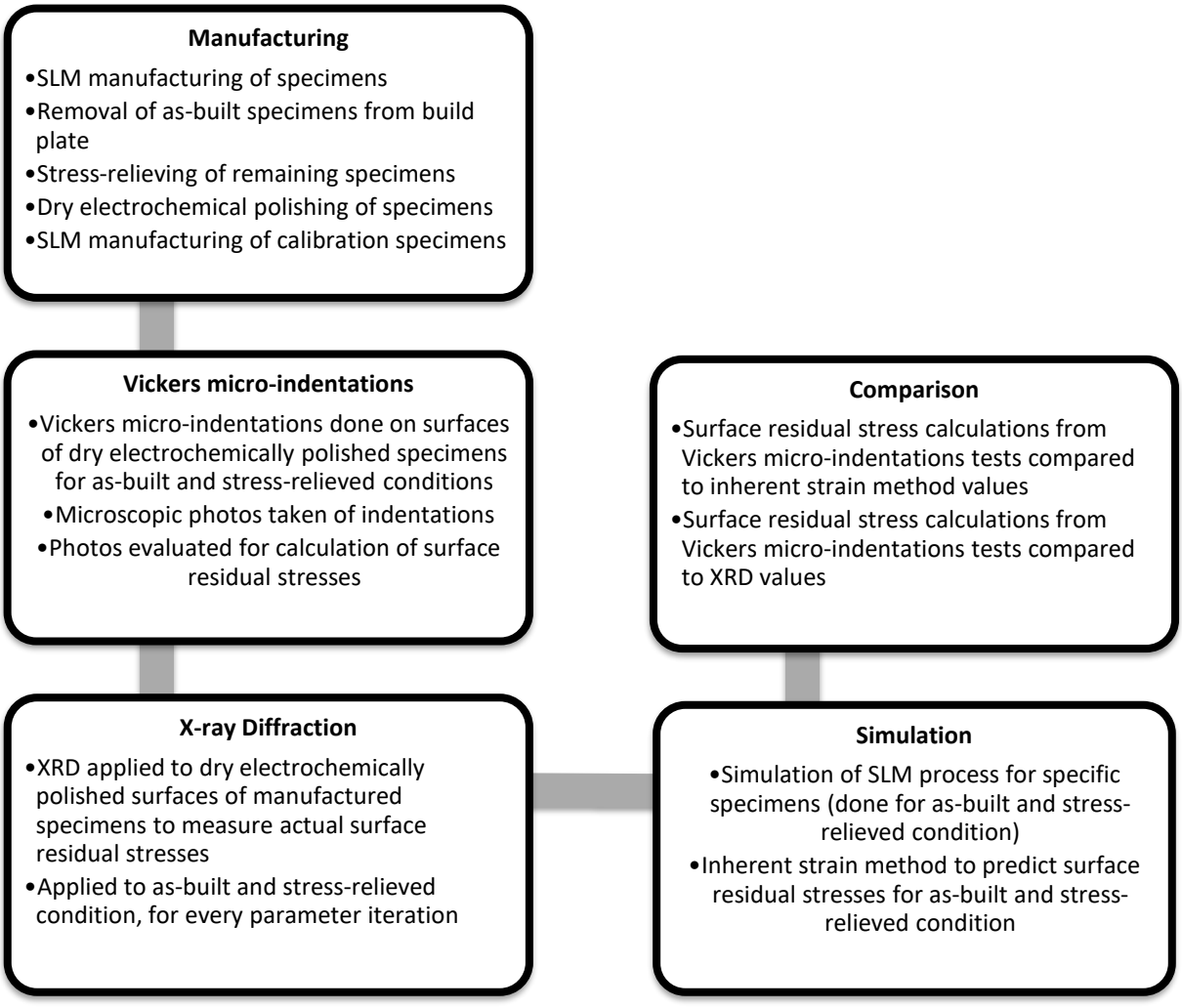

Figure 4-1: Diagram of methods used in current study

4.2 Manufacturing and Preparation of Specimens

4.2.1 SLM Machine and Powder

A COHERENT Creator™ SLM machine was used to manufacture all specimens. This SLM machine utilises a Yb: Fiber laser of max 250 W and laser wavelength of 1070nm. Cylindrical build volume dimensions are 100 mm (diameter) by 110 mm (height). A scraper does the material deposition, and Nitrogen gas is used to create an inert atmosphere with flow direction from the back of the build chamber towards the front. The powder used was gas atomised IN718 powder (with designation TruForm™ 718-35) acquired from Praxair. The chemical composition of the powder is shown in Table 4-1 [27].

Table 4-1: Actual vs nominal (max) chemical composition for IN718 powder (in wt.%)

Element	Nominal composition [wt.%] [27]	Praxair Truform™ typical composition [wt.%]	Element	Nominal composition [wt.%] [27]	Praxair Truform™ typical composition [wt.%]
Carbon	0.08 (max)	0.04 (total)	**Niobium + tantalum**	4.75: 5.50	5.16
Manganese	0.35 (max)	0.02	**Titanium**	0.65: 1.15	0.93
Silicon	0.35 (max)	0.04	**Aluminium**	0.2: 0.8	0.50
Phosphorous	0.015 (max)	0.006	**Iron**	remainder	18.22
Sulfur	0.015 (max)	0.001	**Copper**	0.3 (max)	0.02
Chromium	17.0: 21.0	18.99	**Nickel**	50.00: 55.00	52.93
Cobalt	2 (max)	0.10	**Boron**	0.006 (max)	0.001
Molybdenum	2.80: 3.30	3.00			

Powder morphology was evaluated using SEM imaging and can be seen in Figure 4-2.

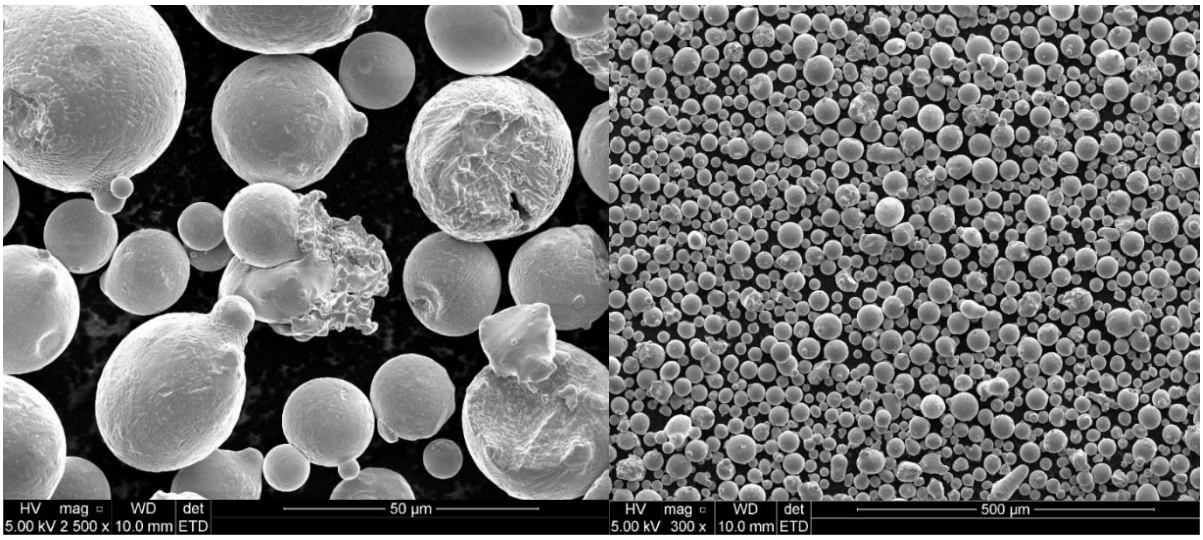

Figure 4-2: Powder morphology and size distribution

From Figure 4-2, it was observed that the powder particles were spherical, with only a few irregular particles present. Some satellites are present that are attached to the larger particles. According to the Certificate of Analysis and Certificate of Conformity (obtained from Praxair), this powder batch had a Hausner ratio of 1.18, an apparent density of 4.26g/cm^3, and a tap density of 5.01g/cm^3. Particles ranged in size from about 14-54µm.

4.2.2 Specimens for XRD and Vickers Indentation Testing

Since the study focuses on comparing data between different methods, specimens were manufactured for each method to be applied; specifically, for utilising the XRD method and the Vickers micro-indentation method. Therefore, cuboid specimens were manufactured according to the quantities and conditions in Table 4-2 to ensure enough comparable data.

Table 4-2: Breakdown of specimens manufactured

Parameter varied	***Post-process condition***		*Total per hatch distance*
Hatch distance [mm]	As-built	Stress-relieved	
0.120	3	3	6
0.114	3	3	6
0.108	3	3	6
Total per condition	9	9	18

It was decided that the efficacy of the Vickers micro-indentation method is to be evaluated under six unique circumstances, including three different values of a specific processing parameter and

two post-processing conditions. The process parameter chosen was hatch distance. A total of 18 specimens were evaluated using two different techniques. The specimens were in the shape of cubes with 10x10x10 mm^3 dimensions with 4 mm high support structures. Specimens were divided into condition-parameter sets (as-built and stress-relieved for each hatch distance), resulting in six condition-parameter sets. Cuboid specimens with dimensions 10x10x10 mm^3 were manufactured according to the process parameters in Table 4-3.

Table 4-3: Process parameters used for cuboid specimens

Hatch overlap [%]	Power [W]	Scan speed [mm/s]	Hatch distance [mm]	Layer thickness [mm]	Laser Spot size [mm]	Scan pattern	VED [J/mm^3]
0	107.3	630	0.120	0.025	0.120	Bi-directional raster	56.77
5	107.3	630	0.114	0.025	0.120		59.76
10	107.3	630	0.108	0.025	0.120		63.08

All cuboid specimens were manufactured with 45° rotation between layers. It should be noted that, since the SLM machine manufactured the specimens with a contour and infill hatch, the parameters given are for the infill hatch only. The contour parameters differ in the laser power, spot size and scan speed values, which were 120.02 W, 0.04 mm and 250 mm/s, respectively. Moreover, the software of the SLM machine used could only alter hatch distances by specifying the percentage overlap of the spot size. Hatch overlap was converted to actual hatch distance with the formula in Equation (4.1) from the theoretical diagram in Figure 4-3.

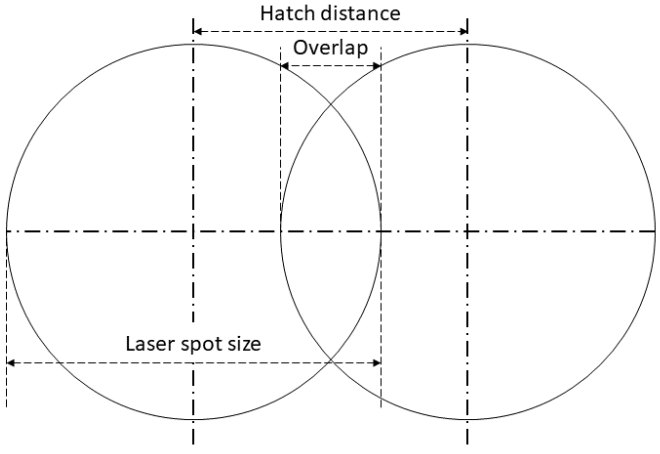

Figure 4-3: Diagram of hatch distance calculation

The laser spot size is the diameter of the focal point of the laser on the powder bed [50]. Hatch distance is the distance between two parallel laser passes; therefore, it is the distance between the centres of the laser focal points (the circles as seen in Figure 4-3.

$$HD\ [mm] = LSS\ [mm] - (LSS\ [mm] * OL\ [\%]) \quad \textbf{(4.1)}$$

In Equation (4.1), HD is the hatch distance, LSS is the laser spot size and OL is the overlap percentage. The part of the Equation in brackets is the overlap distance, as shown in Figure 4-3. All six cubes were manufactured on the same build plate for each hatch distance used. After manufacturing, three cubes were removed from the build plate by grinding off the support structure at 3 mm from the build plate surface, leaving 1 mm of support structure on the bottom of the cubes. The remaining 1 mm support structure was removed using wire EDM cutting. The remaining cubes were then heat-treated for stress-relieving purposes while remaining attached to the build plate. These stress-relieved specimens were removed from the build plate utilising wire EDM cutting within 1 mm from the bottom of the cubes. The cubes were manufactured with the sides marked with “X” at the back of the machine. One of the three sets of cubes (with their orientation) is shown in Figure 4-4.

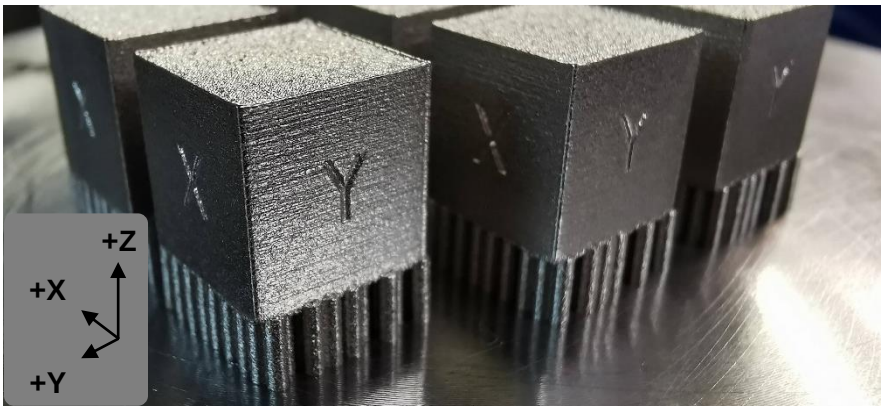

Figure 4-4: Cuboid specimens on build plate

Figure 4-5 shows some stress-relieved cubes on the left and the eight 0 % hatch overlap cubes on the right-hand side. The darker cubes on the right-hand side are the stress-relieved cubes.

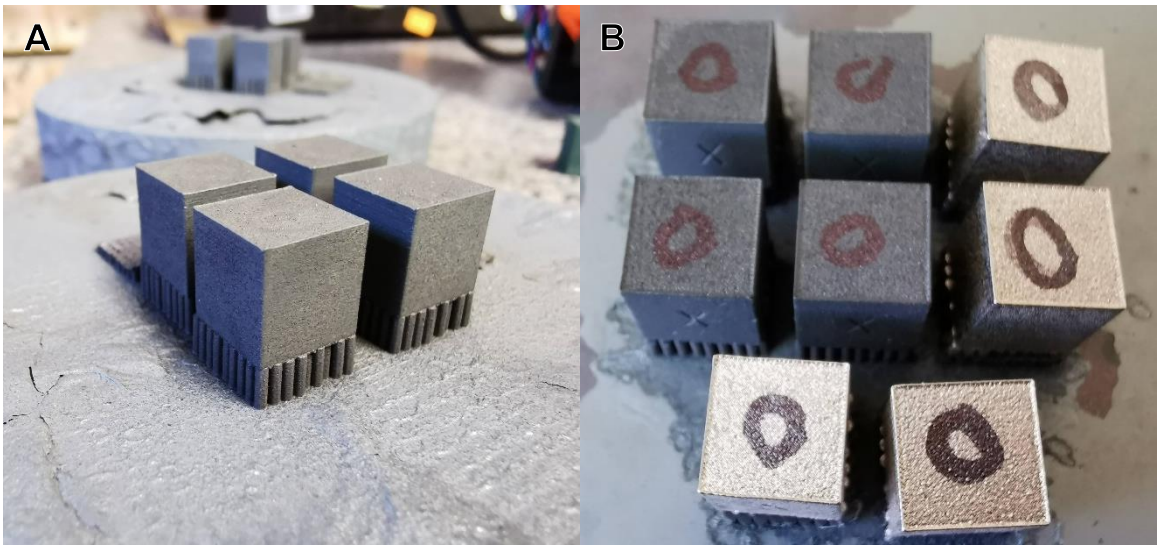

Figure 4-5: Cubes after stress-relief (A) and all 0% hatch overlap cubes on the build plate (as-built cubes ground off) (B)

The 45° scan lines are visible on the top faces of the cubes in Figure 4-5. The contour with which the specimens were manufactured is also visible at the outer perimeter of each cube.

4.2.3 Stress-Relieving of Specimens

Half of the cuboid specimens were stress-relieved using post-processing heat treatment (as per Table 4-2). Stress-relieving heat treatments were done to increase the number of different circumstances under which the Vickers indentation method could be tested. A programmable Nabertherm LH 120/12 GmbH (Lilienthal/Bremen, Germany) oven was used to complete the heat treatment process. The “as-built” cuboid specimens in Table 4-2 were manufactured according to Table 4-3, ground off from the build plate, and the supports removed with wire EDM cutting. In contrast, the “stress-relieved” specimens were manufactured in the same way, after which they were inserted into the oven (whilst still attached to the build plate). The oven was set to ramp-up from 25-1065°C for 240min, held at 1065°C for 90min and cool down from 1065°C to 25°C for 1200min (20h). Finally, these specimens were removed from the build plate utilising wire EDM cutting.

4.2.4 Dry Electrochemical Polishing of Specimens

After the samples were manufactured (and stress-relieved in some cases), the surfaces to be tested were dry electrochemically polished with a DLyte 1D polishing machine (GPAINNOVA, Spain), using CoCr Group: DLyte 01 for S1 Electrolyte. Since we did not have access to electrolytes specifically for IN718, some settings needed to be changed on the machine for the

CoCr electrolyte to sufficiently polish the cubes. The voltage was increased from 28V to 31V, and the humidity was also increased to amplify the current through the cubes. The positive and negative charge times were 200s and 280s, respectively. All cubes were sand-blasted after the first polishing cycle, with 25-70μm sand particles at a pressure of 4 bar for 4s to 8s per face. The voltage was increased to 35V, and the humidity was increased once again using the input parameters on the DLyte machine.

Cube surfaces were measured with an Amittari Dobamoni Surface Roughness Tester (DR-432B). According to the recommended operating parameters, the machine has a diamond probe pin with a 5μm radius and an accuracy of no more than ±10 %. Even though the accuracy is not sufficient for roughness testing, it provided insight into the smoothness of the cube surfaces for Vickers indentation testing. A Gaussian profile was used with a cut-off length of 2.5 mm to determine the Ra values across each surface. After sand-blasting, average surface Ra values were around 3.7μm for the X face and 3.0μm for the Y face. Polishing for 1 hour, washing the specimen and polishing for another hour reduced the average surface Ra values to around 1.1μm for the X faces and 0.8μm for the Y faces. The values differed slightly amongst all the polished cubes; therefore, polishing was deemed successful if the average surface roughness Ra value was evaluated to be lower than 1.5μm. The six cube specimens to be measured using XRD were sent for analysis after the polishing was done.

Two more polishing cycles were done on the cubes to be Vickers indented. Again, these surfaces were evaluated under a microscope to visually determine the number of irregularities still present on the surfaces. Polishing done during these cycles resulted in removing more of the surfaces of the cubes; however, it was necessary for obtaining sufficiently smooth surfaces for Vickers indentations to succeed.

4.3 Vickers Micro-Indentations

Two cuboids for each condition-parameter set were micro-indented using an M-400 Vickers hardness tester (manufactured by LECO) with a force of 0.5kgf for a period of 10s. Vickers micro-indentations were performed on two faces (the X-Z and Y-Z faces) of two cuboids in each condition, at locations depicted in Figure 4-6.

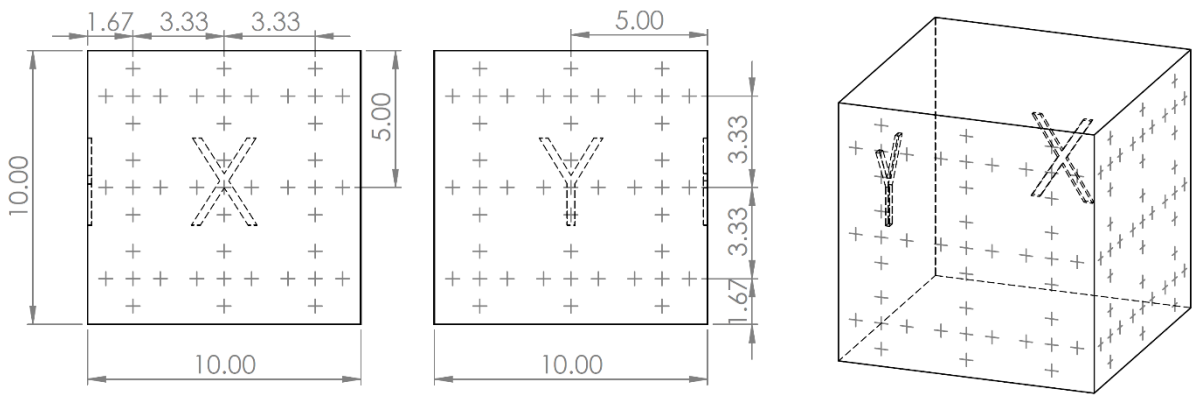

Figure 4-6: Vickers indentation locations for 1st cuboid group (Please note that the "+" marks are not to scale and are only indications of the actual micro-indentation locations)

These indentations were then photographed using scanning electron microscopy (SEM) on a Phenom Pro Desktop SEM machine (Phenom-World BV., Eindhoven, Netherlands). Photographs were taken using the 'Topo A' feature, which meant that only one of the two available detectors were used, providing topographical data and more precise perimeters for measuring purposes. The actual area and diagonal lines of each centre indentation were measured using FIJI (ImageJ) software. Nominal areas were calculated using the two diagonal line lengths, and all measurements were used to calculate the surface residual stresses according to Equation (3.16) derived in Chapter 3. Finally, von Mises stresses were calculated for comparative reasons using Equation (3.17).

In addition to the centre indentations, four more were done for each location; at the top, bottom, left and right positions of the centre indentations, as illustrated in Figure 4-6. The actual distances between the surrounding indentations and the centre indentations were within 300μm. These extra indentations were taken to visually compare the geometries between indentations within small distances from another since they are expected to be nearly identical. One cuboid in each condition-parameter set was indented in this way (six cuboids in total), whereas one cuboid in each condition-parameter set was indented at the centre locations with an additional indentation at the top and bottom, as shown in Figure 4-7.

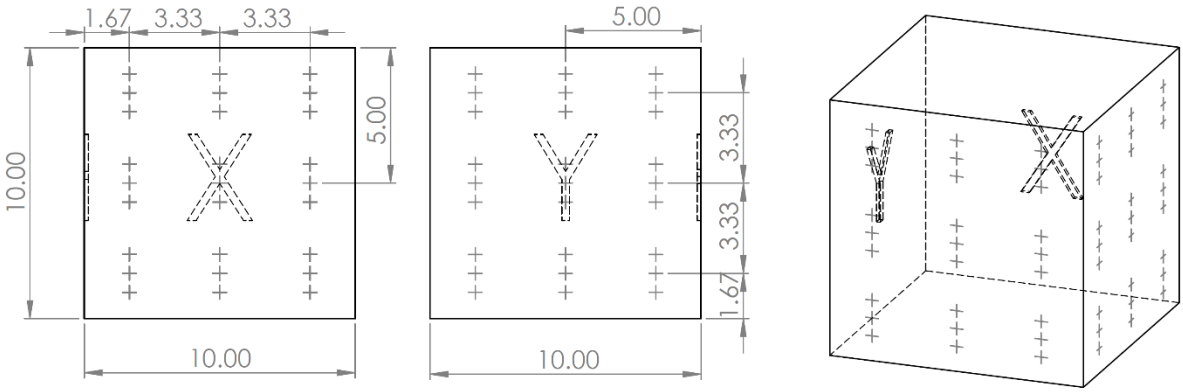

Figure 4-7: Vickers indentation locations for 2nd cuboid group (Please note that the "+" marks are not to scale and are only indications of the actual micro-indentation locations)

Therefore, 90 micro-indentations were done per cuboid (for the 1st cuboid group) and 54 micro-indentations for the 2nd cuboid group, which amounts to a grand total of 864 micro-indentations taken across all the cuboid specimens.

4.4 Experimental X-Ray Diffraction

XRD was done on the centre locations of one cube's X and Y faces in each condition-parameter set using the parameters presented in Table 4-4.

Table 4-4: Parameters used for XRD evaluation

Parameter	Value
Structure	FCC
Indices (hkl)	311
Diffraction angle 2θ [°]	152
Target	Mn
Target voltage [kV]	25
Target current [mA]	5
Exposure diameter [mm]	2
X-ray incident angle [°]	0; ±8.23; ±14.06; ±27.0

Phi angles were chosen according to the coordinate system shown in Figure 4-8.

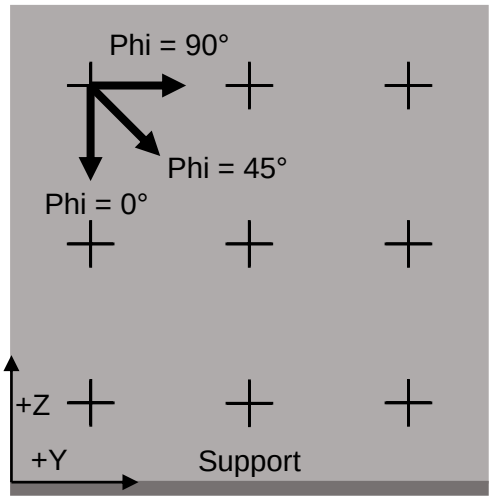

Figure 4-8: XRD coordinate system

Residual stress measurements were taken on the three phi angles shown in Figure 4-8, and the maximum and minimum residual stress values were calculated from these measurements. In addition, maximum shear stresses were also calculated from the measured values. Obtained values were then compared to the data obtained from the Vickers micro-indentation method.

CHAPTER 5 SIMULATIONS (INHERENT STRAIN METHOD)

5.1 Manufacturing of Specimens for Simulation Calibration

Cantilever specimens were manufactured for calibration of the simulation software (using the inherent strain method). The cantilevers' CAD files were obtained directly from the software to ensure exact dimensions and accurate results. Four cantilever specimens were manufactured with the same process parameters as the cubes but with varying scan patterns. Cantilevers were manufactured with a bi-directional raster scan pattern, with no rotation between layers, for three cases: one with scan direction in the longitudinal direction, one with scan direction in the transverse direction and one at 45° with respect to the previous two. Images of these cantilevers are visible in Figure 5-1 (the black arrows indicate scan direction).

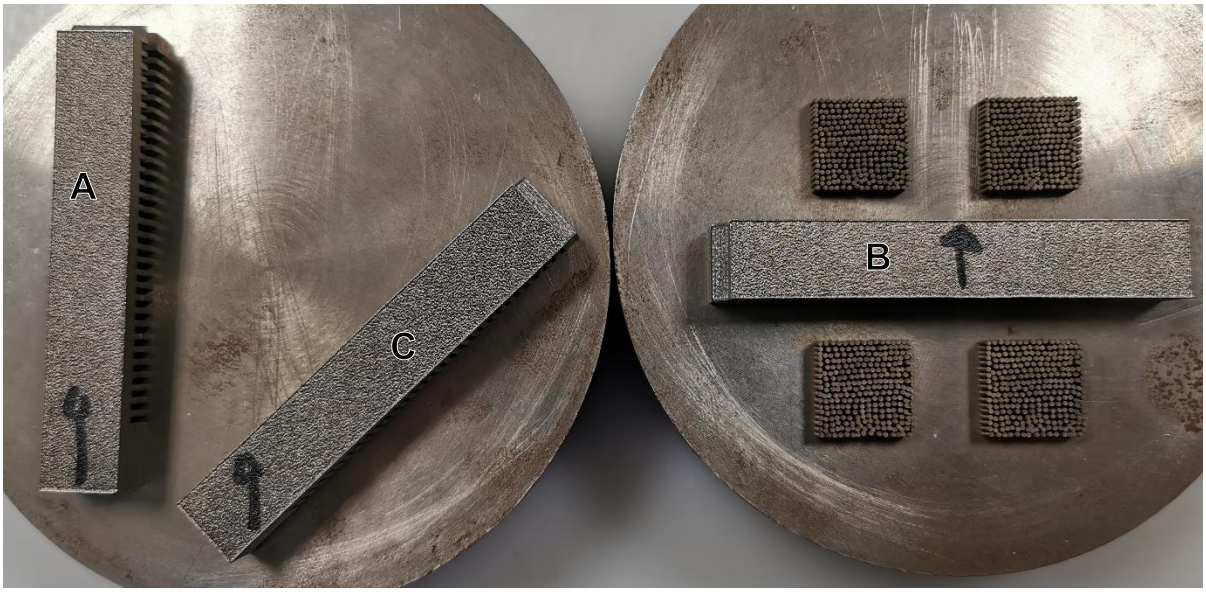

Figure 5-1: Cantilever specimens for calibration (A) longitudinal, (B) transverse and (C) 45°

Cantilever A and B were used for orthotropic calibration of the simulation software. In addition, another cantilever was manufactured with a bi-directional scan pattern and 45° rotation between layers, which was used for isotropic calibration purposes. After manufacturing, the cantilevers were wire-EDM cut, and the displacements of the top halves of the cantilever specimens were measured and input into the simulation software for calibration purposes, which will be described further.

5.2 Simulation Calibration

Simufact Additive has the ability to calibrate for two distinct types of simulations, namely orthotropic and isotropic, where the orthotropic case calibrates for different inherent strain values in the X and Y directions, and the isotropic case calibrates a single value for both directions. The orthotropic simulation is useful for simulating SLM components with no rotation between layers, and the isotropic simulation is adequate for the case of rotation between layers. During all calibration and simulation processes, identical parameters were used, which are presented in APPENDIX A.

5.2.1 Mechanical Orthotropic Calibration

Calibrating the simulation software requires cantilevers to be wire-EDM cut and their displacements measured. Displaced cantilevers can be seen in Figure 5-2.

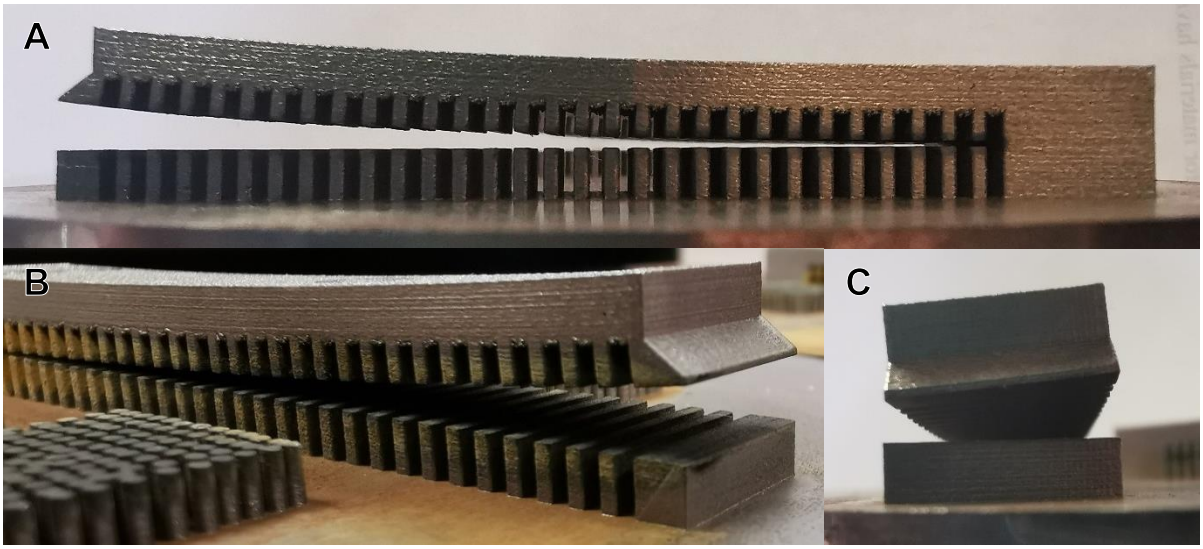

Figure 5-2: Cut, displaced cantilevers (A) longitudinal, (B) transverse and (C) 45°

Displacement values of the three cantilevers are shown in Table 5-1. The difference between the displacements of the longitudinal and transverse cantilevers is a clear indication of the anisotropic nature arising from the manufacturing technique, specifically the scan pattern (0° rotation between layers). The anisotropic nature of SLM IN718 is frequently mentioned in literature [2, 7, 9, 13, 44, 100].

Table 5-1: Cantilever displacements

Cantilever	Measured Displacement [mm]	
A. Longitudinal	3.087	
B. Transverse	1.497	
C. 45°	2.725	1.68

Displacements were measured at the centres of the top lip, at the highest points, as shown in Figure 5-3.

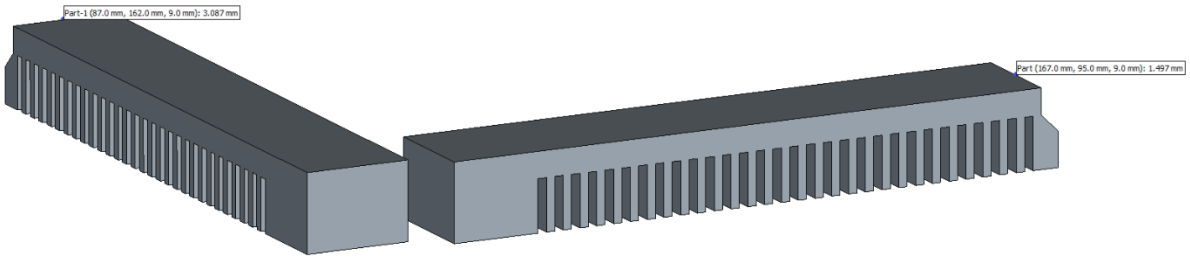

Figure 5-3: Measuring points for longitudinal ("Part-1") and transverse ("Part") cantilevers

For the 45° cantilever, the corners on both sides of the cantilever's top lip were measured. As can be expected, the amounts of deformation correlated with those of the longitudinal and transverse cantilevers, since the 45° cantilever deformed more on the side closest to where the longitudinal cantilever would have been. Calibration of the inherent strain method relied on the software's capabilities to incorporate the actual longitudinal and transverse cantilever displacements in its simulation of the building and cutting processes of the 45° cantilever. These displacements were measured using micrometers and vernier callipers, and the values of the longitudinal and transverse scan direction cantilevers were input into the simulation software. The displacement of the 45° scan direction cantilever was used later for comparison. The software was calibrated to produce the same displacement values (to within 1 %) of the manufactured cantilevers. These values are shown in Table 5-2.

Table 5-2: Calibration values of longitudinal and transverse cantilevers

Part	z_{max} target [mm]	z_{max} sim [mm]	Δz_{max} [mm]	Δz_{max} [%]
Part-1	3.087	3.06	-0.027	0.134
Part	1.497	1.499	0.002	0.875

The build and cutting processes of the 45° cantilever were then simulated and compared to the deformation values of the manufactured version. Figure 5-4 shows the manufactured cantilever on the left and the simulated cantilever on the right, showing the efficacy of the inherent strain method.

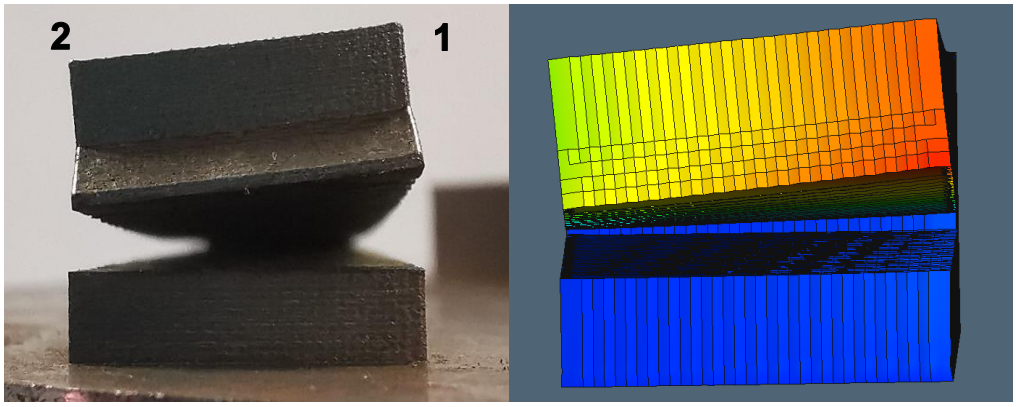

Figure 5-4: Comparison between manufactured and simulated 45° cantilevers

The simulation results (incorporating the calibrated values from the longitudinal and transverse cantilevers) of the 45° cantilever are shown in Table 5-3. Points 1 and 2 are shown in Figure 5-4.

Table 5-3: Simulation values of 45° cantilever

Simulation [mm]		Measured [mm]		Difference [%]	
Point 1	Point 2	Point 1	Point 2	Point 1	Point 2
2.711	1.626	2.725	1.680	0.531	3.228

It is worth noting that, during manufacturing, the SLM machine created a contour at the outer surfaces of the cantilevers (as shown in Figure 5-5, depicted with white arrows), which influenced

the values of the displacement values measured. The scan direction is also visible in Figure 5-5, indicated by the black arrow.

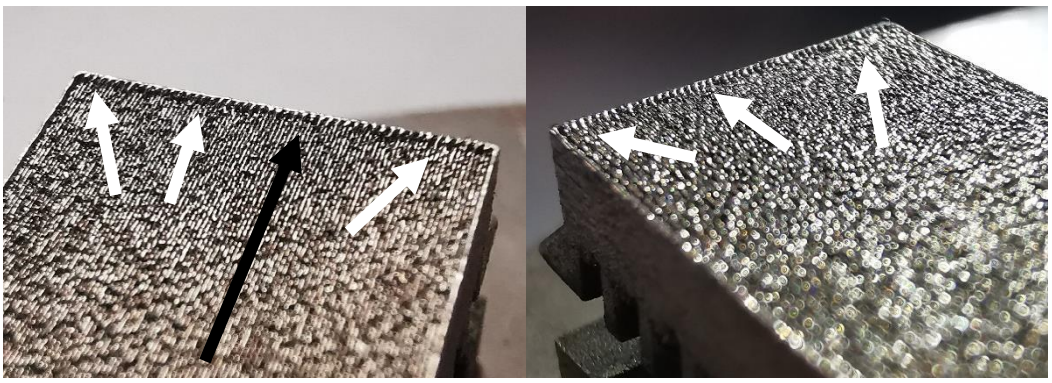

Figure 5-5: Longitudinal cantilever contour

These contours extended an average of 0.12 mm above the top of the cantilever surfaces (measured with a vernier calliper) and were present because of the default settings used in the slicing software, which were set to manufacture the specimens with a contour pattern followed by the applicable layer's infill hatch. Default process parameters used by the SLM machine for the contours are given in Table 5-4.

Table 5-4: Contour process parameters

Hatch overlap [%]	Power [W]	Scan speed [mm/s]	Hatch distance [mm]	Layer thickness [mm]	Spot size [mm]	Inert gas
0	120.02	250	0.04	0.025	0.04	Nitrogen

After the effects of these contours on the measured values were considered, the simulated results were within 5 % compared to the actual displacement values, and this way, the software was correctly calibrated and validated. This calibration meant that the software could be used to simulate the cuboid specimens, and accurate results could be expected.

5.2.2 Mechanical Isotropic Calibration

Another cantilever was manufactured with 45° rotation between layers to calibrate the simulation software for the isotropic (mechanical) case. This cantilever was cut in the same manner as the cantilevers for the orthotropic case, and the displacements were measured after deformation. Calibration occurred identically to the orthotropic case, with the only difference being the

assumption that, for the case where rotation between manufacture layers are present, inherent strains (and, ultimately, stresses) are equal in both the X and Y directions.

5.2.3 Thermo-Mechanical Isotropic Calibration

In addition to the orthotropic and isotropic calibrations, a thermal calibration was done using the calibrated values from the isotropic calibration. During the thermo-mechanical calibration, a single point on the centre of the top surface of the cantilever was specified and calibrated to reach a temperature of 2000°C, according to the literature [66]. An exposure energy fraction of 33.5 % was estimated by the thermo-mechanical calibration and used throughout the subsequent simulations. Calibrating in this way incorporates the mechanical values obtained from the isotropic calibration. The calibration accounts for the temperature gradients in the build plate; therefore, the mechanical properties of the build plate needed to be specified. For this purpose, the default C45_baseplate was used as provided by Simufact Material™.

5.3 Simulation Method

After the calibration process, the simulation software used the inherent strain method to simulate the SLM process of manufacturing the specimens and, ultimately, the residual stresses across the surfaces of the specimens. First, cantilevers A and B were used to calibrate the simulation software for the orthotropic solution of cuboid simulations. Next, Cantilever C was used to verify that the calibration was successful by comparing the measured displacement values of this cantilever to the simulated cantilever (at 45° between the transverse and longitudinal cantilever). After this was done, the fourth cantilever (with 45° rotation between layers) was used to calibrate the simulation software for the isotropic solution of cuboid simulations. Since the anisotropic effects of SLM components are mainly dependent on the scanning direction (when no rotation between layers is present), it is assumed that any cantilever with rotation between layers could be used, and the resulting displacements would be the same in the longitudinal as well as the transverse directions.

Various simulations were run, including mechanical (orthotropic and isotropic) and thermo-mechanical (isotropic) simulation types, to acquire a complete idea of the distribution of residual stresses across the surfaces of the specimens. Stress relief simulations were enabled by using temperature and time tables that the simulation software could use. Data obtained from the simulations could then be exported for use by external programs. MatLab was used to evaluate and extract specific simulation values at the locations used for the Vickers indentation methods. Nine data points surrounding the location of interest were extracted and averaged for this purpose.

CHAPTER 6 RESULTS

This chapter discusses some aspects of the manufacturing and sample preparation process, after which the results are given. A comparison of data is then made in Chapter 6.

6.1 Vickers Micro-Indentation Tests

6.1.1 Microscopic Evaluation

SEM images were taken of each indentation across all indented specimens as described in Vickers Micro-Indentation. An SEM photograph of one group of these indentations (taken on the X face of a cube in the stress-relieved condition, at the bottom centre location) is shown in Figure 6-1.

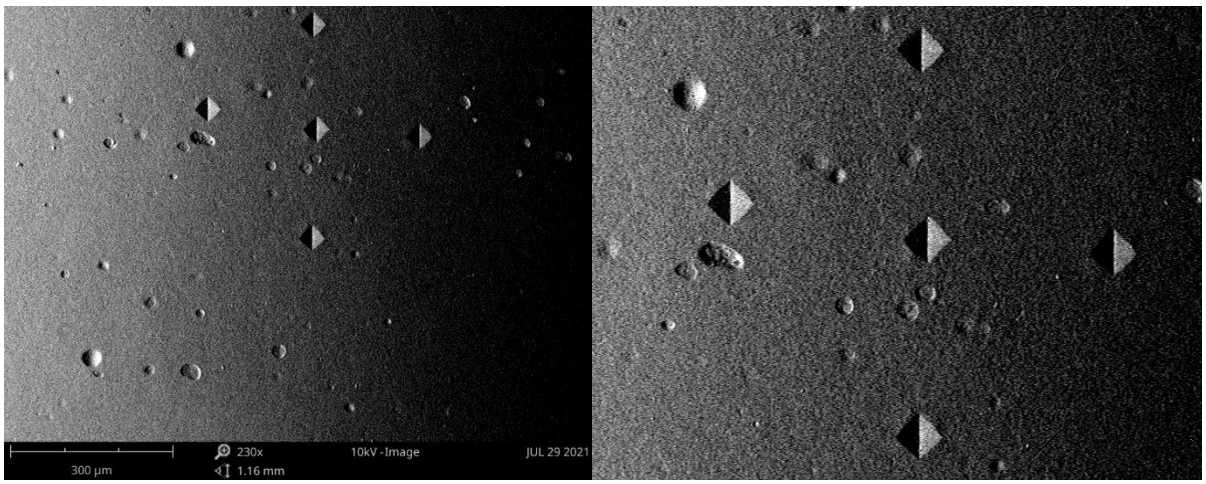

Figure 6-1: SEM photograph of all indentations on a stress-relieved cube on the X face, at the bottom centre location

As shown in Figure 6-1, all surrounding indentations were within 300µm of the centre indentation. Indentations were not made within 2.5 times the diagonal length of each other since this may have influenced the obtained data [82, 101]. However, some surface defects were still present, and individual indentations were made as close as possible to the chosen location while avoiding the defects. The individual indentations of this specific location are shown in Figure 6-2.

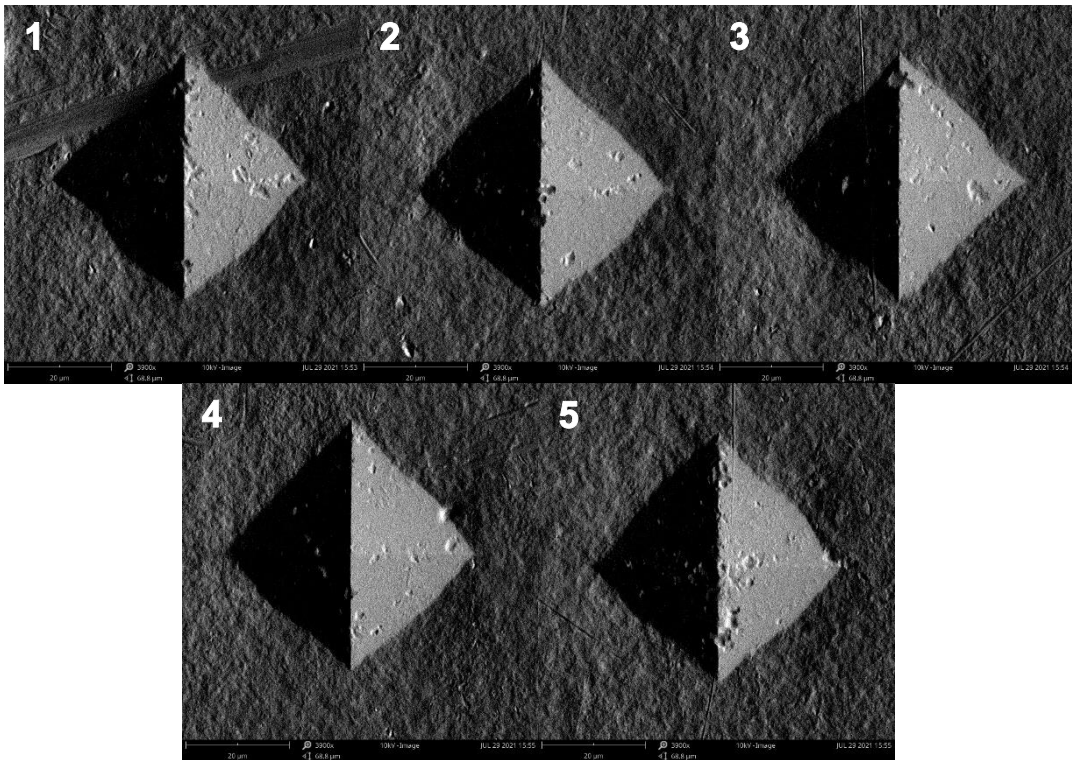

Figure 6-2: Indentation designations: top (1); left (2); centre (3); right (4); bottom (5)

Indentations depicted in Figure 6-2 clearly show differences between indentation geometries, which, however slight, may ultimately lead to varying residual stress values, which should not vary too much in such proximity. In cases where centre locations could not be measured, whether due to microscopic inclusions or failed indentations, the indentations in the top and bottom positions were used, and their average was taken as the value for that location. The centre indentations at each location were evaluated in FIJI (ImageJ) software. Scale bars on the SEM photos were used to set the scale in the software for measuring purposes. The multi-point tool in FIJI (ImageJ) was used to select the indentation perimeter, after which a polygon was created from the selected points. The actual area could then be measured using the newly created polygon. Measuring the two diagonals followed, and the data was then used to calculate the surface residual stresses using Equation (6.1). The measuring process is depicted in Figure 6-3.

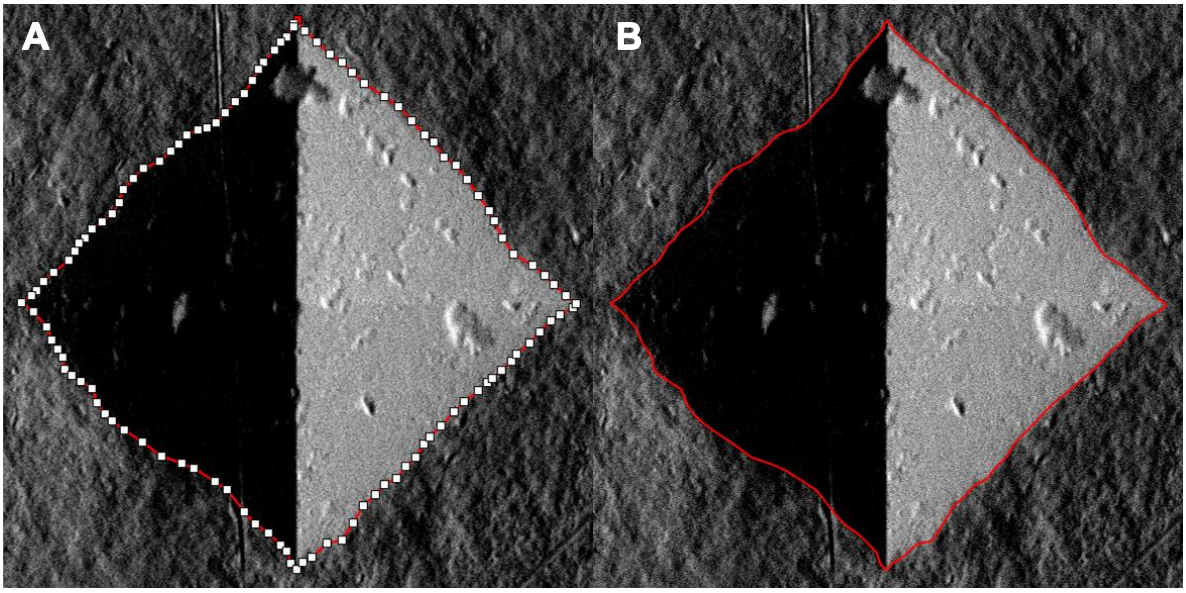

Figure 6-3: Stress-relieved cube with 0% hatch distance overlap, X face, bottom centre location, centre indentation measurement. Perimeter selection (A), polygon to be measured (B).

Figure 6-3 A depicts the selection of the indentation perimeter, and Figure 6-3 B shows the perimeter of the indentation that was measured. The measured data for the indentation shown in Figure 6-3 is presented in Table 6-1.

Table 6-1: Measured values of the stress-relieved cube with 0 % hatch distance overlap, X face, bottom centre location, centre indentation

Parameter	Value
L1 (vertical)	48.75µm
L2 (horizontal)	49.15µm
Actual area	1206.96µm^2
Nominal area	1198.05µm^2

The hardness values, actual and nominal areas and diagonal lengths of the indentations were evaluated using these photographs, and the data was input into Equations (6.1) and (6.2), which were derived in Chapter 3.

$$\sigma_{res} = \sigma_0 \times \left(\left[\frac{8 \times P}{3 \times \sigma_0 \times (L_1 + L_2)^2} \right]^{\frac{1}{n}} - 0.08 \right)^n \times \left\{ e^{\left[\frac{1 - \frac{8 \times A_{real}}{(L_1 + L_2)^2}}{0.32} \right]} - 1 \right\} \quad \textbf{(6.1)}$$

$$HV = \frac{0.1891 \times F}{L^2} \quad \textbf{(6.2)}$$

Using these formulae, the residual stress value obtained from the indentation in Figure 6-3 was -31.33 MPa, indicating compressive stress. The Vickers hardness value was calculated as 387 HV. Finally, using Equation (2.1), presented in Chapter 3, the Von Mises stress at this location was calculated.

$$\sigma_{res} = \left[\sigma_0 \times \left(\left[\frac{8 \times P}{3 \times \sigma_0 \times (L_1 + L_2)^2} \right]^{\frac{1}{n}} - 0.08 \right)^n \times \left\{ e^{\left[\frac{\frac{8 \times A_{real}}{(L_1 + L_2)^2} - 1}{0.32} \right]} - 1 \right\} \right] \quad \textbf{(6.3)}$$

Residual Von Mises stress calculated from the indentation in Figure 6-3 was 32.07 MPa. The magnitude of this value is close to the residual stress value since both are relatively small, and the difference between the Equations is not substantial. The only difference is that the sign has changed between the area ratios, and the absolute value is calculated.

6.1.2 Residual Stress Data Obtained from Vickers Micro-Indentations

Surface residual stresses calculated using the Vickers indentation method were predominantly compressive, as seen in literature [82]. Residual stress values were compared in 3x3 grids across each X and Y surface. Conditional formatting was used to highlight the differences in values and for visual comparison of trends noticed. Surface graphs of all cubes are included in APPENDIX B. Table 6-2 presents the surface residual stresses measured on the surfaces of the as-built specimens.

Table 6-2: Residual stresses calculated from Vickers indentations (as-built)

As-built cube surfaces							
Calculated surface residual stresses [MPa]							
Cube and face	**Values**			**Cube and face**	**Values**		
0A: X face	115	-60	154	**0A: Y face**	-37	-27	-60
	-149	-178	-19		83	-144	-13
	-228	-79	-99		-18	-70	40
0B: X face	-210	52	0	**0B: Y face**	-105	44	89
	112	-63	-144		-108	-23	-51
	-84	-17	-87		-107	-85	-116
5A: X face	-81	-16	-38	**5A: Y face**	-112	-258	-32
	-210	-75	-186		-155	5	-225
	-271	87	-284		-311	42	-97
5B: X face	9	-20	-247	**5B: Y face**	57	-109	-50
	-235	143	-169		-90	-34	-238
	-72	71	-1		24	-97	-317
10A: X face	63	-42	-35	**10A: Y face**	-1	-118	-123
	7	-189	-255		-108	9	-209
	-42	-102	68		-100	12	-130
10B: X face	-120	43	-142	**10B: Y face**	40	-250	-48
	-134	-133	-102		-145	11	-88
	-69	-38	18		-77	-13	-268

-400	-300	-200	-100	0	100	200

Colour Scale [MPa]

Conditional formatting was set so that compressive stresses (negative values) were increasingly blue with an increase in magnitude, zero values were set to white, and tensile stresses (positive values) were increasingly red with an increase in magnitude. Calculated values are seen to be predominantly compressive, with some tensile stresses present. There is, however, no discernible trends present. Cubes manufactured with the same hatch distance (0 %, 5 % and 10 % overlap) show very little correlation with each other. The X and Y faces of the same cubes also show minimal similarity with each other. For further evaluation, the average residual stress values across each surface were calculated and are shown in Table 6-3.

Table 6-3: Average residual stress calculated from Vickers indentations (as-built)

Average surface residual stresses [MPa]			
Cube and face	**Values**	**Cube and face**	**Values**
0A: X face	-60.4	**0A: Y face**	-27.2
0B: X face	-48.8	**0B: Y face**	-51.4
5A: X face	-119.2	**5A: Y face**	-126.9
5B: X face	-57.8	**5B: Y face**	-95.0
10A: X face	-58.5	**10A: Y face**	-85.5
10B: X face	-75.3	**10B: Y face**	-93.2
-200	-150	-100	-50	0
Colour Scale [MPa]				

Considering the average surface residual stress values in Table 6-3, it is observed that the X and Y faces of individual cubes differ considerably, from 5 % to 64 %. Average stress values of cubes with identical hatch distances do not correlate well, and no trend can be discerned with increasing hatch distance overlap. Cube 5A shows the highest compressive values, which seems like an outlier.

Stress-relieved cubes were evaluated in the same way as the as-built cubes. It was expected that these stresses would be much lower than those of the as-built cubes. Residual stress values calculated on the surfaces of the stress-relieved cubes are shown in Table 6-4.

Table 6-4: Residual stresses calculated from Vickers indentations (stress-relieved)

Stress-relieved cube surfaces							
Calculated surface residual stresses [MPa]							
Cube and face	**Values**			**Cube and face**	**Values**		
0C: X face	-211	-135	-330	**0C: Y face**	-43	-341	-230
	-165	-71	-176		-224	93	-200
	-41	-31	-127		-41	-241	-118
0D: X face	-234	-169	8	**0D: Y face**	-296	-322	-227
	-269	-173	-60		-208	-323	-253
	-293	-41	-97		-323	-310	-242
5C: X face	-23	-206	-248	**5C: Y face**	-296	-54	-393
	22	-297	-274		-242	-224	-215
	-35	-274	-332		-163	-148	-297
5D: X face	-499	-366	-344	**5D: Y face**	-258	-573	-265
	-243	-479	-349		-288	-321	-230
	-81	-79	-286		-171	-491	-386
10C: X face	-441	-349	-360	**10C: Y face**	-381	-588	-290
	-194	-341	-310		-264	-365	-298
	-302	-204	-360		-377	-322	-380
10D: X face	-171	-633	-276	**10D: Y face**	-255	-358	-438
	-359	-342	-323		-350	-416	-403
	-375	-395	-434		-332	-412	-310
-750	-600	-450	-300	-150	0	150	
Colour Scale [MPa]							

The stress-relieved cubes contain very high compressive surface residual stresses across all surfaces. The maximum and minimum residual stress values of the stress-relieved cubes were 93 MPa and -633 MPa, respectively. Stress distribution patterns do not provide clear trends and are not comparable, even across the X and Y faces of individual cubes. Average residual stress values in the stress-relieved condition are presented in Table 6-5.

Table 6-5: Average residual stress calculated from Vickers indentations (stress-relieved)

Average surface residual stresses [MPa]			
Cube and face	**Values**	**Cube and face**	**Values**
0C: X face	-143.1	**0C: Y face**	-149.4
0D: X face	-147.5	**0D: Y face**	-278.4
5C: X face	-185.1	**5C: Y face**	-225.9
5D: X face	-302.9	**5D: Y face**	-331.4
10C: X face	-317.8	**10C: Y face**	-362.7
10D: X face	-367.3	**10D: Y face**	-363.9
-400	-300	-200	-100
Colour Scale [MPa]			

A vague trend of increasing compressive residual stresses can be seen when comparing the average surface values. Apart from cube 0B, the average values of individual cube X and Y faces differ in a range from 1 % to 22 %, which is much less than those of the as-built cubes. Average residual stresses across the Y faces are frequently higher than those across the X faces of the same specimen. Residual stress magnitudes are much higher than expected on all cube surfaces.

Average stresses per cube were evaluated (taking the average stresses across the X and Y faces), and the stress reduction between the as-built and stress-relieved cubes were calculated. These stress reductions are shown in Table 6-6.

Table 6-6: Average stress reduction per cube

Average stress per cube			
Cube	**As-built [MPa]**	**Stress-relieved [MPa]**	**Reduction [%]**
0A: 0C	-43.8	-146.2	238
0B: 0D	-50.1	-212.9	324
5A: 5C	-123.1	-205.5	67
5B: 5D	-76.4	-317.1	315
10A: 10C	-72.0	-340.3	369
10B: 10D	-84.2	-365.6	334
0	-100	-200	-300
Colour Scale [MPa]			

Stress reduction values from the as-built condition to the stress-relieved condition are primarily above 200 %, with cube 5A being an outlier. Average reductions in stress values per hatch distance were calculated using the X and Y surface average stresses of both cubes per hatch distance, except for the 5 % hatch distance overlap cubes, where cube 5A was regarded as an outlier and not used. These values are displayed in Table 6-7.

Table 6-7: Average stress reduction per hatch distance

Average stress per hatch distance				
Cube	**As-built [MPa]**	**Stress-relieved [MPa]**		**Reduction [%]**
0 %	-47.0	-179.6		282
5 %	-76.4	-261.3		242
10 %	-78.1	-352.9		352
0	-100	-200	-300	-400
Colour Scale [MPa]				

Average stress reduction was very high (above 280 %) for all hatch distances. The highest reduction in stress was with the 10 % hatch distance overlap cubes. From these calculated values, stress relief was successful.

6.1.3 Von Mises Stress Data Obtained from Vickers Micro-Indentations

The Von Mises stresses were calculated at matching locations as the residual stresses using Equation (2.1). Von Mises stresses calculated on the as-built cubes are shown in Table 6-8.

Table 6-8: Von Mises stresses calculated from Vickers indentations (as-built)

As-built cube surfaces							
Calculated surface Von Mises stresses [MPa]							
Cube and face	Values			Cube and face	Values		
0A: X face	103	64	133	0A: Y face	38	27	63
	172	209	20		77	164	13
	282	85	109		18	75	39
0B: X face	257	50	0	0B: Y face	116	42	82
	102	67	164		119	23	54
	90	17	94		118	91	128
5A: X face	88	16	39	5A: Y face	125	326	33
	253	80	219		178	5	277
	350	81	371		418	41	105
5B: X face	9	20	316	5B: Y face	54	121	53
	295	126	199		98	35	299
	77	66	1		24	106	432
10A: X face	60	44	36	10A: Y face	1	132	138
	6	226	326		119	8	255
	44	111	64		109	12	146
10B: X face	133	42	162	10B: Y face	39	311	50
	150	151	112		165	11	95
	73	40	17		83	13	347
0	100	200	300	400	500		
Colour Scale [MPa]							

Similar to the calculated residual stress results, the Von Mises stresses do not show clear trends across the surfaces of the as-built cubes. Values differ considerably between the X and Y faces of individual cubes, and no trend or pattern can be discerned from these results. Average values were also calculated per face for further evaluation, and these values are shown in Table 6-9.

Table 6-9: Average Von Mises stresses calculated from Vickers indentations (as-built)

Average surface Von Mises stresses [MPa]			
Cube and face	**Values**	**Cube and face**	**Values**
0A: X face	130.8	**0A: Y face**	57.3
0B: X face	93.5	**0B: Y face**	86.0
5A: X face	166.3	**5A: Y face**	167.5
5B: X face	123.1	**5B: Y face**	135.7
10A: X face	101.8	**10A: Y face**	102.4
10B: X face	97.7	**10B: Y face**	123.6
0	50	100	150	200
Colour Scale [MPa]				

No clear trend is visible from the average values presented in Table 6-9. Average surface Von Mises stresses tend to be higher on the Y faces than on the corresponding X faces; however, this trend is not visible for cubes 0A and 0B. Von Mises stresses calculated on the stress-relieved cubes are included in Table 6-10.

Table 6-10: Von Mises stresses calculated from Vickers indentations (stress-relieved)

Stress-relieved cube surfaces							
Calculated surface Von Mises stresses [MPa]							
Cube and face	**Values**			**Cube and face**	**Values**		
0C: X face	250	149	427	**0C: Y face**	45	447	274
	187	89	201		268	87	233
	42	32	140		52	289	129
0D: X face	281	191	7	**0D: Y face**	374	417	273
	333	198	63		244	436	308
	369	42	105		419	400	293
5C: X face	23	242	302	**5C: Y face**	377	57	536
	22	378	349		293	266	253
	36	345	437		186	165	376
5D: X face	785	502	458	**5D: Y face**	317	967	328
	296	747	465		365	422	274
	86	85	362		197	746	533
10C: X face	671	467	494	**10C: Y face**	552	1037	379
	225	452	405		339	510	394
	396	240	497		545	435	547
10D: X face	202	1107	347	**10D: Y face**	314	483	649
	506	454	418		464	601	584
	526	558	645		435	606	399
0	200	400	600	800	1000	1200	
Colour Scale [MPa]							

Surface Von Mises stresses do not correlate across the X and Y faces of individual cubes. Stress values are much higher than those of the as-built cubes, which is unexpected. Further evaluation required the calculation of the average surface Von Mises stresses across each surface. These average values are shown in Table 6-11.

Table 6-11: Average Von Mises stresses calculated from Vickers indentations (stress-relieved)

Average surface Von Mises stresses [MPa]			
Cube and face	**Values**	**Cube and face**	**Values**
0C: X face	168.5	**0C: Y face**	202.6
0D: X face	176.6	**0D: Y face**	351.5
5C: X face	237.3	**5C: Y face**	278.6
5D: X face	420.5	**5D: Y face**	461.1
10C: X face	427.5	**10C: Y face**	526.5
10D: X face	529.2	**10D: Y face**	503.8
150	250	350	450	550
Colour Scale [MPa]				

Average Von Mises stresses seem to increase with increasing hatch distance. Values are also generally higher on the Y faces than on the corresponding X faces of each cube, except for cube 10B. The very high Von Mises stress on the Y face of cube 0B seems to be an outlier.

6.1.4 Hardness Data Obtained from Vickers Micro-Indentations

As a measure of validation, hardness values were also measured from the SEM photographs, using the lengths of the diagonals. Vickers hardness values for the as-built cubes are shown in Table 6-12.

Table 6-12: Vickers hardness values of as-built cubes

As-built cube surfaces								
Vickers hardness [HV]								
Cube and face	Values			Cube and face	Values			
0A: X face	293	314	286	0A: Y face	317	301	297	
	320	340	306		304	333	321	
	334	312	302		317	324	307	
0B: X face	329	310	306	0B: Y face	310	295	289	
	312	315	322		327	326	320	
	338	312	320		331	346	351	
5A: X face	317	342	337	5A: Y face	323	349	321	
	351	341	345		343	342	340	
	342	324	343		343	356	337	
5B: X face	309	293	325	5B: Y face	304	320	313	
	327	291	316		310	309	332	
	313	295	315		325	330	339	
10A: X face	304	308	303	10A: Y face	308	318	331	
	308	333	334		328	311	326	
	309	328	317		331	325	334	
10B: X face	346	339	333	10B: Y face	310	363	317	
	354	321	338		345	327	326	
	341	340	333		329	325	335	
Average hardness per cube surface [HV]								
0A: X face	311.9			0A: Y face	313.4			
0B: X face	318.1			0B: Y face	321.7			
5A: X face	338.2			5A: Y face	339.4			
5B: X face	309.4			5B: Y face	320.1			
10A: X face	316.1			10A: Y face	323.5			
10B: X face	338.3			10B: Y face	330.8			
250	275	300	325	350	375	400	425	
Colour Scale [HV]								

Hardness values measured on the as-built cubes vary from 286 HV to 363 HV. Most of these cubes are, on average, harder on the Y face than on their X faces, except for cube 10B. No clear trends can be discerned with varying hatch distances. Vickers hardness values of the stress-relieved cubes are presented in Table 6-13.

Table 6-13: Vickers hardness values of stress-relieved cubes

Stress-relieved cube surfaces								
Vickers hardness [HV]								
Cube and face	Values			Cube and face	Values			
0C: X face	389	406	409	0C: Y face	389	406	405	
	397	405	409		389	387	404	
	396	387	394		395	407	398	
0D: X face	399	399	387	0D: Y face	403	402	385	
	394	388	391		403	377	399	
	402	385	387		402	394	398	
5C: X face	380	392	388	5C: Y face	390	387	419	
	376	394	363		399	400	410	
	388	374	390		385	392	405	
5D: X face	389	384	392	5D: Y face	392	399	387	
	383	378	396		386	381	399	
	373	369	389		369	409	396	
10C: X face	366	390	377	10C: Y face	349	385	351	
	389	393	374		338	365	345	
	364	385	373		346	350	352	
10D: X face	313	419	382	10D: Y face	390	393	382	
	356	393	401		402	385	369	
	370	383	375		398	366	398	
Average surface residual stresses [MPa]								
0C: X face	399.2			0C: Y face	397.9			
0D: X face	392.4			0D: Y face	395.9			
5C: X face	382.9			5C: Y face	398.6			
5D: X face	383.8			5D: Y face	390.9			
10C: X face	378.9			10C: Y face	353.5			
10D: X face	376.9			10D: Y face	386.9			
250	275	300	325	350	375	400	425	
Colour Scale [HV]								

Vickers hardness values range from 313 HV to 419 HV. Hardness generally remains constant across cube surfaces, with no clear trends showing in any direction. However, average values show a general trend of decreasing hardness with increasing hatch distance overlap.

6.2 X-Ray Diffraction Data

XRD measurements were taken on the centre locations on each face for a single cuboid specimen per condition-parameter set. The maximum and minimum values of each of these measurements are shown in Table 6-14

Table 6-14: Centre location XRD values

As-built cubes XRD						
Hatch overlap [%]	Max Stress [MPa]		Min stress [MPa]		Average [MPa]	
	X	Y	X	Y	X	Y
0	1080.00	1045.00	346.99	363.29	713.50	704.15
5	-771.80	-785.74	-866.60	-877.88	-819.20	-831.81
10	-691.48	-632.45	-839.71	-793.98	-765.60	-713.22
Stress-relieved cubes XRD						
Hatch overlap [%]	Max Stress [MPa]		Min stress [MPa]		Average [MPa]	
	X	Y	X	Y	X	Y
0	-549.64	-30.83	-665.21	-52.22	-607.425	-41.525
5	-40.81	-0.93	-92.19	-94.38	-66.5	-47.655
10	-787.22	-833.23	-845.36	-956.52	-816.29	-894.875

-900	-600	-300	0	300	600	900	1200

Colour Scale [MPa]

The as-built cube specimen with 0 % hatch distance overlap showed very high surface residual stresses in the centres of both faces, close to the material's ultimate tensile strength. X and Y faces corresponded well with each other. As-built cubes with 5 % and 10 % hatch distance overlaps showed very high compressive stresses on both their faces.

Stress-relieved cubes were expected to have very low stresses, which is displayed by both faces of the 5 % hatch distance overlap cube and the Y face of the 0 % hatch distance overlap cube. Comparison of the stresses in the as-built and stress-relieved conditions required two faces that were observed to be free of the compression effect. The Y faces of the 0 % overlap cubes satisfied this condition, and multiple points on each of these faces were evaluated using XRD. Nine locations on the Y face were chosen for this purpose, as shown in Figure 6-4.

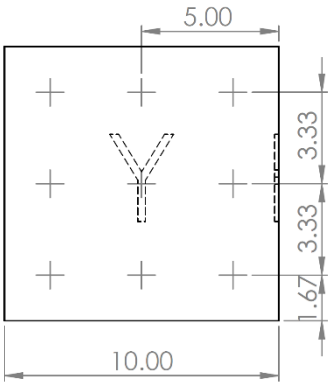

Figure 6-4: Locations for XRD evaluation

Locations were the same as chosen for the Vickers indentation tests. The XRD results obtained from these tests are shown in Table 6-15.

Table 6-15: XRD results of 0 % overlap cubes in the as-built and stress-relieved condition

Hatch overlap [%]	As-built Y face [MPa]			Stress-relieved Y face [MPa]		
0	1030.44	1013.66	963.37	-35.18	8.71	-28.04
	950.52	992.95	916.32	-37.54	-27.55	-37.02
	551.09	705.57	569.00	-19.93	-55.37	-48.41
Average	854.77			-31.15		

-100	100	300	500	700	900	1100
Colour Scale [MPa]						

Average residual stress values across the Y faces of the 0 % hatch distance overlap cubes show that the stress-relieving was successful. Residual stress values on the Y face of the as-built cube are highly tensile, and the values are close to the material's ultimate tensile strength. Values seem to decrease from the top locations of the face to the bottom. Values on the bottom locations of this face are much lower than the rest of the values. The values on the face of the stress-relieved cube are mostly compressive, and the highest stress magnitude is 55 MPa, which is virtually negligible. Slight differences are visible across the cube face, and a single tensile value is present at the centre top location, although this value is relatively small. The same trend is visible as with the as-built cube; stresses seem to decrease and become increasingly tensile from top to bottom. The low compressive stress at the bottom left location of the stress-relieved cube is the only exception to this trend.

6.3 Simulation Data

Since the data obtained from the Vickers indentation tests did not correlate well, simulations were done using the inherent strain method (with Simufact Additive) to evaluate the expected surface residual stresses in the cuboid specimens. Tangential stresses were simulated since these stresses act in the surfaces of the specimens; therefore, the tangential stresses are comparable to the stresses calculated from the Vickers indentation tests. In addition, the Von Mises residual stress data that was obtained using a similar equation were also simulated. Simulation data was firstly extracted from the simulation software as ".arc" files, extracted using the included Arc Tool software, and finally, input into MatLab for evaluation. Scatter plots were created using this data, and plots like those shown in Figure 6-5 are helpful for visual understanding of the distribution of the residual stresses on the surfaces of the cubes.

6.3.1 Orthotropic Calibration: As-Built Cube Data

Orthotropic as-built cubes were calibrated with two cantilevers as explained under 5.2.1. The tangential and Von Mises stresses are shown in Figure 6-5.

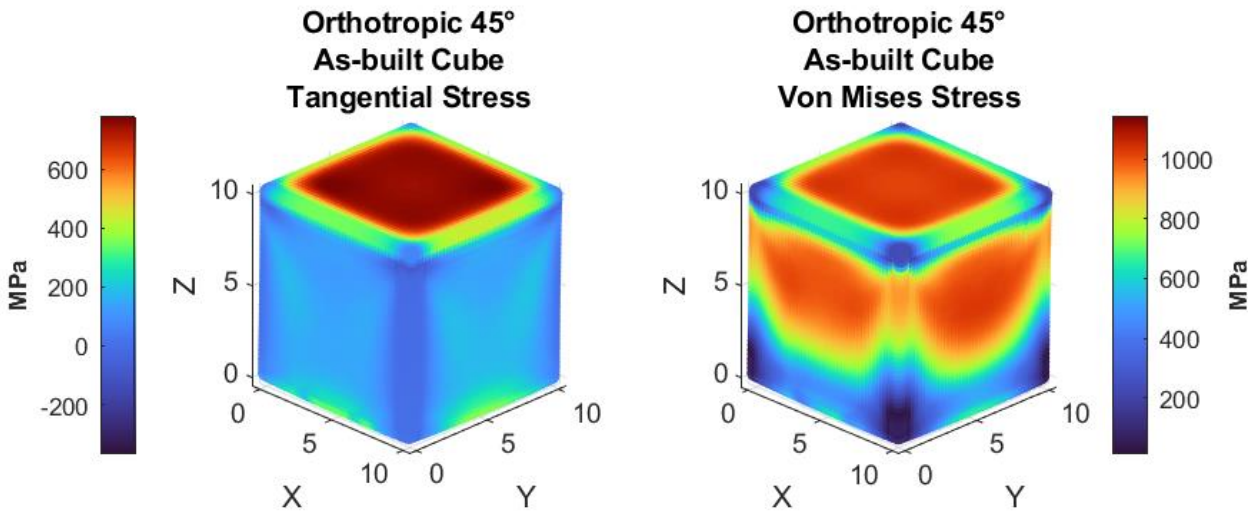

Figure 6-5: Tangential and Von Mises stresses on the orthotropic simulation, as-built cube surfaces

Stress distribution patterns of both the tangential and Von Mises stresses correlate across both faces, with slight differences between the Von Mises stresses on the X and Y faces. Tangential stresses do not vary much across the surfaces, whereas the Von Mises stresses increase from the bottom upwards, with the highest stresses present in the upper centre regions. Average surface tangential stress values for the orthotropic as-built cubes are 130 MPa for the X face and

152 MPa for the Y face. Average surface Von Mises stresses are 718 MPa for the X face and 733 MPa for the Y face.

6.3.2 Orthotropic Calibration: Stress-Relieved Cube Data

Orthotropic stress-relieved cubes were calibrated in the same manner as the as-built orthotropic cubes. In addition, stress-relief heat treatments were input into the simulation software, and the resulting stresses were then obtained. As expected, these stresses are much lower than those obtained from the as-built simulations. The tangential and Von Mises stresses on the X and Y faces are presented in Figure 6-6.

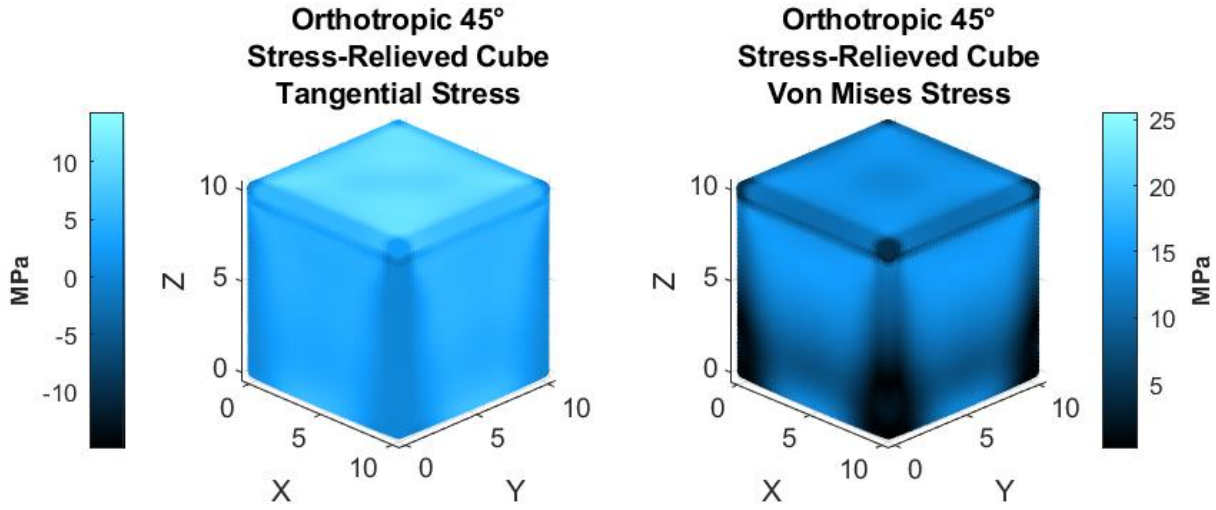

Figure 6-6: Tangential and Von Mises stresses on the orthotropic simulation, stress-relieved cube surfaces

Tangential and Von Mises stresses on the surfaces of the stress-relieved orthotropic cubes are very low and follow the same stress distribution patterns as those of the as-built cubes. Furthermore, minuscule deviations in the stress distribution patterns across the bottoms of the Von Mises stresses are present, where the stresses increase relative to the rest of the cube surfaces. Average surface tangential stress values for the orthotropic as-built cubes are 3 MPa for the X face and 4 MPa for the Y face, and average surface Von Mises stresses are 10 MPa for both faces. These amount to stress reductions of ~98 % for the Von Mises stresses and ~97 %, indicating that the stress-relief simulations were successful.

6.3.3 Mechanical Calibration: As-Built Cube Data

Mechanical cubes were calibrated using a single cantilever with 45° rotation between its layers, as described in 5.2.2. Tangential and Von Mises stress distributions on the X and Y faces are presented in Figure 6-7.

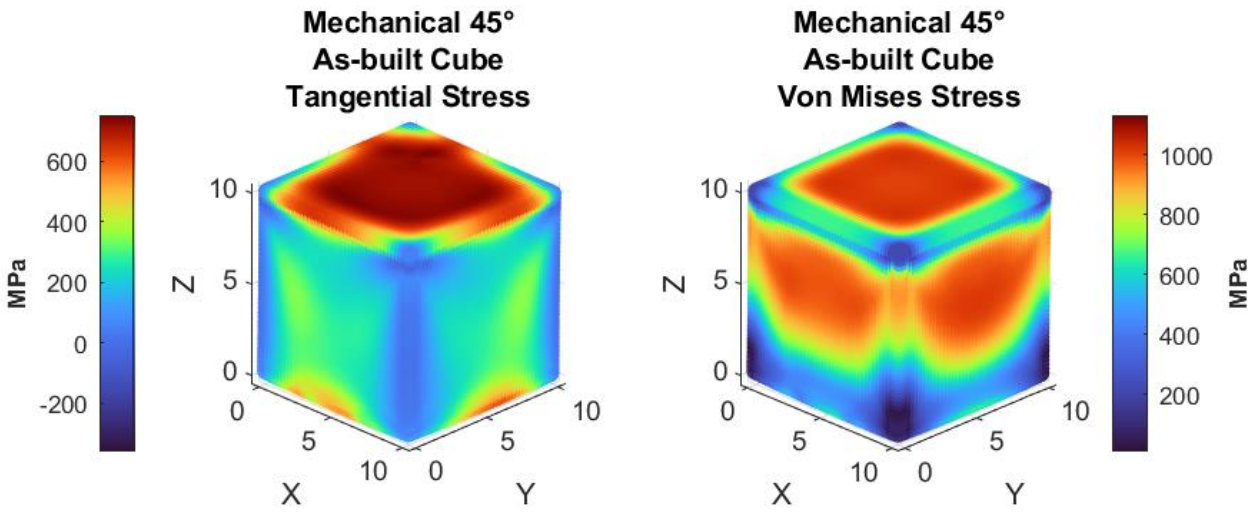

Figure 6-7: Tangential and Von Mises stresses on the mechanical simulation, as-built cube surfaces

Tangential stress distributions differ somewhat from those on the orthotropic as-built cube surfaces. Slight increases in stress values are present on the left side of the X face, and on the right side of the Y face. Von Mises stress distributions of the mechanical as-built cubes are practically identical to those of the orthotropic as-built cubes. Average surface tangential stresses are 239 MPa for the X face and 232 MPa for the Y face, and average surface Von Mises stresses for the mechanical as-built cubes are 726 MPa for the X face and 720 MPa for the Y face. Average tangential stresses differ from the orthotropic cubes by about 46 % and 35 % for X and Y faces, respectively, whereas average Von Mises stresses are within 2 %.

6.3.4 Mechanical Calibration: Stress-Relieved Cube Data

Stress-relieving simulations were done in the same way as the orthotropic stress-relieved cube. Tangential and Von Mises stresses of the stress-relieved mechanical cubes are shown in Figure 6-8.

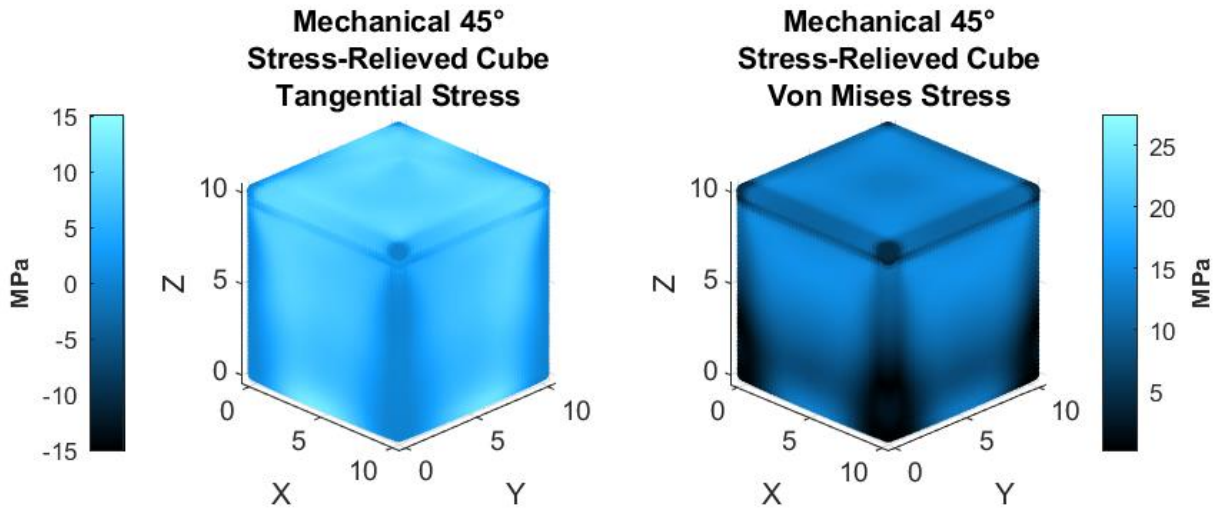

Figure 6-8: Tangential and Von Mises stresses on the mechanical simulation, stress-relieved cube surfaces

Surface tangential stresses and Von Mises stresses follow the same distribution patterns as those of the as-built mechanical cubes, with lower stress values. The same phenomenon is seen with the orthotropic cubes, where the Von Mises stress distributions of the stress-relieved cubes differ at the bottom of the cubes. Since the tangential stresses of the mechanical as-built cubes were much higher than those of the orthotropic cubes, the high tangential stress values present in the stress-relieved mechanical cubes are expected. Average surface tangential stresses are 6 MPa, and average surface Von Mises stresses are 10 MPa and 6 MPa, respectively, for the X and Y faces. Stresses correlate well between the X and Y faces, and the stress values are minor, indicating successful stress-relief simulation.

6.3.5 Thermo-Mechanical Calibration: As-Built Cube Data

Thermo-mechanical cubes were simulated using mechanical calibration methods, together with thermal calibration, as explained in 5.2.3. Tangential and Von Mises stress distributions across the surfaces of the thermo-mechanical cubes are shown in Figure 6-9.

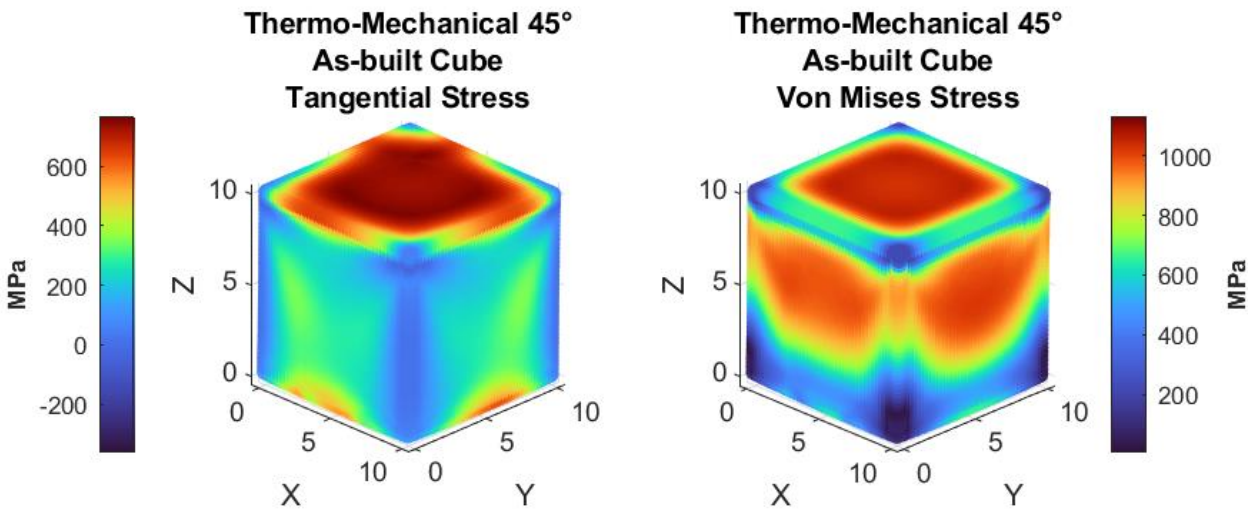

Figure 6-9: Tangential and Von Mises stresses on the thermo-mechanical simulation, as-built cube surfaces

Stress distributions for the tangential and Von Mises stresses are practically the same as those of the mechanical as-built cubes. Higher surface tangential stresses are visible at the centres of both the X and Y surfaces and Von Mises stresses are significant across both surfaces. Average surface tangential stresses are 239 MPa and 233 MPa, respectively, for the X and Y faces, and average surface Von Mises stresses are 705 MPa and 719 MPa, respectively, for the X and Y faces. These values are within 0.2 % of those of the mechanical as-built cubes.

6.3.6 Thermo-Mechanical Calibration: Stress-Relieved Cube Data

Thermo-mechanical cubes in the stress-relieved condition were calibrated and simulated in the same way as the thermo-mechanical as-built cubes, with the stress-relief stage simulated using a table inserted into the simulation program. Tangential and Von Mises stresses of the stress-relieved thermo-mechanical cubes are presented in Figure 6-10.

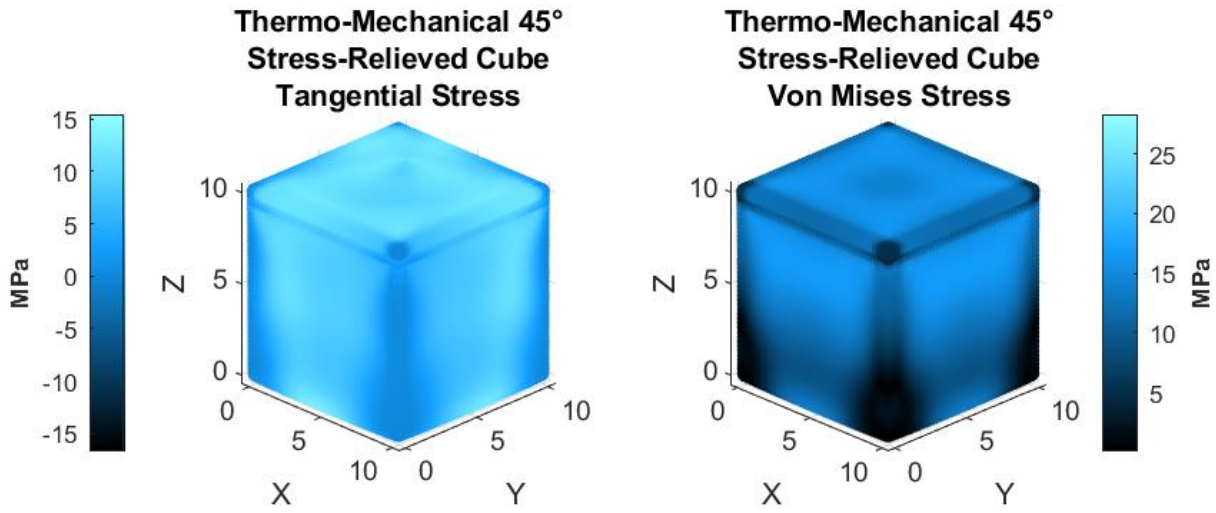

Figure 6-10: Tangential and Von Mises stresses on the thermo-mechanical simulation, stress-relieved cube surfaces

Surface tangential and Von Mises stresses correlate well with orthotropic and mechanical stress-relieved cubes in distribution and magnitude. Surface tangential stress distributions display similar distributions and magnitudes as those of the mechanical stress-relieved cubes, and the distributions are similar to the as-built cases, with decreased values. Average surface tangential stresses are 7 MPa for both the X and Y faces and average surface Von Mises stresses are 11 MPa for both the X and Y faces. These values are within 5 MPa of those of the mechanical as-built cubes.

6.4 Simulation Data: Specific Surface Values

Multiple simulations were run to better understand the expected residual stress values across the surfaces of the as-built and the stress-relieved cube specimens. These stresses will be compared between the different simulation types and between the simulated values and the calculated residual stress values obtained from the Vickers indentation method. Residual tangential stresses across the surfaces of the simulated specimens are included in Table 6-16.

Table 6-16: Simulated residual tangential stresses in the as-built condition

As-built cube surfaces						
Simulated tangential surface stresses [MPa]						
Cube and face	Values			Cube and face	Values		
Orthotropic X Tangential	117	135	95	Orthotropic Y Tangential	109	148	125
	168	142	120		152	169	184
	139	166	118		143	204	150
Mechanical X Tangential	210	236	149	Mechanical Y Tangential	136	225	210
	302	275	230		203	269	310
	257	319	194		165	322	263
Thermo-Mechanical X Tangential	210	231	145	Thermo-Mechanical Y Tangential	136	221	211
	301	275	207		203	269	309
	256	322	175		165	326	263
Average simulated tangential surface stresses							
Orthotropic X Tangential	133			Orthotropic Y Tangential	154		
Mechanical X Tangential	241			Mechanical Y Tangential	234		
Thermo-Mechanical X Tangential	236			Thermo-Mechanical Y Tangential	234		
50	100	150	200	250	300	350	
Colour Scale [MPa]							

Considering the respective X and Y faces, it is observed that the stress distributions are mirrors of each other. Average values differ between X and Y faces of the same simulation type. Differences are 16 % for the orthotropic simulation, 3 % for the mechanical simulation and 41 % for the thermo-mechanical simulation. Tangential stresses of the stress-relieved simulated cubes are shown in Table 6-17.

Table 6-17: Simulated residual tangential stresses in the stress-relieved condition

Stress-relieved cube surfaces								
Simulated tangential surface stresses [MPa]								
Cube and face	Values			Cube and face	Values			
Orthotropic X Tangential	5	4	4	Orthotropic Y Tangential	5	5	5	
	4	4	3		4	5	4	
	3	4	2		3	4	3	
Mechanical X Tangential	9	8	7	Mechanical Y Tangential	6	8	10	
	7	8	5		5	8	8	
	4	8	3		3	7	5	
Thermo-Mechanical X Tangential	10	9	7	Thermo-Mechanical Y Tangential	7	8	11	
	9	9	6		6	9	9	
	4	8	3		3	8	5	
Average simulated tangential surface stresses								
Orthotropic X Tangential	4			Orthotropic Y Tangential	4			
Mechanical X Tangential	7			Mechanical Y Tangential	6			
Thermo-Mechanical X Tangential	7			Thermo-Mechanical Y Tangential	7			
0	2	4	6	8	10			
Colour Scale [MPa]								

The tangential stresses in the stress-relieved condition show an apparent reduction in magnitude, and the thermo-mechanical simulated cubes in this condition are predominantly compressive, in stark contrast to the entirely tensile nature of the other simulation types. The stresses on the individual X and Y faces are comparable in distribution and magnitude. The Von Mises stresses across the surfaces of the simulated cubes are shown in Table 6-18.

Table 6-18: Simulated Von Mises stresses in the as-built condition

As-built cube surfaces								
Simulated Von Mises surface stresses [MPa]								
Cube and face	Values			Cube and face	Values			
Orthotropic X Von Mises	899	973	905	Orthotropic Y Von Mises	900	974	898	
	899	958	894		896	1020	898	
	449	541	444		443	618	445	
Mechanical X Von Mises	878	954	882	Mechanical Y Von Mises	881	959	881	
	890	946	887		886	1005	886	
	444	530	443		437	604	437	
Thermo-Mechanical X Von Mises	876	953	873	Thermo-Mechanical Y Von Mises	879	958	879	
	889	947	856		884	1006	885	
	441	530	405		434	603	434	
Average simulated Von Mises surface stresses								
Orthotropic X Von Mises	774			Orthotropic Y Von Mises	788			
Mechanical X Von Mises	761			Mechanical Y Von Mises	775			
Thermo-Mechanical X Von Mises	752			Thermo-Mechanical Y Von Mises	774			
400	500	600	700	800	900	1000	1100	
Colour Scale [MPa]								

Simulated Von Mises stresses correlate well between the different simulation types and between the X and Y faces of the individual simulation types. Average Von Mises stresses are generally higher on the Y faces than on the X faces; however, the differences are relatively small. From the Von Mises stress Equation, all stress values are positive. The highest values are very close to the ultimate tensile strength of as-built IN718 SLM specimens (from 1040 MPa to about 1300 MPa), indicating that the as-built cubes are indeed highly stressed. Simulated Von Mises stresses on the surfaces of the stress-relieved cubes are presented in Table 6-19.

Table 6-19: Simulated Von Mises stresses in the stress-relieved condition

Stress-relieved cube surfaces							
Simulated Von Mises surface stresses [MPa]							
Cube and face	**Values**			**Cube and face**	**Values**		
Orthotropic X Von Mises	15	15	15	**Orthotropic Y Von Mises**	15	15	15
	11	13	11		11	13	11
	5	8	5		5	8	5
Mechanical X Von Mises	15	15	15	**Mechanical Y Von Mises**	15	15	15
	11	13	11		11	13	11
	5	8	5		5	8	5
Thermo-Mechanical X Von Mises	16	17	16	**Thermo-Mechanical Y Von Mises**	16	17	16
	13	14	12		13	14	13
	5	9	4		5	9	5
Average simulated Von Mises surface stresses							
Orthotropic X Von Mises	11			**Orthotropic Y Von Mises**	11		
Mechanical X Von Mises	11			**Mechanical Y Von Mises**	11		
Thermo-Mechanical X Von Mises	12			**Thermo-Mechanical Y Von Mises**	12		
0	4		8	12	16		
Colour Scale [MPa]							

Von Mises stresses on the surfaces of the mechanical and orthotropic cubes are the same, whereas the thermo-mechanical surface Von Mises stresses differ somewhat. All stresses correlate well with each other and across X and Y faces of each simulation type. Maximum Von Mises stresses have been reduced by more than 98 % for all simulation types.

CHAPTER 7 DISCUSSION

This chapter will compare results obtained from the Vickers indentation method to the results obtained from XRD techniques. Simulation data will also be compared to see if the inherent strain method could be used to obtain usable data.

7.1 Vickers Data vs X-Ray Diffraction Data

7.1.1 As-Built Cubes

According to the Vickers micro-indentation data obtained, the as-built cube surfaces contained, on average, compressive stresses across all surfaces. Average residual stresses ranged from -27 MPa to -127 MPa, which is unexpected. In a similar study by Balbaa et al. [9], surface residual stresses in the as-built condition were measured using XRD and found to be between 327 MPa and 497 MPa (tensile) for mainly the same process parameters as those used in the current study [9]. Residual stresses have been said to increase with build height; however, only some cube faces in the as-built condition obey this trend [9, 43, 56]. Other studies have found values ranging from 50 MPa to 800 MPa at specimen surfaces [44, 59, 102].

XRD values on the surfaces of the as-built cubes presented high tensile stresses on the 0 % hatch distance overlap specimen and highly compressive stresses on each of the faces of the 5 % and 10 % hatch distance overlap cubes. The highly tensile values on the 0 % hatch distance overlap cube are present across both the X and Y faces and correlate more with literature than in other cases [44, 59, 102]. Residual stress values calculated using the Vickers micro-indentation method and XRD at the centres of the as-built are included in Table 7-1.

Table 7-1: Comparison of centre location residual stresses of cubes in the as-built condition

Measuring technique	0 % hatch		5 % hatch		10 % hatch	
	X	Y	X	Y	X	Y
XRD	713.50	704.15	-819.20	-831.81	-765.60	-713.22
Vickers A	-177.93	-143.89	-74.60	4.83	-189.29	8.50
Vickers B	-63.39	-22.94	143.00	-33.76	-133.18	10.63

-900	-600	-300	0	300	600	900
Colour Scale [MPa]						

Comparing the residual stresses calculated on the centres of the faces, significant variations are apparent between all data points. In addition, stresses measured utilising Vickers micro-indentations are low in magnitude compared to the XRD values.

7.1.2 Stress-Relieved Cubes

Specimens in the stress-relieved condition show higher magnitudes of compressive stresses than those in the as-built condition. XRD results indicate incredibly high compressive stresses; however, the differences in results between the two methods used are substantial. Residual stress values calculated using the Vickers micro-indentation method and XRD at the centres of the stress-relieved cubes are included in Table 7-2.

Table 7-2: Comparison of centre location residual stresses of cubes in the stress-relieved condition

Measuring technique	0 % hatch		5 % hatch		10 % hatch	
	X	Y	X	Y	X	Y
XRD	-607.43	-41.53	-66.50	-47.66	-816.29	-894.88
Vickers C	-75.90	92.88	-297.21	-223.92	-340.77	-365.25
Vickers D	-173.00	-316.24	-478.70	-320.85	-341.68	-416.50

-1000	-800	-600	-400	-200	0	200

Colour Scale [MPa]

XRD results for the cube with 0 % hatch distance overlap showed highly compressive stresses on the X face and very low compressive stresses on the Y face, which is unexpected since the X and Y faces are generally supposed to exhibit approximately equal stress values [29, 103].

Cubes evaluated with the Vickers micro-indentation technique were polished longer, as well as sand-blasted, as discussed earlier (under 4.2.4), which meant that more material was removed from these specimens (at most 0.24 mm). According to literature, IN718 specimens exhibit higher tensile stresses from the outer perimeter inwards up to about 1 mm deep [59]. In the study by Ahmad et al. [59], the samples were manufactured with three perimeter passes. This phenomenon of increasing tensile stresses was not seen in the current study since the Vickers-evaluated cubes displayed lower residual stresses than those measured with XRD. XRD data on the surfaces of the as-built cubes either showed highly tensile stress values or highly compressive stresses. Alternatively, XRD values on the surfaces of the stress-relieved cubes showed minuscule stress values (under 100 MPa tensile or compressive) or highly compressive stresses. It was decided that the two cubes with 0 % hatch distance overlap would be tested across their Y faces since these faces exhibited what was believed to be stresses with no external stress-causing factors. These two faces were XRD evaluated at identical locations used for the Vickers micro-indentations tests, and the results are shown in Table 7-3.

Table 7-3: XRD values across the Y face of a single as-built and stress-relieved cube

Hatch overlap [%]	As-built Y face [MPa]			Stress-relieved Y face [MPa]		
0	1030.44	1013.66	963.37	-35.18	8.71	-28.04
	950.52	992.95	916.32	-37.54	-27.55	-37.02
	551.09	705.57	569.00	-19.93	-55.37	-48.41
Average	854.77			-31.15		

-100	100	300	500	700	900	1100
Colour Scale [MPa]						

When evaluating the values across these two faces, the first observation was that the residual stresses increased with build height, as seen in literature [9, 43, 56]. Average values indicated a reduction in residual stress of about 104 %, and the stress-relieved cube exhibited stresses close to zero (with the highest magnitude being 55.37 MPa). This reduction in values proved the success of the stress-relieving procedure. Low stresses at the bottoms of both cubes are probably caused by the grinding-off of the supports and removal from the build plate [7].

Since the residual stress data obtained from the Vickers indentation tests did not correlate well (with each other and with XRD values), a single indentation was used and measured twice to evaluate the effect of minor deviations on the resulting residual stress values. The measured indentation is shown in Figure 7-1.

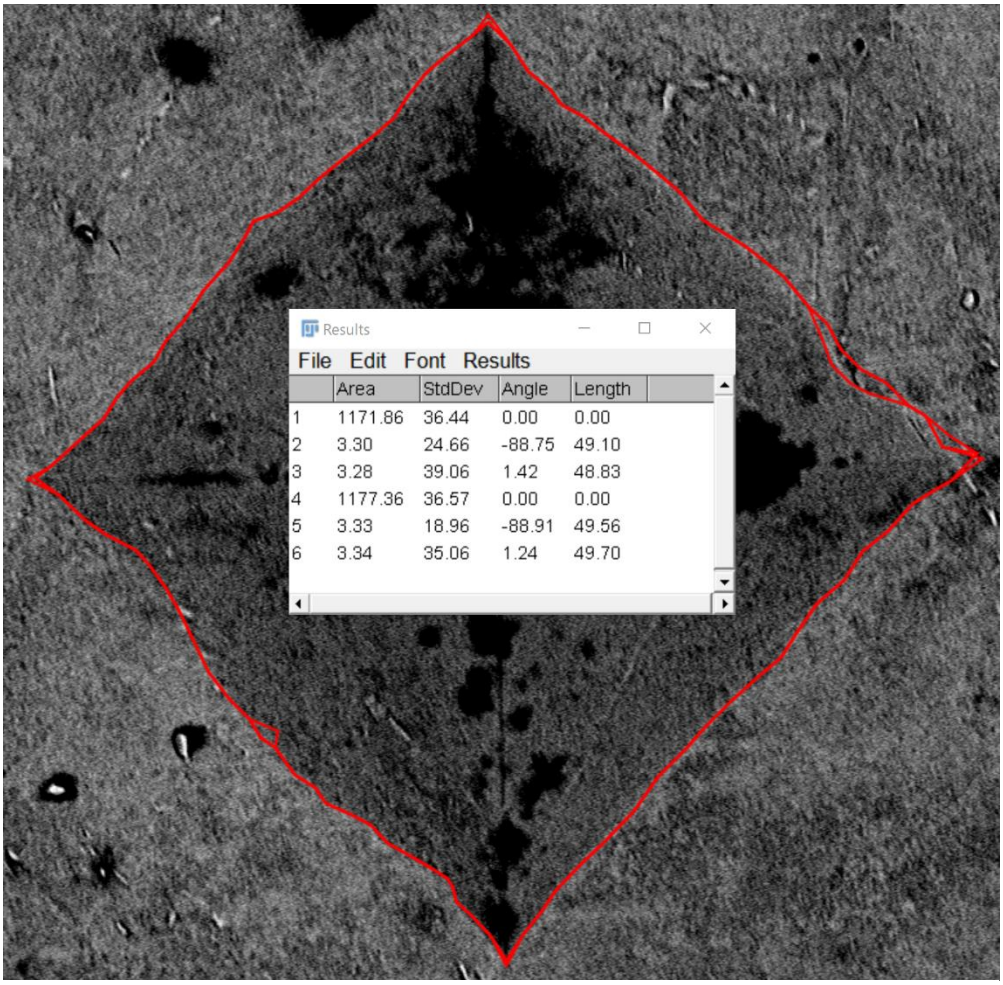

Figure 7-1: Human error in the measurement technique

The first set of values in Figure 7-1 (values 1 to 3) was measured from the inner perimeter, and the second set of values (4 to 6) was measured from the outer perimeter. A c^2 value of 0.978 was obtained from the inner perimeter and a c^2 value of 0.956 from the outer perimeter. The difference was a decrease of 2 %, and the resulting residual stress values were 99 MPa and 196 MPa for the inner and outer perimeters, respectively. This difference resulted in a 49 % increase, which is quite large, seeing as the c^2 value only differed by 2 %. This analysis shows the sensitivity of Equation (6.1) to changes in the area ratio.

7.2 Suspected Causes of Data Discrepancies

Removal of the specimens from the base plate may have caused some stress-relaxation and deformation of the specimens, causing misleading results [7, 30]. The sand-blasting process may have been severe enough to cause plastic deformation, and the measured stresses are not representational of the actual stresses built-up during the SLM process [104, 105]. Upon inspection, contours around the perimeter of the cubes were still intact after sand-blasting and polishing. It has been observed that specimens fabricated with a contour contain higher tensile

residual stresses (at and near the surface) than specimens fabricated without a contour, by around 250 MPa [103]. Since the dry electrochemical polishing delivered different results under the same conditions, some cubes were polished more than others. This difference in polishing times probably has little effect on the stresses present in the sample; however, the amount of material removed differed between each specimen and each face since some specimens needed to be polished for longer to obtain the required surface roughness for Vickers indentations. Specimen dimensions were measured before and after polishing, and the maximum amount of material removed was 0.24 mm. Considering the shallow penetration depth of XRD measurements (at most 0.01 mm), this may have caused the drastic discrepancies in the obtained values compared to the Vickers indented specimens. The macroscale unevenness (or waviness) as seen in Figure 7-2 may have led to untrustworthy Vickers indentations since the Vickers indenter needs to be as close to perpendicular as possible to the sample surface [101, 103].

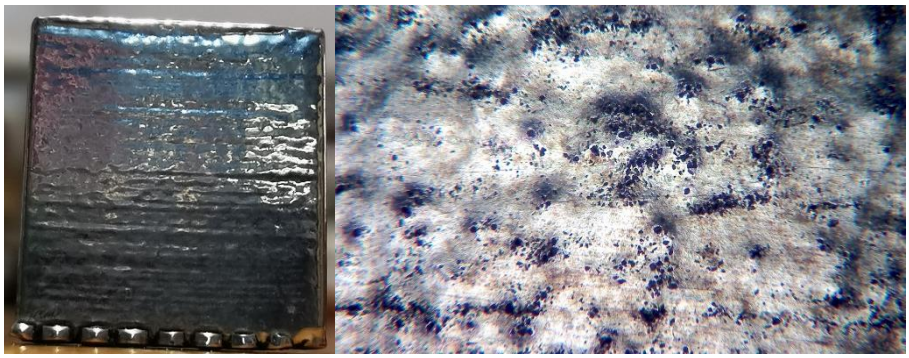

Figure 7-2: Surface unevenness/waviness of cuboid specimens

7.3 Hardness Results

The hardness values of the as-built specimens (ranging from 286 HV to 363 HV) correlated well with those found in the literature (~320 HV to about 400 HV), albeit somewhat lower [5, 35, 82, 106, 107]. Hardness values across the stress-relieved cube faces (ranging from 313 HV to 419 HV) are slightly lower than those found in the literature (~457 HV to about 500 HV) [5, 6, 35, 82]. These lower values are probably the result of using different heat treatment methods, such as solution annealing, which was not the case in the current study. Additionally, the contour with which the specimens were manufactured may have also affected the hardness values measured on the surfaces [6, 108, 109].

7.4 Simulated Data vs Vickers Micro-Indentation Data

Since surface results obtained from the Vickers micro-indentation method did not exhibit clear trends across the faces, average values of each face were compared to simulated surface

tangential stresses and Von Mises stresses. Average surface tangential stresses were graphed in comparison with the calculated residual stresses. The graph is shown in Figure 7-3.

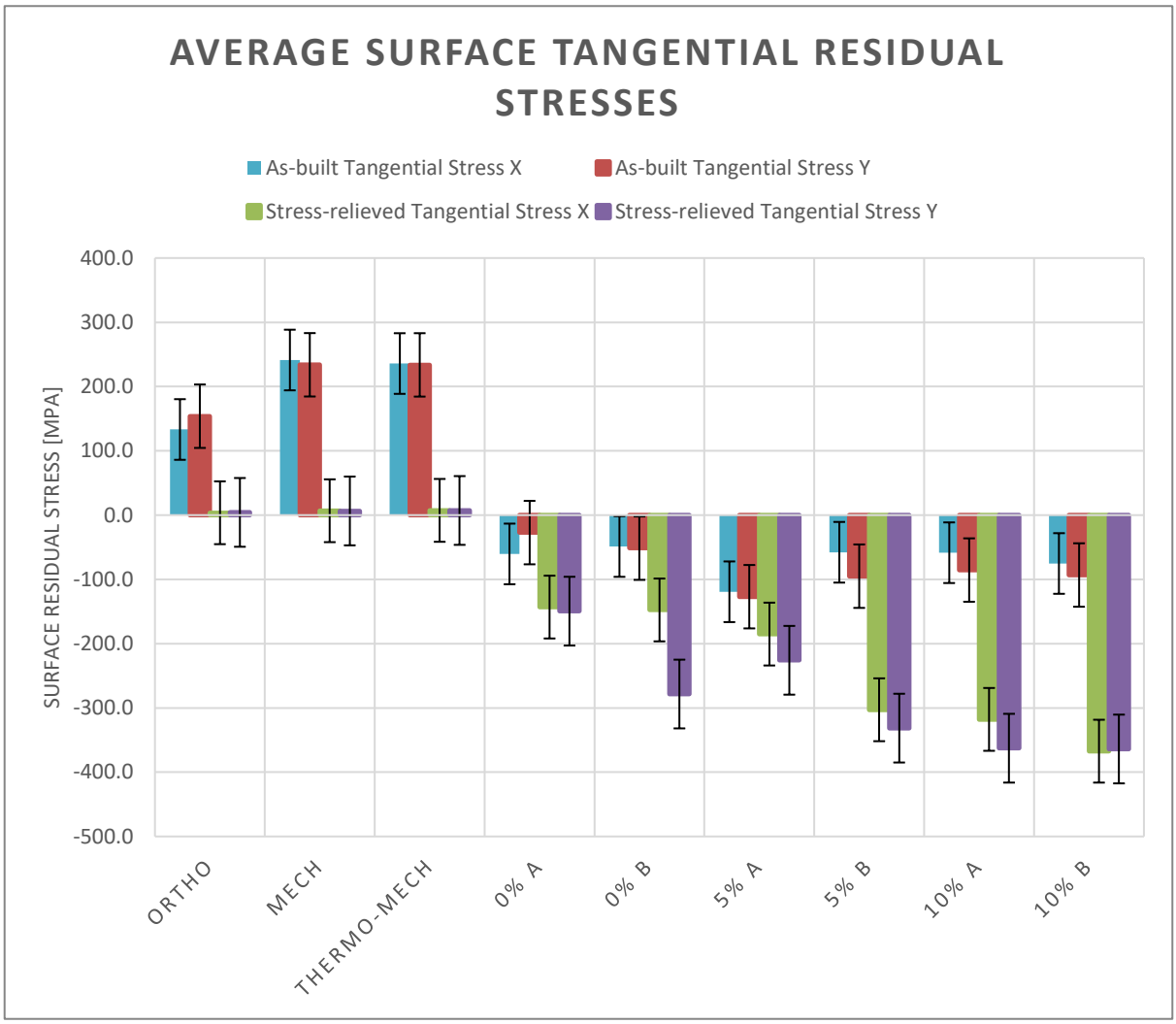

Figure 7-3: Average simulated surface tangential stresses vs calculated surface residual stresses

Average simulated surface tangential stresses in the as-built condition are tensile, and the different simulation types correlate well. Orthotropic simulated values in the as-built condition are slightly lower than those of the mechanical and thermo-mechanical values. Stress-relieved cube surfaces show very low tensile tangential stresses. Calculated surface residual stresses show no correlation with these stresses. Discrepancies between the measured and simulated data may arise from the failure of the simulation program to simulate the physical post-processes used in the experimental procedure, specifically, the sand-blasting process and the dry electrochemical polishing process. With the simulation program being unable to simulate the contours used to manufacture the specimens, the simulated values could not account for the stress differences

caused by these contours [99]. It has also been shown that residual stresses near the surfaces of specimens change considerably within 1 mm from the surface [59, 110]. Additionally, the inherent strain method has been shown to differ from experimental data by up to 17 % [111]. Values calculated using Equation (3.17) were compared to the simulated Von Mises stresses and are shown in Figure 7-4.

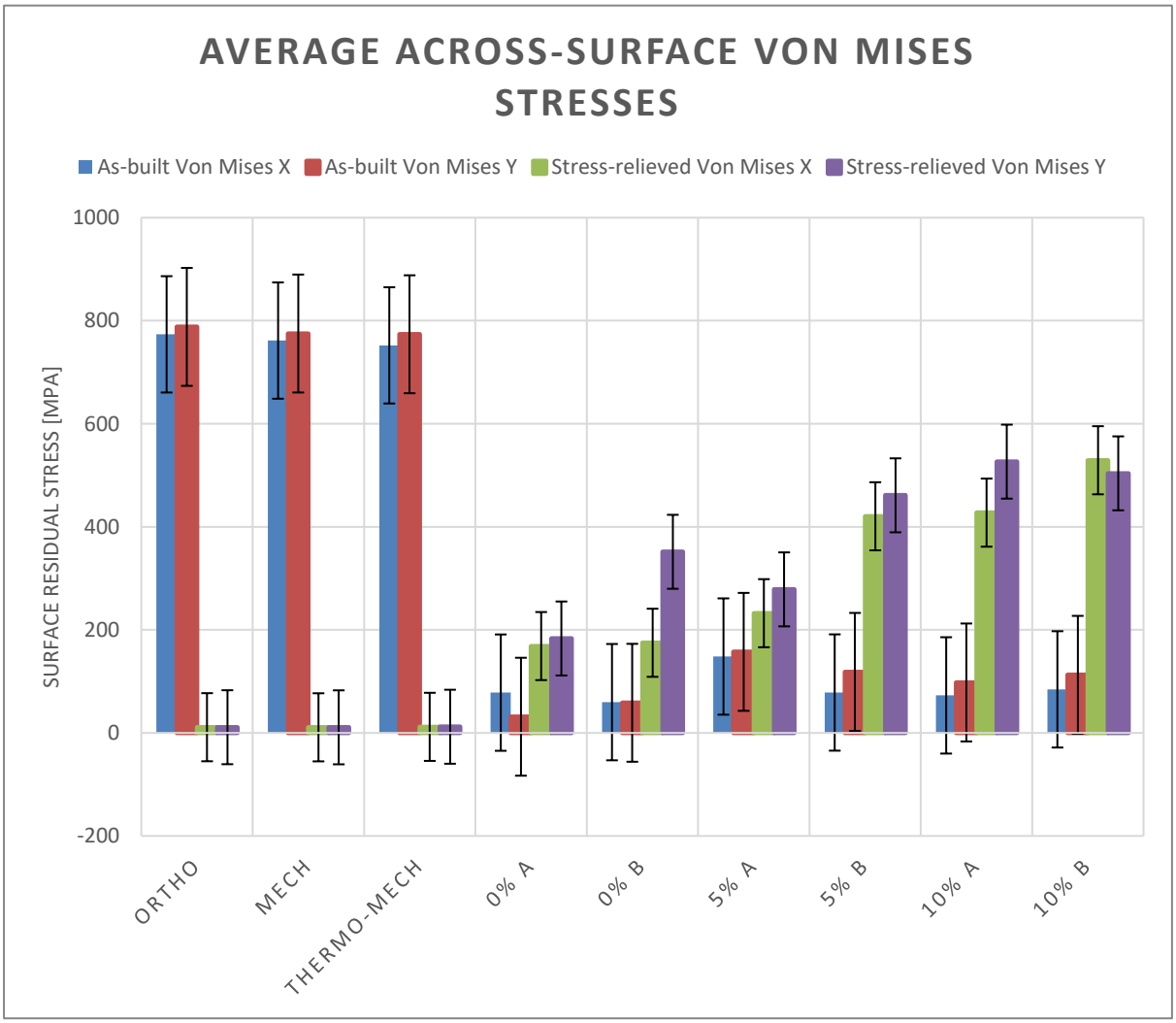

Figure 7-4: Average simulated Von Mises stresses vs calculated Von mises stresses

Average simulated Von Mises stresses in the as-built condition are highly tensile. After simulated stress-relief, Von Mises stresses reduce to low tensile values, nearing zero. Von Mises stresses calculated using Equation (3.17) do not exhibit these trends; on the contrary, these stresses appear to become increasingly tensile after stress relief. This dissimilarity between the calculated and simulated values confirm that this specific Equation cannot be used to calculate Von Mises stresses from Vickers indentation methods. Discrepancies in the above data may be due to the

same causes mentioned for the tangential stresses. In addition, the Equation used for calculating this data may introduce some errors not seen in previous studies [15, 83, 84].

CHAPTER 8 CONCLUSIONS AND RECOMMENDATIONS

8.1 Conclusions

The main objective of the current study was to evaluate the efficacy of the Vickers micro-indentation method to evaluate surface residual stresses of IN718 specimens manufactured with SLM. Several cuboid specimens were manufactured from IN718 powder, utilising the SLM process, and their surfaces were evaluated for surface residual stresses. Some of the specimens were kept in the as-built condition, and half were stress-relieved, after which all specimens were sand-blasted for short periods and dry electrochemically polished. Lateral surfaces of each cuboid specimen were indented with a Vickers micro indenter, and the residual stresses were calculated from the geometries of the indentations by applying Equation (3.16) (derived from [16]) and Equation (3.17) (from [15, 83, 84]). Specimens that were not evaluated using the Vickers micro-indentation method were evaluated using XRD methods. After it was seen that the values calculated from the Vickers indentations did not correlate between the lateral faces of individual cubes, lateral faces of cubes manufactured with the same processing parameters and measured XRD values, the inherent strain method was used (through simulation) to evaluate the surface residual stresses of cuboid specimens.

The study showed that the Vickers indentation method could not be used with certainty to calculate the residual stresses at the surfaces of SLM specimens. The main concern with this method is that the specimen surfaces need to be completely smooth and even to obtain trustworthy Vickers indentations, and with the observed irregularity across the surfaces of the specimens, this cannot be done without a substantial amount of post-processing. Post-process polishing may not influence the stresses present; however, the amount of material that needs to be removed from the specimen surfaces will cause measurements to provide data on the sub-surface regions of the specimens, thereby invalidating the data, specifically when the surface stresses need to be measured. Some human error in the measuring process of the Vickers indentations will, of course, also be present, and it was seen that minor deviations in the measuring technique led to significant variations in calculated residual stress values. It was also seen that the sand-blasting effect resulted in high compressive values on the surfaces of cuboid specimens since this method mimics the mechanisms of a shot-peening process, albeit less intense. Lower Vickers hardness values were observed and can be ascribed to the manufacturing of contours in the specimens, which were still present after dry electrochemical polishing. It was observed and substantiated by the literature that the presence of the contour during the manufacturing process may have led to discrepancies in the results [6, 108, 109].

Additionally, the inherent strain method (using Simufact Additive) could not account for the post-processes used in the study and could therefore not be used confidently to evaluate the surface residual stresses across the specimen faces. Simulated values could not account for the stress differences caused by contour scans during manufacturing [99]. It has also been shown that residual stresses near the surfaces of specimens change considerably within 1 mm from the surface [59, 110]. Additionally, the inherent strain method has been shown to differ from experimental data by up to 17 % [111].

8.2 Recommendations

Some recommendations are provided for future studies based on the work done in the current study. Recommendations include the following:

- Specimens of exact dimensions used in the study may be manufactured without the contour scans used during manufacturing. Evaluating these specimens may provide insight into the effects of the contour on the stresses measured.
- The effect of not including the sand-blasting post-process may be evaluated.
- Electrochemical polishing using liquid electrolytes may be used instead of dry electrochemical polishing to smooth the specimen surfaces.
- Mechanical polishing may be used to achieve adequate surface uniformity, and these surfaces should then be evaluated using the Vickers indentation method with XRD.
- The correlation between density and residual stresses may also be evaluated in future studies.
- The effect of inert gas flow direction may be studied to determine whether this could cause differences in measured surface residual stresses between perpendicular specimen faces.

REFERENCES

[1] K. Amato *et al.*, "Microstructures and mechanical behavior of Inconel 718 fabricated by selective laser melting," *Acta Materialia,* vol. 60, no. 5, pp. 2229-2239, 2012.

[2] V. Popovich, E. Borisov, A. Popovich, V. S. Sufiiarov, D. Masaylo, and L. Alzina, "Functionally graded Inconel 718 processed by additive manufacturing: Crystallographic texture, anisotropy of microstructure and mechanical properties," *Materials & Design,* vol. 114, pp. 441-449, 2017.

[3] W. J. Sames, F. A. List, S. Pannala, R. R. Dehoff, and S. S. Babu, "The metallurgy and processing science of metal additive manufacturing," *International Materials Reviews,* vol. 61, no. 5, pp. 315–360, 2016, doi: 10.1080/09506608.2015.1116649.

[4] E. Hosseini and V. Popovich, "A review of mechanical properties of additively manufactured Inconel 718," *Additive Manufacturing,* vol. 30, p. 100877, 2019.

[5] S. Holland, "Relating processing-microstructure-mechanical properties of inconel 718 fabricated by selective laser melting," University of Alabama Libraries, 2018.

[6] S. Moorthy, "Modeling and Characterization of Mechanical Properties in Laser Powder Bed Fusion Additive Manufactured Inconel 718," Colorado School of Mines, 2018.

[7] D. Deng, *Additively Manufactured Inconel 718: Microstructures and Mechanical Properties*. Linköping University Electronic Press, 2018.

[8] T. DebRoy *et al.*, "Additive manufacturing of metallic components – Process, structure and properties," *Progress in Materials Science,* vol. 92, pp. 112–224, 2018, Art no. Pii: S0079642517301172, doi: 10.1016/j.pmatsci.2017.10.001.

[9] M. Balbaa, S. Mekhiel, M. Elbestawi, and J. McIsaac, "On selective laser melting of Inconel 718: Densification, surface roughness, and residual stresses," *Materials & Design,* p. 108818, 2020.

[10] A. A. A. El Gaaly, "Optimization Models for Melting Patterns in Powder Bed Fusion Additive Manufacturing," 2019.

[11] N. Perevoshchikova *et al.*, "Optimisation of selective laser melting parameters for the Ni-based superalloy IN-738 LC using Doehlert's design," *Rapid Prototyping Journal,* vol. 23, no. 5, pp. 881–892, 2017, doi: 10.1108/rpj-04-2016-0063.

[12] S. Cordner, "Evaluation of porosity in additively manufactured inconel 718 through density and metallography," M.S.E., The University of Alabama in Huntsville, Ann Arbor, 10250756, 2016.

[13] J. L. Bartlett and X. Li, "An overview of residual stresses in metal powder bed fusion," *Additive Manufacturing,* vol. 27, pp. 131-149, 2019.

[14] L. Mugwagwa, I. Yadroitsev, and S. Matope, "Effect of Process Parameters on Residual Stresses, Distortions, and Porosity in Selective Laser Melting of Maraging Steel 300," *Metals,* vol. 9, no. 10, p. 1042, 2019.

[15] F. Liu, X. Lin, G. Yang, M. Song, J. Chen, and W. Huang, "Microstructure and residual stress of laser rapid formed Inconel 718 nickel-base superalloy," *Optics laser technology,* vol. 43, no. 1, pp. 208-213, 2011.

[16] S. Carlsson and P.-L. Larsson, "On the determination of residual stress and strain fields by sharp indentation testing.: Part I: theoretical and numerical analysis," *Acta materialia,* vol. 49, no. 12, pp. 2179-2191, 2001.

[17] S. Carlsson and P.-L. Larsson, "On the determination of residual stress and strain fields by sharp indentation testing.: Part II: experimental investigation," *Acta materialia,* vol. 49, no. 12, pp. 2193-2203, 2001.

[18] *ISO/ASTM 52900: 2015 Additive Manufacturing-General Principles-Terminology*, A. International, West Conshohocken, PA, 2015. [Online]. Available: www.astm.org

[19] I. Gibson, D. Rosen, and B. Stucker, *Additive Manufacturing Technologies*. New York, NY: Springer New York, 2015.

[20] G. A. Appuhamillage, N. Chartrain, V. Meenakshisundaram, K. D. Feller, C. B. Williams, and T. E. Long, "110th Anniversary: Vat Photopolymerization-Based Additive

Manufacturing: Current Trends and Future Directions in Materials Design," *Industrial Engineering Chemistry Research,* vol. 58, no. 33, pp. 15109-15118, 2019.
[21] W. Gao *et al.*, "The status, challenges, and future of additive manufacturing in engineering," *Computer-Aided Design,* vol. 69, pp. 65-89, 2015.
[22] A. Standard, "Standard terminology for additive manufacturing technologies," *ASTM International F2792-12a,* 2012.
[23] R. Engeli, T. Etter, S. Hövel, and K. Wegener, "Processability of different IN738LC powder batches by selective laser melting," *Journal of Materials Processing Technology,* vol. 229, pp. 484-491, 2016, doi: 10.1016/j.jmatprotec.2015.09.046.
[24] J. O. Milewski, *Additive Manufacturing of Metals: From Fundamental Technology to Rocket Nozzles, Medical Implants, and Custom Jewelry*. Springer, 2017.
[25] S. L. Campanelli, N. Contuzzi, A. Angelastro, and A. D. Ludovico, "Capabilities and performances of the selective laser melting process," *New Trends in Technologies: Devices, Computer, Communication and Industrial Systems,* vol. 1, no. 1, pp. 233-252, 2010.
[26] D. Herzog, V. Seyda, E. Wycisk, and C. Emmelmann, "Additive manufacturing of metals," *Acta Materialia,* vol. 117, pp. 371–392, 2016, Art no. Pii: S1359645416305158, doi: 10.1016/j.actamat.2016.07.019.
[27] *F3055-14a, Standard Specification for Additive Manufacturing Nickel Alloy (UNS N07718) with Powder Bed Fusion*, A. International, West Conshohocken, PA, 2014.
[28] R. J. Hebert, "Viewpoint: metallurgical aspects of powder bed metal additive manufacturing," *Journal of Materials Science,* vol. 51, no. 3, pp. 1165–1175, 2016, Art no. Pii: 9479, doi: 10.1007/s10853-015-9479-x.
[29] X. Wang, *Microstructural and mechanical characterizations of metallic parts made by powder-bed fusion additive manufacturing technologies*. The University of Alabama, 2017.
[30] T. Mishurova *et al.*, "The influence of the support structure on residual stress and distortion in SLM Inconel 718 parts," *Metallurgical Materials Transactions A,* vol. 49, no. 7, pp. 3038-3046, 2018.
[31] L. Rickenbacher, T. Etter, S. Hovel, and K. Wegener, "High temperature material properties of IN738LC processed by selective laser melting (SLM) technology," *Rapid Prototyping Journal,* 2013, doi: 10.1108/13552541311323281.
[32] W. E. Frazier, "Metal Additive Manufacturing: A Review," *Journal of Materials Engineering and Performance,* vol. 23, no. 6, pp. 1917–1928, 2014, Art no. Pii: 958, doi: 10.1007/s11665-014-0958-z.
[33] custompartnet.com. "Direct Metal Laser Sintering." http://www.custompartnet.com/wu/direct-metal-laser-sintering (accessed 2020).
[34] M. Zaeh, J. Moesl, J. Musiol, and F. Oefele, "Material processing with remote technology revolution or evolution?," *Physics Procedia,* vol. 5, pp. 19-33, 2010.
[35] E. Chlebus, K. Gruber, B. Kuźnicka, J. Kurzac, and T. Kurzynowski, "Effect of heat treatment on the microstructure and mechanical properties of Inconel 718 processed by selective laser melting," *Materials Science and Engineering: A,* vol. 639, pp. 647-655, 2015.
[36] H. Attar, M. Calin, L. Zhang, S. Scudino, and J. Eckert, "Manufacture by selective laser melting and mechanical behavior of commercially pure titanium," *Materials Science Engineering: A,* vol. 593, pp. 170-177, 2014.
[37] M. Cao *et al.*, "The effect of homogenization temperature on the microstructure and high temperature mechanical performance of SLM-fabricated IN718 alloy," *Materials Science Engineering: A,* vol. 801, p. 140427, 2021.
[38] P. K. Gokuldoss, S. Kolla, and J. Eckert, "Additive manufacturing processes: Selective laser melting, electron beam melting and binder jetting—Selection guidelines," *Materials & Design,* vol. 10, no. 6, p. 672, 2017.
[39] J. Elmer, J. Vaja, H. Carlton, and R. Pong, "The effect of Ar and N2 shielding gas on laser weld porosity in steel, stainless steels, and nickel," *Welding Journal,* vol. 94, no. 10, pp. 313S-325S, 2015.
[40] J. C. Fox, S. P. Moylan, and B. M. Lane, "Effect of Process Parameters on the Surface Roughness of Overhanging Structures in Laser Powder Bed Fusion Additive

Manufacturing," *Procedia CIRP,* vol. 45, pp. 131–134, 2016, Art no. Pii: S2212827116006429, doi: 10.1016/j.procir.2016.02.347.
[41] H. Schleifenbaum, W. Meiners, K. Wissenbach, and C. Hinke, "Individualized production by means of high power Selective Laser Melting," *CIRP Journal of manufacturing science and technology,* vol. 2, no. 3, pp. 161-169, 2010.
[42] J. P. Kruth, P. Mercelis, J. Van Vaerenbergh, L. Froyen, and M. Rombouts, "Binding mechanisms in selective laser sintering and selective laser melting," *Rapid prototyping journal,* 2005.
[43] Y. Liu, Y. Yang, and D. Wang, "A study on the residual stress during selective laser melting (SLM) of metallic powder," *The International Journal of Advanced Manufacturing Technology,* vol. 87, no. 1, pp. 647-656, 2016.
[44] R. Barros *et al.*, "Laser powder bed fusion of Inconel 718: Residual stress analysis before and after heat treatment," *Metals,* vol. 9, no. 12, p. 1290, 2019.
[45] Y. Lu *et al.*, "Study on the microstructure, mechanical property and residual stress of SLM Inconel-718 alloy manufactured by differing island scanning strategy," *Optics & Laser Technology,* vol. 75, pp. 197-206, 2015.
[46] M. Xia, D. Gu, G. Yu, D. Dai, H. Chen, and Q. Shi, "Influence of hatch spacing on heat and mass transfer, thermodynamics and laser processability during additive manufacturing of Inconel 718 alloy," *International Journal of Machine Tools and Manufacture,* vol. 109, pp. 147-157, 2016.
[47] G. E. Bean, D. B. Witkin, T. D. McLouth, D. N. Patel, and R. J. Zaldivar, "Effect of laser focus shift on surface quality and density of Inconel 718 parts produced via selective laser melting," *Additive Manufacturing,* vol. 22, pp. 207-215, 2018.
[48] K.-y. Feng, P. Liu, H.-x. Li, S.-y. Sun, S.-b. Xu, and J.-n. Li, "Microstructure and phase transformation on the surface of Inconel 718 alloys fabricated by SLM under 1050° C solid solution+ double ageing," *Vacuum,* vol. 145, pp. 112-115, 2017.
[49] N. Nadammal *et al.*, "Effect of hatch length on the development of microstructure, texture and residual stresses in selective laser melted superalloy Inconel 718," *Materials & Design,* vol. 134, pp. 139-150, 2017.
[50] D. Patil, "Effects of Increasing Layer Thickness in the Laser Powder Bed Fusion of Inconel 718," Arizona State University, 2019.
[51] M. Saunders, "X marks the spot-find ideal process parameters for your metal AM parts," *White papers collection–Renishaw plc,* 2017.
[52] P. Kumar, J. Farah, J. Akram, C. Teng, J. Ginn, and M. Misra, "Influence of laser processing parameters on porosity in Inconel 718 during additive manufacturing," *The International Journal of Advanced Manufacturing Technology,* vol. 103, no. 1-4, pp. 1497-1507, 2019.
[53] H. Pohl, A. Simchi, M. Issa, and H. C. Dias, "Thermal Stresses in Direct Metal Laser Sintering 366," in *2001 International Solid Freeform Fabrication Symposium*, 2001.
[54] K. Prashanth, S. Scudino, T. Maity, J. Das, and J. Eckert, "Is the energy density a reliable parameter for materials synthesis by selective laser melting?," *Materials Research Letters,* vol. 5, no. 6, pp. 386-390, 2017.
[55] F. Caiazzo, V. Alfieri, and G. Casalino, "On the Relevance of Volumetric Energy Density in the Investigation of Inconel 718 Laser Powder Bed Fusion," *Materials,* vol. 13, no. 3, p. 538, 2020.
[56] P. Mercelis and J. P. Kruth, "Residual stresses in selective laser sintering and selective laser melting," *Rapid Prototyping Journal,* vol. 12, no. 5, pp. 254–265, 2006, doi: 10.1108/13552540610707013.
[57] B. Cheng, S. Shrestha, and K. Chou, "Stress and deformation evaluations of scanning strategy effect in selective laser melting," *Additive Manufacturing,* vol. 12, pp. 240-251, 2016.
[58] C. Li, Z. Liu, X. Fang, and Y. Guo, "Residual stress in metal additive manufacturing," *Procedia Cirp,* vol. 71, pp. 348-353, 2018.
[59] B. Ahmad, S. O. van der Veen, M. E. Fitzpatrick, and H. Guo, "Residual stress evaluation in selective-laser-melting additively manufactured titanium (Ti-6Al-4V) and inconel 718

using the contour method and numerical simulation," *Additive Manufacturing,* vol. 22, pp. 571-582, 2018.
[60] P. J. Withers and H. K. D. H. Bhadeshia, "Residual stress. Part 1 – Measurement techniques," *Materials Science and Technology,* vol. 17, no. 4, pp. 355-365, 2001/04/01 2001, doi: 10.1179/026708301101509980.
[61] P. Withers, "Residual stress and its role in failure," *Reports on progress in physics,* vol. 70, no. 12, p. 2211, 2007.
[62] L. Mugwagwa, D. Dimitrov, S. Matope, and I. Yadroitsev, "Influence of process parameters on residual stress related distortions in selective laser melting," 2018.
[63] C. Chen *et al.*, "The effect of process parameters on the residual stress of selective laser melted Inconel 718 thin-walled part," *Rapid Prototyping Journal,* 2019.
[64] Y. Zhou *et al.*, "Selective laser melting of Ti–22Al–25Nb intermetallic: Significant effects of hatch distance on microstructural features and mechanical properties," *Journal of Materials Processing Technology,* vol. 276, p. 116398, 2020.
[65] T. Mukherjee, W. Zhang, and T. DebRoy, "An improved prediction of residual stresses and distortion in additive manufacturing," *Computational Materials Science,* vol. 126, pp. 360-372, 2017.
[66] H. Ali, H. Ghadbeigi, and K. Mumtaz, "Effect of scanning strategies on residual stress and mechanical properties of Selective Laser Melted Ti6Al4V," *Materials Science and Engineering: A,* vol. 712, pp. 175-187, 2018.
[67] J. Song *et al.*, "Understanding processing parameters affecting residual stress in selective laser melting of Inconel 718 through numerical modeling," *Journal of Materials Research,* vol. 34, no. 8, pp. 1395-1404, 2019.
[68] Z. Xiao *et al.*, "Study of residual stress in selective laser melting of Ti6Al4V," *Materials Design,* vol. 193, p. 108846, 2020.
[69] L. N. Carter, M. M. Attallah, and R. C. Reed, "Laser Powder Bed Fabrication of Nickel-Base Superalloys: Influence of Parameters; Characterisation, Quantification and Mitigation of Cracking," in *Superalloys 2012*, vol. 2009, E. S. Huron Ed. Hoboken, NJ: Wiley, 2012, pp. 577–586.
[70] S. Catchpole-Smith, N. Aboulkhair, L. Parry, C. Tuck, I. Ashcroft, and A. Clare, "Fractal scan strategies for selective laser melting of 'unweldable' nickel superalloys," *Additive Manufacturing,* vol. 15, pp. 113-122, 2017.
[71] J. Jhabvala, E. Boillat, T. Antignac, and R. Glardon, "On the effect of scanning strategies in the selective laser melting process," *Virtual and physical prototyping,* vol. 5, no. 2, pp. 99-109, 2010.
[72] P. Karimi, T. Raza, J. Andersson, and L.-E. Svensson, "Influence of laser exposure time and point distance on 75-µm-thick layer of selective laser melted Alloy 718," *The International Journal of Advanced Manufacturing Technology,* vol. 94, no. 5-8, pp. 2199-2207, 2018.
[73] T. Mishurova, K. Artzt, J. Haubrich, G. Requena, and G. Bruno, "New aspects about the search for the most relevant parameters optimizing SLM materials," *Additive Manufacturing,* vol. 25, pp. 325-334, 2019.
[74] S. Lou, X. Jiang, W. Sun, W. Zeng, L. Pagani, and P. Scott, "Characterisation methods for powder bed fusion processed surface topography," *Precision Engineering,* vol. 57, pp. 1-15, 2019.
[75] H. Wan, Z. Zhou, C. Li, G. Chen, and G. Zhang, "Effect of scanning strategy on grain structure and crystallographic texture of Inconel 718 processed by selective laser melting," *Journal of materials science & technology,* vol. 34, no. 10, pp. 1799-1804, 2018.
[76] J. Zhang, L. Gao, L. Cui, H. Wang, and J. Yang, "Analysis in the variation principle of thermal cycle and stress in the laser overlapping area," *Laser Technol,* vol. 4, pp. 370-372, 2005.
[77] M. Ferraro, "Quantitative determination of residual stress on additively manufactured Ti-6Al-4V," 2018.
[78] C. J. Hellier, *Handbook of nondestructive evaluation*. McGraw-Hill Education, 2013.
[79] "Destructive & Non-Destructive Testing: Definition, Function & Examples," ed. Study.com, 2018.

[80] J. L. Bartlett, B. P. Croom, J. Burdick, D. Henkel, and X. Li, "Revealing mechanisms of residual stress development in additive manufacturing via digital image correlation," *Additive Manufacturing,* vol. 22, pp. 1-12, 2018.
[81] K. M. Pawelec, A. A. White, and S. M. Best, "4 - Properties and characterization of bone repair materials," in *Bone Repair Biomaterials (Second Edition)*, K. M. Pawelec and J. A. Planell Eds.: Woodhead Publishing, 2019, pp. 65-102.
[82] X. Wang and Y. K. Chou, "A method to estimate residual stress in metal parts made by Selective Laser Melting," in *ASME International Mechanical Engineering Congress and Exposition*, 2015, vol. 57359: American Society of Mechanical Engineers, p. V02AT02A015.
[83] B. Song, S. Dong, Q. Liu, H. Liao, and C. Coddet, "Vacuum heat treatment of iron parts produced by selective laser melting: microstructure, residual stress and tensile behavior," *Materials & Design,* vol. 54, pp. 727-733, 2014.
[84] J. Cao, F. Liu, X. Lin, C. Huang, J. Chen, and W. Huang, "Effect of overlap rate on recrystallization behaviors of Laser Solid Formed Inconel 718 superalloy," *Optics Laser Technology,* vol. 45, pp. 228-235, 2013.
[85] Y. Cheng, Z. Xiao, H. Zhu, X. Zeng, and G. Wang, "Influence of substrate characteristics on residual stress of SLMed Inconel 718," *Rapid Prototyping Journal,* 2019.
[86] J.-P. Kruth, J. Deckers, E. Yasa, and R. Wauthlé, "Assessing and comparing influencing factors of residual stresses in selective laser melting using a novel analysis method," *Proceedings of the institution of mechanical engineers, Part B: Journal of Engineering Manufacture,* vol. 226, no. 6, pp. 980-991, 2012.
[87] R. Budynas and K. Nisbett, "Shigley's Mechanical Engineering Design," 10th ed: McGraw-Hill Education, 2014.
[88] K. Herrmann, *Hardness testing: principles and applications*. ASM international, 2011.
[89] D. Tabor, "A simple theory of static and dynamic hardness," *Proceedings of the Royal Society of London. Series A. Mathematical Physical Sciences,* vol. 192, no. 1029, pp. 247-274, 1948.
[90] H. Wang *et al.*, "Nanoindentation based properties of Inconel 718 at elevated temperatures: A comparison of conventional versus additively manufactured samples," *International Journal of Plasticity,* vol. 120, pp. 380-394, 2019.
[91] Y. Gao *et al.*, "Effect of δ phase on high temperature mechanical performances of Inconel 718 fabricated with SLM process," *Materials Science Engineering: A,* vol. 767, p. 138327, 2019.
[92] M. E. Fitzpatrick, A. T. Fry, P. Holdway, F. Kandil, J. Shackleton, and L. Suominen, "Determination of residual stresses by X-ray diffraction," 2005.
[93] C. Azersky, "Evaluation of Particle Size Dependent Crystal Defects in Inconel 718 by Line Profile Analysis of X-Ray Diffraction," Tufts University, 2020.
[94] M. Bugatti and Q. Semeraro, "Limitations of the inherent strain method in simulating powder bed fusion processes," *Additive Manufacturing,* vol. 23, pp. 329-346, 2018.
[95] X. Liang, L. Cheng, Q. Chen, Q. Yang, and A. C. To, "A modified method for estimating inherent strains from detailed process simulation for fast residual distortion prediction of single-walled structures fabricated by directed energy deposition," *Additive Manufacturing,* vol. 23, pp. 471-486, 2018.
[96] N. Ma *et al.*, "Inherent strain method for residual stress measurement and welding distortion prediction," in *ASME 2016 35th International Conference on Ocean, Offshore and Arctic Engineering*, 2016: American Society of Mechanical Engineers Digital Collection.
[97] X. Liang, Q. Chen, L. Cheng, D. Hayduke, and A. C. To, "Modified inherent strain method for efficient prediction of residual deformation in direct metal laser sintered components," *Computational Mechanics,* vol. 64, no. 6, pp. 1719-1733, 2019.
[98] K. Ravichandran, "Calibrating Inherent Strain for Additive Manufacturing: An investigation of different subscale geometries," 2020.
[99] Q. Chen *et al.*, "An inherent strain based multiscale modeling framework for simulating part-scale residual deformation for direct metal laser sintering," *Additive Manufacturing,* vol. 28, pp. 406-418, 2019.

[100] S. Liu, H. Li, C. Qin, R. Zong, and X. Fang, "The effect of energy density on texture and mechanical anisotropy in selective laser melted Inconel 718," *Materials Design,* vol. 191, p. 108642, 2020.
[101] A. Standard, "E384-17, Standard Test Method for Microindentation Hardness of Materials, ASTM International, West Conshohocken, PA, 2017," ed.
[102] D. Deng, R. L. Peng, H. Brodin, and J. Moverare, "Microstructure and mechanical properties of Inconel 718 produced by selective laser melting: Sample orientation dependence and effects of post heat treatments," *Materials Science Engineering: A,* vol. 713, pp. 294-306, 2018.
[103] T. Mishurova, K. Artzt, J. Haubrich, G. Requena, and G. Bruno, "Exploring the correlation between subsurface residual stresses and manufacturing parameters in laser powder bed fused Ti-6Al-4V," *Metals,* vol. 9, no. 2, p. 261, 2019.
[104] M. Torres and H. Voorwald, "An evaluation of shot peening, residual stress and stress relaxation on the fatigue life of AISI 4340 steel," *International Journal of Fatigue,* vol. 24, no. 8, pp. 877-886, 2002.
[105] D. Lesyk, S. Martinez, B. Mordyuk, V. Dzhemelinskyi, A. Lamikiz, and G. Prokopenko, "Post-processing of the Inconel 718 alloy parts fabricated by selective laser melting: Effects of mechanical surface treatments on surface topography, porosity, hardness and residual stress," *Surface Coatings Technology,* vol. 381, p. 125136, 2020.
[106] Q. Jia and D. Gu, "Selective laser melting additive manufacturing of Inconel 718 superalloy parts: Densification, microstructure and properties," *Journal of Alloys and Compounds,* vol. 585, pp. 713-721, 2014.
[107] J.-P. Choi *et al.*, "Densification and microstructural investigation of Inconel 718 parts fabricated by selective laser melting," *Powder Technology,* vol. 310, pp. 60-66, 2017.
[108] J. Yu, D. Kim, K. Ha, J. B. Jeon, and W. Lee, "Strong feature size dependence of tensile properties and its microstructural origin in selectively laser melted 316L stainless steel," *Materials Letters,* vol. 275, p. 128161, 2020.
[109] E. L. Stevens, J. Toman, A. C. To, and M. Chmielus, "Variation of hardness, microstructure, and Laves phase distribution in direct laser deposited alloy 718 cuboids," *Materials design,* vol. 119, pp. 188-198, 2017.
[110] C. Duan, X. Cao, and X. Luo, "Efficient Distortion Prediction of Laser Melting Deposited Industrial-scale Parts Using Modified Inherent Strain Method," in *IOP Conference Series: Earth and Environmental Science*, 2021, vol. 714, no. 3: IOP Publishing, p. 032032.
[111] M. R. Hill and D. V. Nelson, "The inherent strain method for residual stress determination and its application to a long welded joint," *ASME-PUBLICATIONS-PVP,* vol. 318, pp. 343-352, 1995.
[112] Z. Luo and Y. Zhao, "Efficient thermal finite element modeling of selective laser melting of Inconel 718," *Computational Mechanics,* vol. 65, no. 3, pp. 763-787, 2020.

APPENDIX A CALIBRATION PARAMETERS

Mechanical properties used during the calibration and simulation processes are shown in Table A-1.

Table A-1: Mechanical properties of IN718

Yield strength [MPa]	Ultimate tensile strength [MPa]	Elastic modulus [GPa]
758	1040	190

Build parameters used for calibration purposes are shown in Table A-2.

Table A-2: Build parameters used during calibration

Parameters of single laser		
Parameter	**Value**	**Unit**
Beam width	0.12	[mm]
Power	107	[W]
Scan speed	630	[mm/s]
Efficiency	50	[%]
Material	IN-718_powder	-

In addition to these parameters, voxel sizes of 0.25 mm were used for all calibration and simulation types. Material properties were taken as default from Simufact Material™. Thermal properties were used considering the differences with temperature increase, as shown in Table A-3 [112].

Table A-3: Thermal parameters for solid IN718

Temperature [K]	Thermal conductivity [W/mK]	Emissivity
298	8.9	0.54
373	10.8	0.53
473	12.9	0.53
573	15.2	0.53
673	17.4	0.53
773	18.7	0.54
873	20.8	0.54
973	21.9	0.54
1073	26.9	0.54
1173	25.8	0.54
1273	26.7	0.54
1373	28.3	0.54
1443	29.3	0.54
1609	444	0.33
1673	444	0.33
1773	444	0.34
1873	444	0.34

APPENDIX B SURFACE RESIDUAL STRESS RESULTS FROM VICKERS MICRO-INDENTATION TESTS: AS-BUILT CUBES

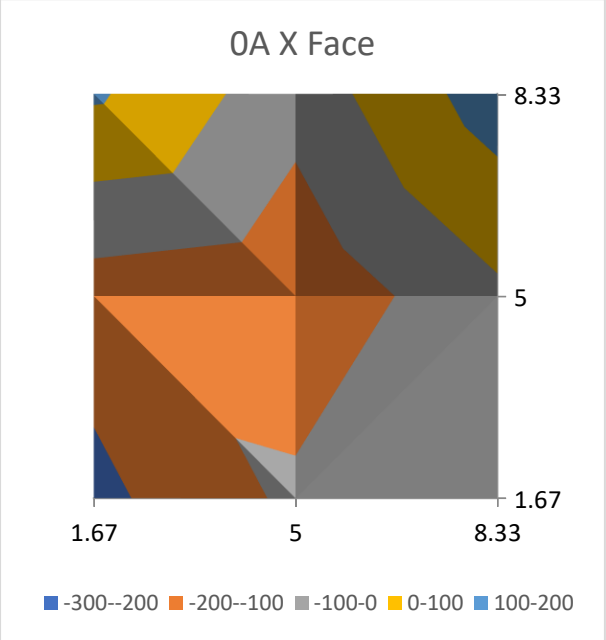

Figure B-1: Surface residual stresses of cube 0A [MPa]

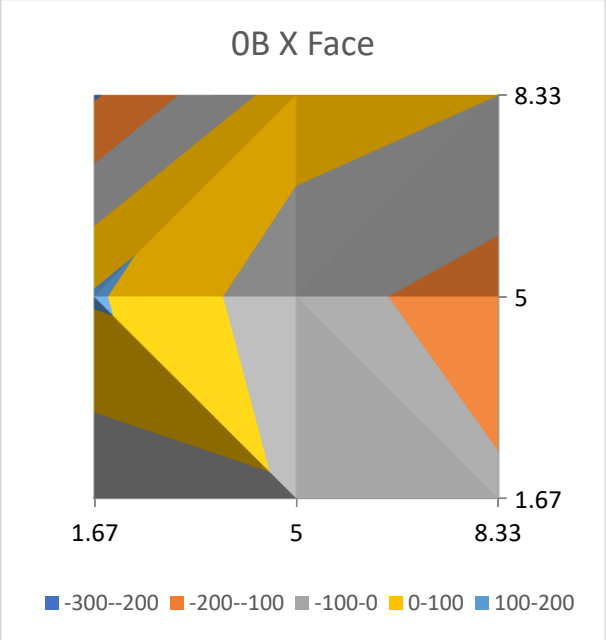

Figure B-2: Surface residual stresses of cube 0B [MPa]

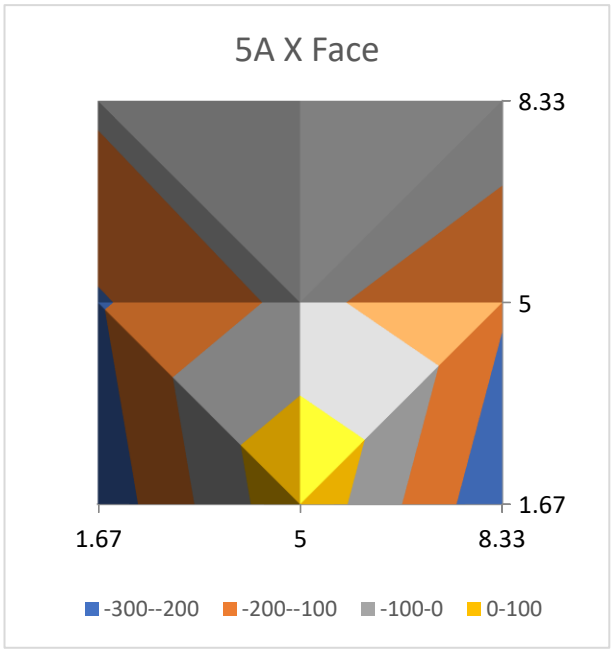

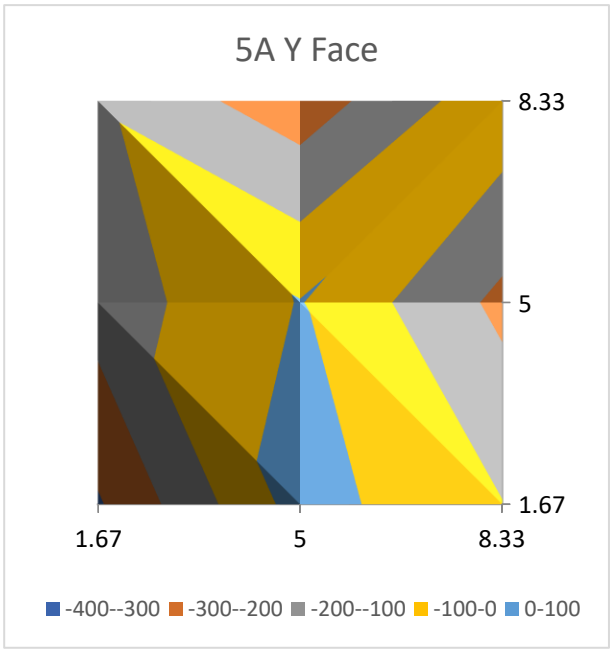

Figure B-3: Surface residual stresses of cube 5A [MPa]

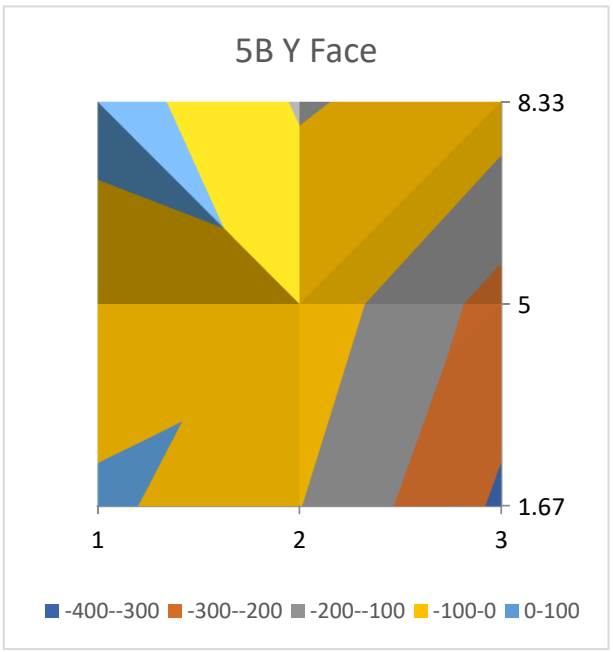

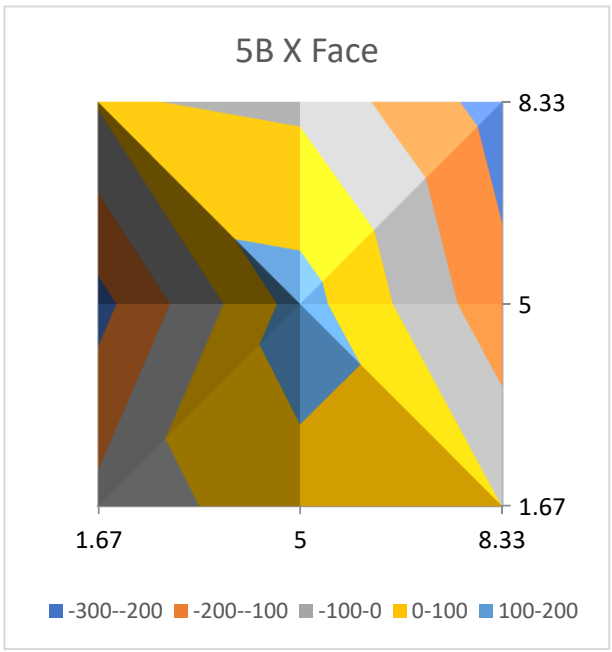

Figure B-4: Surface residual stresses of cube 5B [MPa]

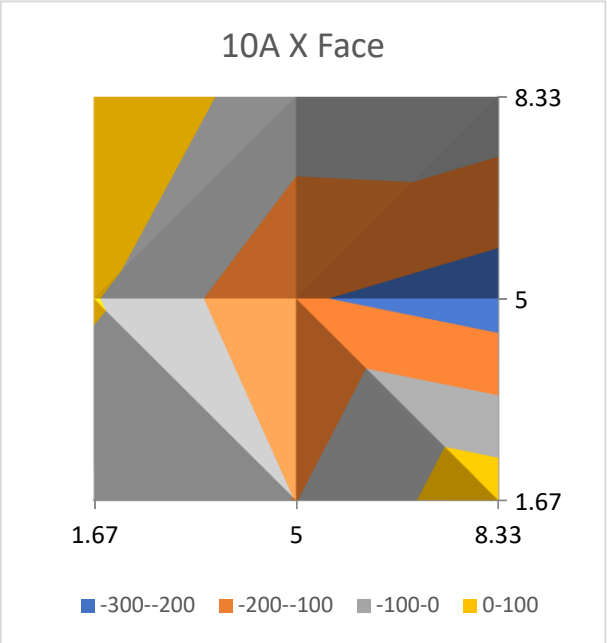

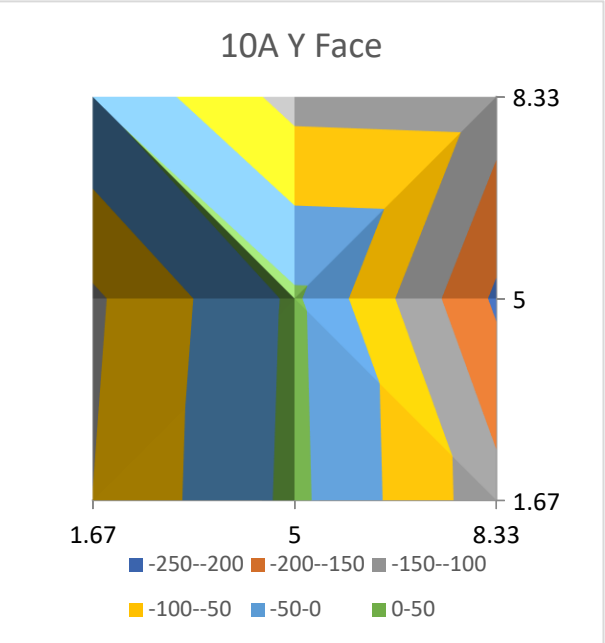

Figure B-5: Surface residual stresses of cube 10A [MPa]

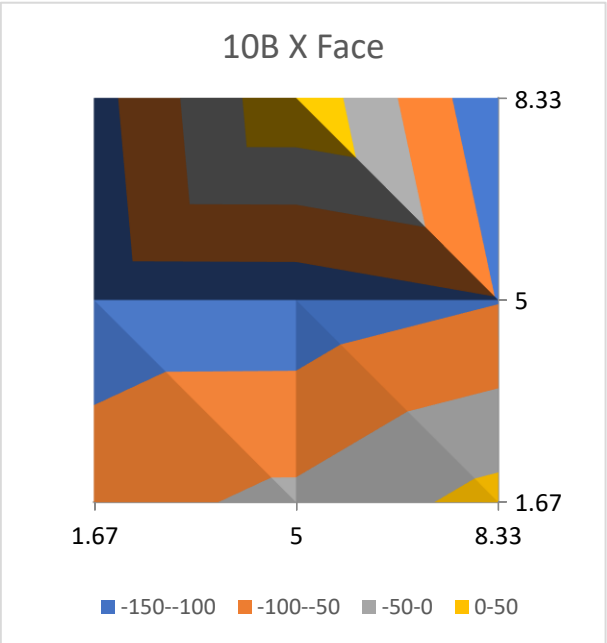

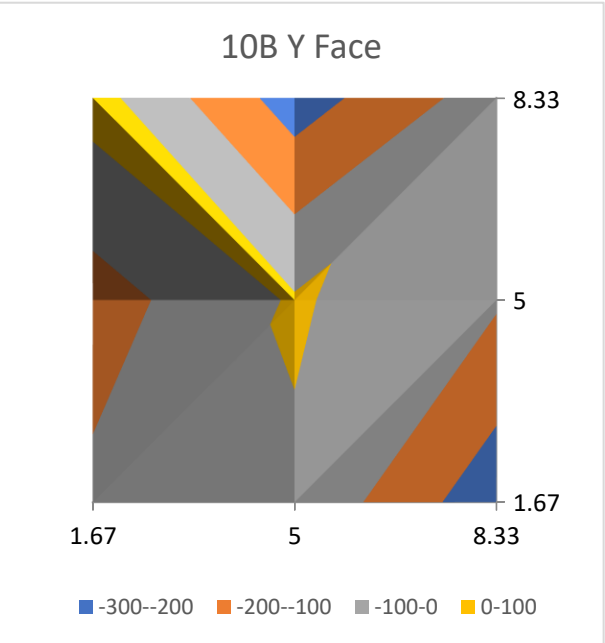

Figure B-6: Surface residual stresses of cube 10B [MPa]

APPENDIX C SURFACE RESIDUAL STRESS RESULTS FROM VICKERS MICRO-INDENTATION TESTS: STRESS-RELIEVED CUBES

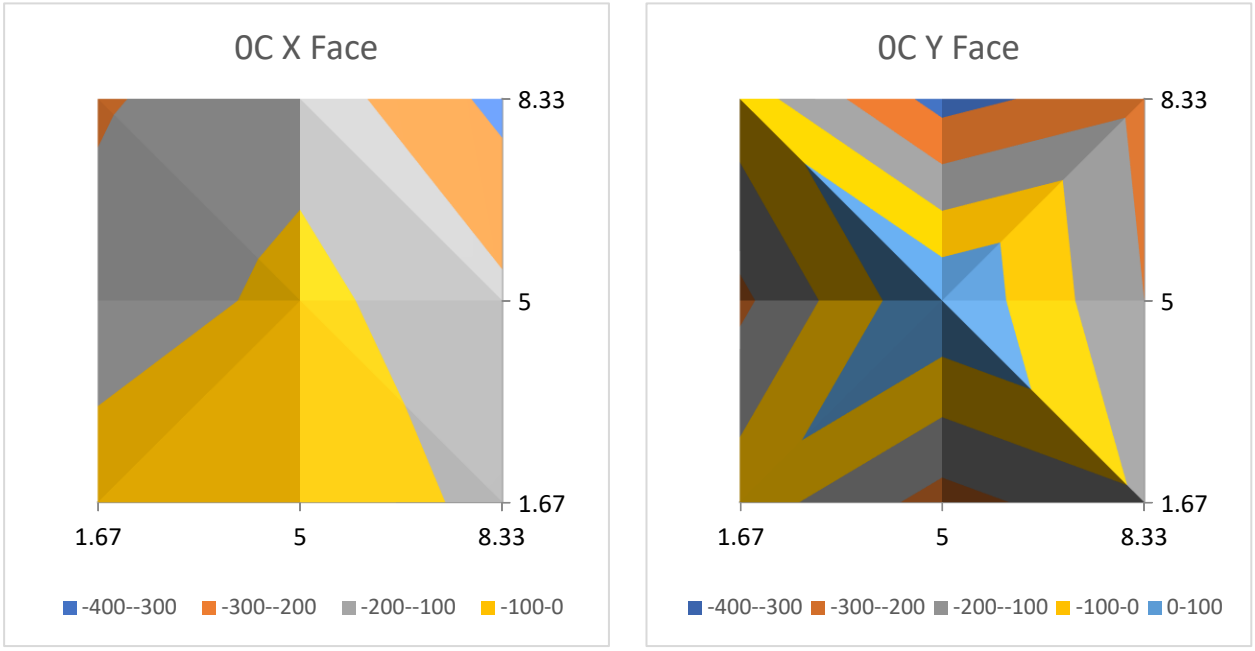

Figure C-1: Surface residual stresses of cube 0C [MPa]

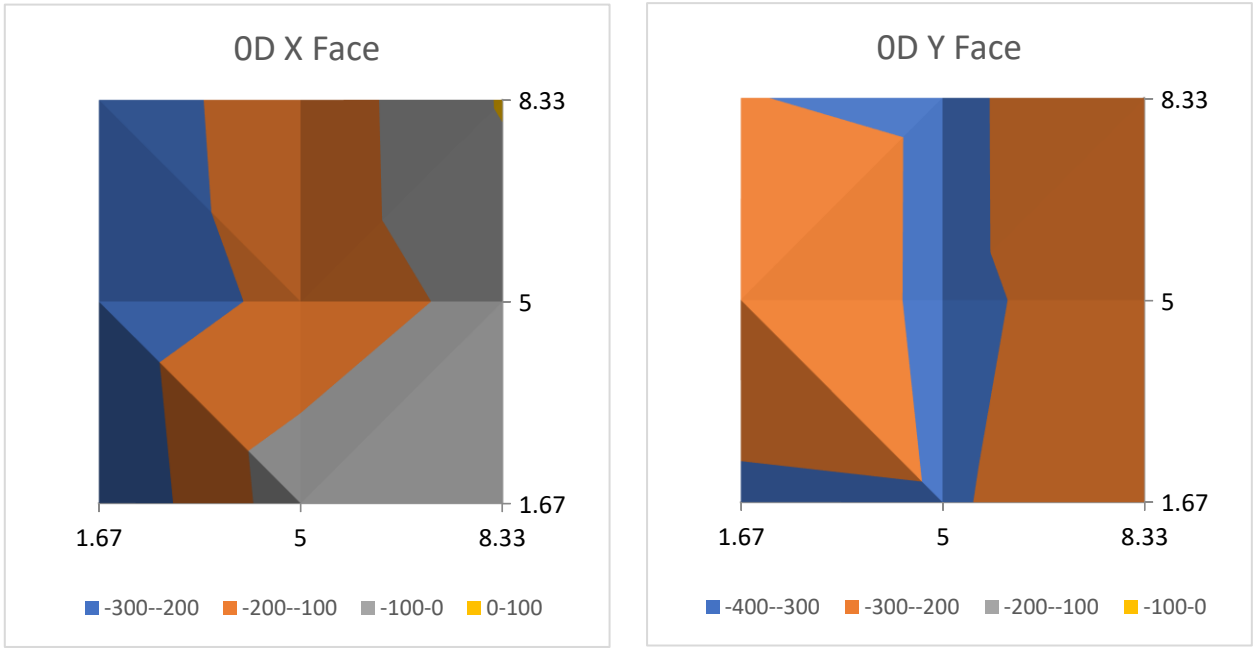

Figure C-2: Surface residual stresses of cube 0D [MPa]

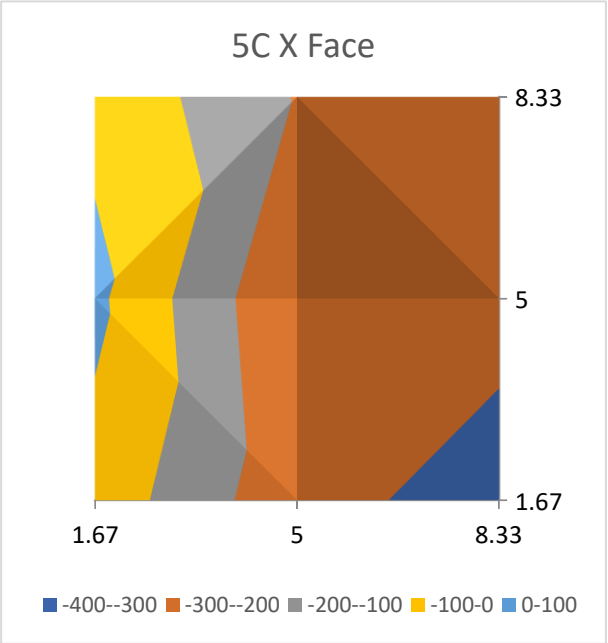

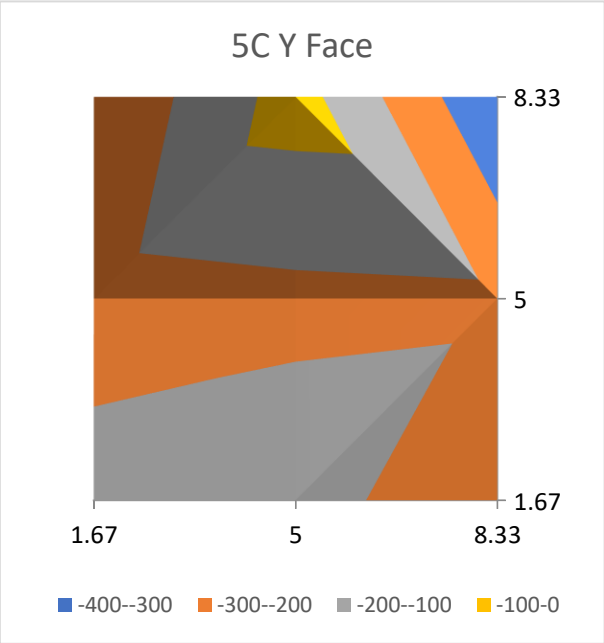

Figure C-3: Surface residual stresses of cube 5C [MPa]

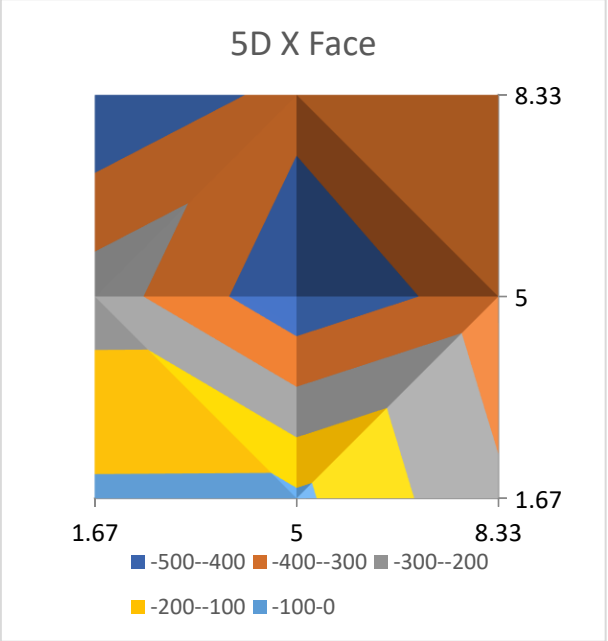

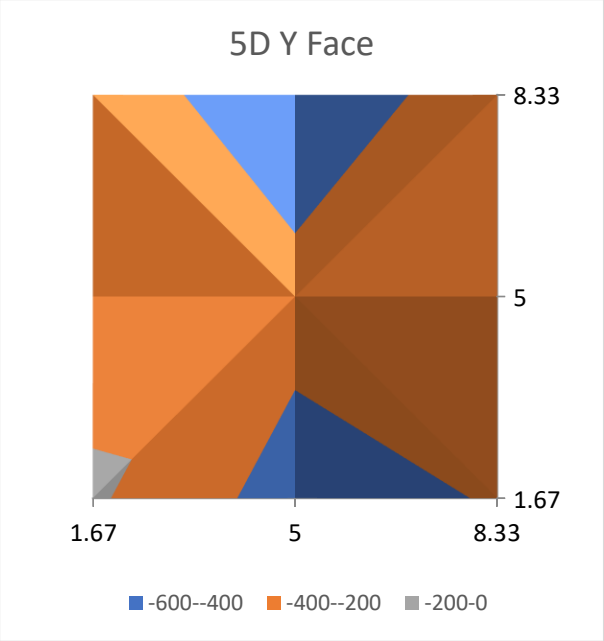

Figure C-4: Surface residual stresses of cube 5D [MPa]

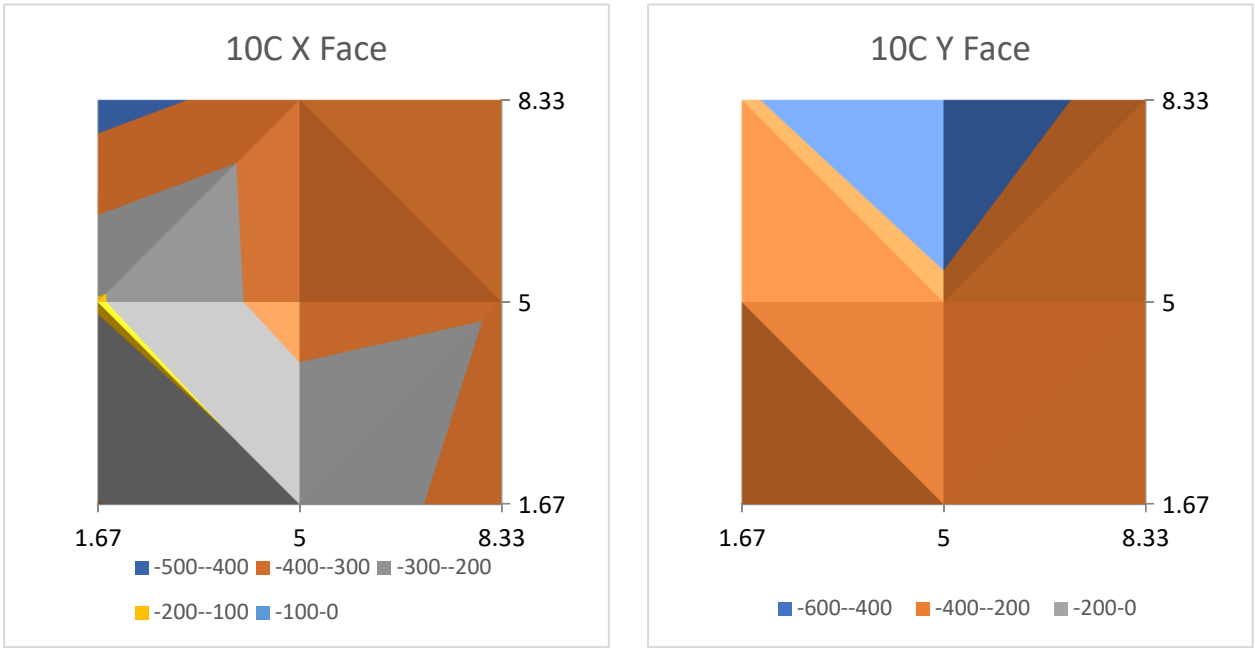

Figure C-5: Surface residual stresses of cube 10C [MPa]

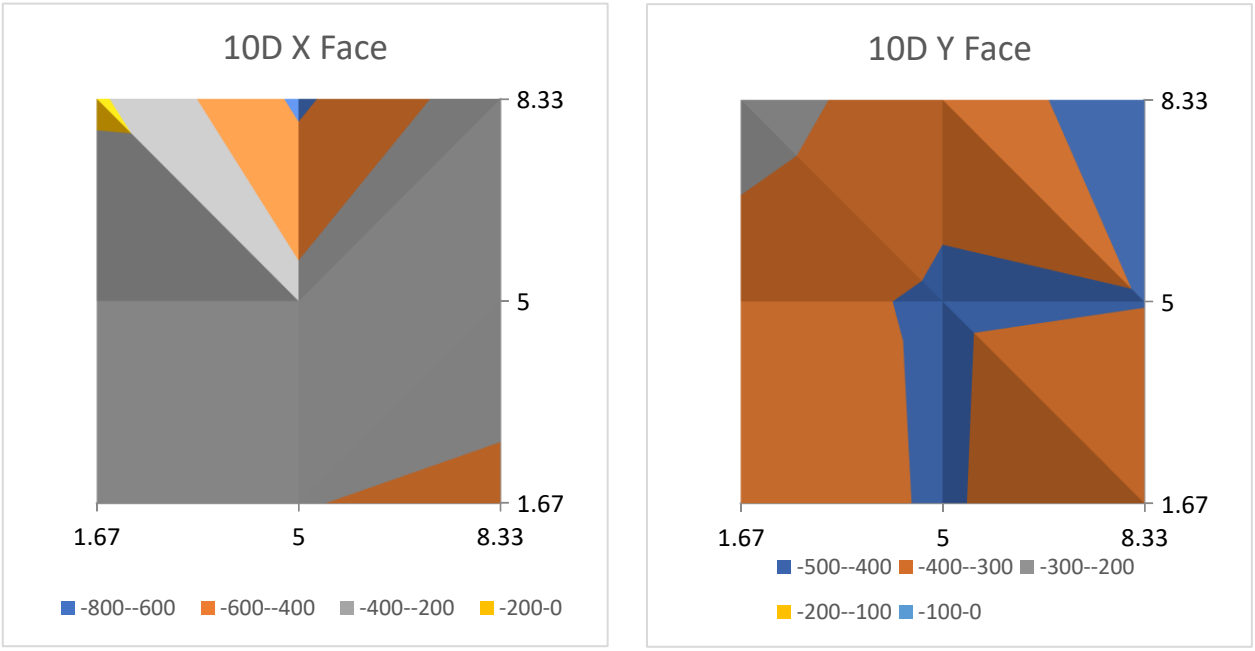

Figure C-6: Surface residual stresses of cube 10D [MPa]